TALLINN UNIVERSITY OF TECHNOLOGY
School of Information Technologies

Joosep Niinemägi 204764IVEM

APPLICATION OF PARTIAL POWER CONVERTERS FOR THE POWERING OF FUTURE CIRCULAR COLLIDER

Master's Thesis

Supervisor: Andrii Chub
PhD

Co-supervisor: Manuel Colmenero Moratalla
MSc

Tallinn 2023

TALLINNA TEHNIKAÜLIKOOL
Infotehnoloogia teaduskond

Joosep Niinemägi 204764IVEM

OSAVÕIMSUSEGA TOITEMUUNDURITE RAKENDAMINE FUTURE CIRCULAR COLLIDER OSAKESTEKIIRENDI TOITMISEL

Magistritöö

Juhendaja: Andrii Chub
PhD

Kaasjuhendaja: Manuel Colmenero Moratalla
MSc

Tallinn 2023

Author's Declaration of Originality

I hereby certify that I am the sole author of this thesis. All the used materials, references to the literature, and the work of others have been referred to. This thesis has not been presented for examination anywhere else.

Author: Joosep Niinemägi

30.12.2023

Abstract

This Master's thesis was written in cooperation with the Power Converter Group at CERN, the European Organization for Nuclear Research, located in Geneva. The accelerator complex at CERN is a succession of particle accelerators with increasingly higher energies, with the objective to accelerate and to collide particles for research. CERN is currently developing the concept for the next-generation particle accelerator called the Future Circular Collider (FCC), and this Master's thesis contributes to the conceptional design studies for the powering of this machine. More specifically, in the context of energy storage systems (ESSs).

The optimization of energy storage integration is essential in achieving an economically and environmentally viable technical solution. The concept of partial power processing (PPP) has gained significant attention due to its application in DC grids, photovoltaic systems, and energy storage applications, offering advantages such as increased efficiency, higher energy density, and reduced component ratings. However, no conclusive analyses have been put forward to demonstrate the advantages of the PPP concept in ESSs.

In this thesis, a specific partial power converter (PPC) topology is analyzed for energy storage integration, and its performance is validated through extensive simulations. A comparative analysis is conducted with conventional full-power converters to highlight the fundamental differences between the energy conversion approaches, aiming for a comprehensive comparison. The specific focus of this study is the integration of batteries into the submodules of a high-power bidirectional AC-DC converter called a Modular Multilevel Converter (MMC) within the FCC.

The research findings demonstrate the tremendous potential of PPCs in such applications, showcasing notable improvements in efficiency and a smaller overall footprint. The PPC outperformed the conventional full power converters, with a 2.42% higher efficiency, 69.07% smaller volume, and 16.33% lower cost. Through detailed calculations, the study provides strong evidence supporting the consideration of PPCs as an attractive technology for interfacing batteries to the power distribution system of FCC. Additionally, the outcomes of this research contribute not only to the advancement of energy storage integration within large-scale particle accelerators like the FCC but also address the industry's interest in enhancing the designs of ESSs in terms of efficiency and cost.

Previously, PPCs had not been considered for battery integration into MMC submodules. By embracing PPCs, the advancements in battery technology can be further exploited with more efficient and sustainable integration solutions.

The thesis is written in English and is 104 pages long, including 5 chapters, 53 figures, 7 tables, and 4 appendices.

Annotatsioon

Osavõimsusega Toitemuundurite Rakendamine Future Circular Collider Osakestekiirendi Toitmisel

Käesolev magistritöö kirjutati koostöös CERNi, Euroopa Tuuma-uuringute Organisatsiooni, toitemuundurirühmaga, mis asub Genfis. CERNi kiirendite kompleks koosneb järjestikest osakestekiirenditest, mille energiad kasvavad järjest kõrgemaks eesmärgiga kiirendada ja kokku põrgatada osakesi teadusuuringuteks. Praegu arendab CERN kontseptsiooni järgmise põlvkonna osakestekiirendi (FCC) jaoks ja käesolev magistritöö aitab kaasa selle masina toiteallikate kontseptuaalsete disainiuuringute loomisele, täpsemalt energiasalvestussüsteemide kontekstis.

Energiasalvestuse integreerimise optimeerimine on oluline, et saavutada majanduslikult ja keskkonnasäästlikult jätkusuutlik tehniline lahendus. Osavõimsusega toitemuunduri kontseptsioon on pälvinud märkimisväärset tähelepanu alalisvooluvõrkudes, päikesepaneelide süsteemides ja energiasalvestuse rakendustes tänu oma kõrgendatud kasutegurile, kõrgemale energiatihedusele ja vähendatud komponentide nimiväärtustele.

Käesolevas magistritöös analüüsitakse konkreetset osavõimsusega toitemuunduri topoloogiat energiasalvestuse integreerimiseks. Osavõimsusega toitemuunduri jõudlus valideeritakse põhjalike simulatsioonide abil. Analüüs ja võrdlus viiakse läbi tavapäraste kahesuunaliste täisvõimsusega toitemuunduritega, et tuua välja topoloogiate põhilised erinevused, et saavutada kõikehõlmav võrdlus. Uurimistöö keskendub täpsemalt akude integreerimisele modulaarse mitmetasandilise toitemuunduri alammoodulitesse FCC's.

Uurimistulemused näitavad, et osavõimsusega toitemuundurid omavad suurt potentsiaali energia salvestuse rakendustes tänu oma kõrgendatud kasutegurile ning vähendatud muunduri mõõtmetele. Osavõimsusega toitemuundur saavutas 2.42% kõrgema kasuteguri, 69.07% väiksema mahu ning 16.33% madalama hinna võrreldes tavapäraste toitemuunduritega. Põhjalike arvutuste abil pakub uuring tugevaid tõendeid osavõimsusega toitemuundurite kaalumiseks atraktiivse tehnoloogiana akude ühendamiseks FCC'sse. Lisaks ei aita selle uurimistöö tulemused kaasa mitte ainult energiasalvestuse integreerimise edendamisele suurtes osakestekiirendites nagu FCC, vaid aitavad ka täita tööstuse

huvi energiasalvestussüsteemide parema tõhususe ja kuluefektiivsuse osas. Varasemalt ei ole osavõimsusega toitemuundureid kaalutud akude integreerimiseks mitmetasandilise toitemuunduri alammoodulitesse. Osavõimsusega toitemuundurite kasutuselevõtmine võimaldab veelgi paremini ära kasutada aku-tehnoloogia edusamme, et saavutada nende efektiivsem ja jätkusuutlikum integratsioon.

Lõputöö on kirjutatud inglise keeles ning sisaldab teksti 104 leheküljel, 5 peatükki, 53 joonist, 7 tabelit ja 4 lisa.

List of Abbreviations and Terms

AC	Alternating Current
CAD	Computer Aided Design
CERN	European Organization for Nuclear Research (Conseil Européen pour la Recherche Nucléaire)
DAB	Dual Active Bridge
DC	Direct Current
DPC	Differential Power Processing
EMC	Electromagnetic Compatibility
ES	Energy Storage
ESS	Energy Storage System
EV	Electric Vehicle
FCC	Future Circular Collider
IGBT	Insulated-Gate Bipolar Transistor
ISOP	Input Series Output Parallel
IPOS	Input Parallel Output Series
LHC	Large Hadron Collider
LTO	Lithium-Titanate-Oxide
MLT	Median Length per Turn
MMC	Modular Multilevel Converter
MPN	Manufacturer Part Number
MOSFET	Metal-Oxide-Semiconductor Field-Effect Transistor
MVDC	Medium Voltage Direct Current
PV	Photovoltaic
PWM	Pulse Width Modulation
PPP	Partial Power Processing
PPC	Partial Power Converter
RMS	Root Mean Square
SiC	Silicon Carbide
UPS	Uninterruptible Power Supply
ZCS	Zero Current Switching

Table of Contents

List of Figures

List of Tables

1. Introduction

1.1 CERN and the Accelerators

CERN (European Organization for Nuclear Research) is an international scientific research organization in Geneva, Switzerland. CERN's primary focus is to conduct fundamental research in particle physics [1].

It is best known for its Large Hadron Collider (LHC), the world's largest and most powerful particle accelerator. The LHC consists of a circular underground tunnel with a circumference of 27 km, where two beams of high-energy particles, usually protons, are accelerated to nearly the speed of light [1]. These beams are made to collide at four experimental sites, as seen in Figure 1. There, the sophisticated detectors can detect the resulting collisions and analyze their properties. The largest detectors at CERN are ATLAS and CMS [1].

The primary objective of the LHC experiments is to investigate the fundamental nature of the universe. The discovery of the Higgs boson in 2012 was a significant milestone achieved by experiments conducted at the LHC, confirming the existence of the Higgs field and elucidating the mechanism of mass generation for elementary particles [2].

The accelerator complex at CERN comprises a series of machines that progressively increase the energy of particle beams. Each machine passes the beam to the next, culminating in the LHC, where beams reach a record energy of 6.5 TeV [1]. Many accelerators in the complex have their experimental halls for lower energy experiments. The size of an accelerator is determined by its maximum energy, which depends on the radius of the machine and the strength of the magnetic field that confines particles in their orbits [1].

1.2 Future Circular Collider

CERN is currently working on the feasibility study for the next-generation Hadron Collider. The Future Circular Collider (FCC) is planned to have a circumference of 91 km [4]. This is more than a threefold increase in the tunnel length compared to the LHC. The new accelerator could potentially reach energies up to eight times those of the LHC [5]. Higher energies combined with a precise measurement apparatus would enable new physics to be discovered by physicists [4, 5].

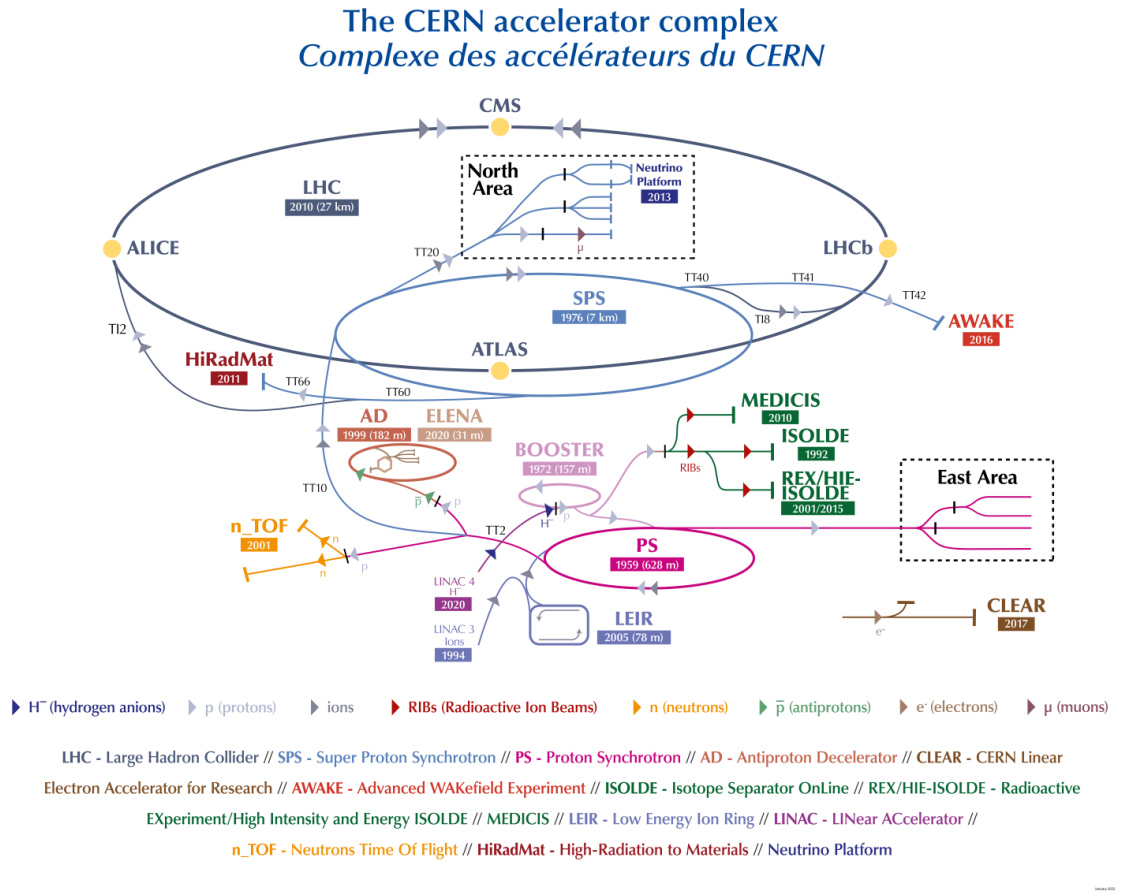

Figure 1. CERN accelerator complex [3].

1.3 Superconducting Magnets

In a proton accelerator like the LHC, the maximum achievable energy is directly linked to the strength of the magnetic field in the dipole magnets, given a specific acceleration circumference [6]. The dipole magnets used in LHC are designed to provide a very high field of 8.3 T over their length [1]. Furthermore, a current of 11 850 A flows in the magnets during peak operation [1]. The current waveform in the dipole magnets is illustrated in Figure 2.

The design of the LHC faced a significant technological challenge concerning its dipole magnets. The required magnetic properties could not have been realized practically using warm magnets. For this reason, superconducting magnets were employed. Superconductivity is achieved by bringing the temperature of the specifically engineered conductor material down to 1.85 K using liquid helium, which is actively kept at a stable temperature by the accelerator's cryogenic system [1]. FCC is also planned to use superconductive magnets [6]. One of the goals for FCC's magnets design programme is to achieve a stable

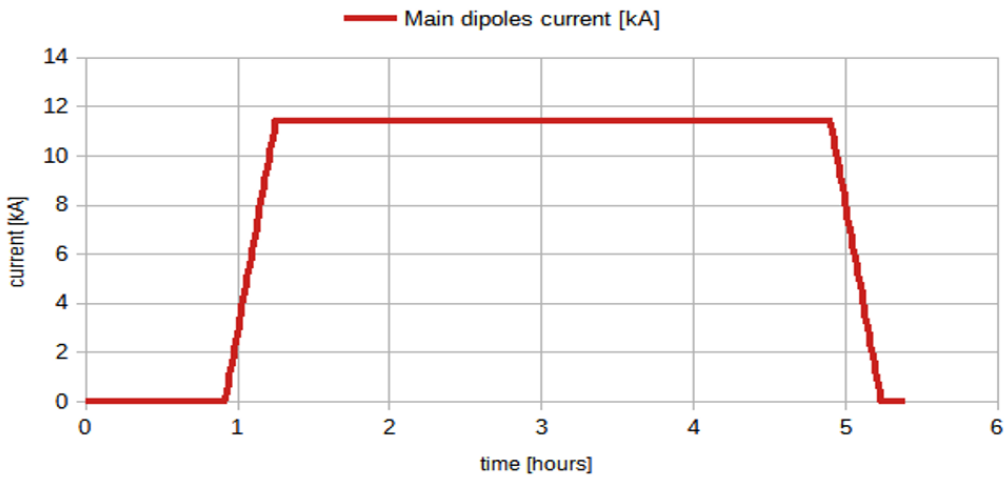

Figure 2. Current in the dipole magnets.

magnetic field with more than double the field strength achieved in LHC [6]. The FCC will incorporate a larger quantity of magnets and more powerful magnets with a greater capacity to store energy compared to the LHC. The total amount of energy to be stored in FCC's main dipole magnets during peak magnetic field is 174 GJ [7]. This is equivalent to 90 high-speed trains running at the speed of 360 km/h [7].

1.4 Energy Storage Technologies

The ongoing FCC Feasibility Study has revealed that the proposed dipole magnets require a significant amount of energy. Additionally, there are quadrupole and sextupole magnets that require comparatively less energy, though it is still substantial. The main dipole magnets in FCC are planned to ramp up and down up to four times a day during the operation of FCC [5].

Considering the vast amount of stored energy in the magnets, it is impractical and economically disadvantageous to obtain this power directly from the grid [5]. Furthermore, as superconducting magnets are used, most of the energy stored in the magnetic fields could be retrieved. Thus, the implementation of a local energy storage system (ESS) becomes essential [5]. ESSs can encompass various technologies, including battery storage, flywheel storage, capacitor storage, hydrogen storage, and pumped hydroelectric storage [8, 7]. It is planned that the ESS will supply all the energy needed for generating a magnetic field in the magnets. The losses occurring in the system shall be sourced from the grid. During the ramp-up sequence, energy is supplied to the main dipole magnets from ESS. Once the required magnetic field strength is reached, the current is kept stable, as shown in Figure 2. During the ramp-down sequence, the current in the magnet is reduced, and the released

energy will be captured and stored back in the ESS [7, 5].

1.5 Objective and Scope of Thesis

This subsection covers the problem statement of the thesis. This thesis seeks to address the challenges associated with energy storage (ES) integration in the context of the FCC. As the magnets utilized in the FCC project require a substantial amount of energy, the development of an ES solution is necessitated. As detailed in the next chapter, there exist different approaches, solutions, and converter topologies for achieving an optimal ES solution. Possible solutions are presented and analyzed. This raises the question of the most suitable technology and explores the benefits of using the concept of partial power processing (PPP), proposed by the Power Electronics Research Group at TalTech, for ES applications for CERN's FCC program.

PPP is a concept in power electronics where only a part of the transferred power is processed by the converter's components [9]. This allows for decreasing the cost and size of a power converter while increasing its efficiency [9]. The objective of this thesis is to synthesize a suitable partial power converter (PPC) and provide a comprehensive comparison with the existing solutions based on theoretical and simulation analysis.

The main portion of this study consists of demonstrating the operation principle of the PPC assisted with simulations, providing an overview of the relevant technologies involved, and conducting a comprehensive comparison among the various converter topologies. Two conventional bidirectional power converter topologies are also introduced and analyzed. A case for a comparison between the converters is presented. The comparison is made between the converters based on various key performance indicators such as constraints, efficiencies, cost, and volume, enabling a thorough evaluation of the converters. Additionally, the performance and characteristics of different topologies, including the PPC, are compared in detail. Moreover, the comparison encompasses loss calculations, component selection, and magnetics calculations specified in Appendix 2, Chapter 4, and Appendix 3 respectively. The analysis conducted in this thesis seeks to provide an understanding of whether PPCs could be a beneficial choice in the FCC project as a means of connecting ES to the FCC's power distribution system.

This thesis contributes to the feasibility study of the FCC. This research work was performed during an internship at CERN, which was funded under CERN's Technical Student Programme.

2. Background on Energy Storage Integration in the FCC

This chapter gives an overview of different aspects of integrating ES into the FCC. Initially, the question is investigated on a system level. From there, an overview is given of power converter topologies that could be used in such applications. Additionally, a short analysis of suitable solutions for ES integration is conducted.

2.1 Energy Storage Integration Scenarios

This section gives an overview of different scenarios in which ES could be integrated into the electrical system of the FCC. Although different ES technologies were considered, it should be noted that along the progression of the FCC Feasibility Study, battery storage has been proven to be the most suitable energy storage technology. This suitability means a good compromise regarding maintenance and procurement costs, electrical and mechanical suitability, and longevity. Currently, batteries are the most economical and efficient form of ES [8]. Therefore, alternative technologies are not considered in this thesis. At the current stage of development, the LTO (Lithium-Titanate-Oxide) cell type has been chosen as a suitable battery technology [5]. The main advantages of LTO battery technology are its faster charge rates, high number of charge cycles, and elevated level of safety [10, 5]. For this application, safety is an especially important factor in selecting the battery technology. Moreover, the reality of having batteries located underground significantly increases the concerns regarding fire safety. Since battery technology evolves rapidly, the specific cell type shall be fully reassessed at the time of procurement [5].

As mentioned in Section 1.4, the energy required during the operation of the magnets will be sourced from the local ESS. When the magnetic field is not required, the energy will be recaptured into the ESS. However, there can be several different approaches on how to connect the batteries to the magnets. The goal in designing an ESS integration solution for the FCC is to achieve a high-efficiency power path between the batteries and magnets. On the other hand, another goal is to minimize the installation cost that depends on the amount of excavated bedrock and wiring. Additionally, the electrical performance of the system shall be considered. This is especially true when considering the losses in the system against the procurement costs.

Three layout configurations are considered for connecting ES to the magnets of the FCC. All configurations could potentially be supplemented with medium voltage direct

current (MVDC) networks. MVDC networks have shown great promise to be utilized, for example, in data center integration, rail networks, marine applications, EV charging station integration, ES applications, and collection grids for wind and solar [11]. The voltage distribution rating in MVDC applications is generally between 1.5 kV and 55 kV [11]. MVDC is already utilized in many applications, including railway and collection grids for renewable energy [12]. MVDC grid provides advantages over medium voltage AC grid, including increased efficiency of the system and increased power throughput with the same diameter of conductor [11]. Additionally, it has improved flexibility, controllability, and efficiency, as there is no reactive power [11]. Due to the fact that DC distribution allows for transferring more energy through the same cable cross-section than the AC distribution, the economical and environmental advantages become evident as smaller cables can be used [12, 11]. The three layout configurations proposed by CERN with their critical system components are described in the following subsections. One goal of the following subsections is to present the different aspects of the given application, together with its challenges and solutions, to achieve the best way to connect batteries to magnets.

2.1.1 Energy Storage in Magnet Power Converters

One solution for connecting storage to the system is to install the batteries next to the power converters that power the magnets. This is a decentralized approach that comes with numerous advantages. This approach allows to have the shortest possible connection path between the magnets and the associated power converters. This allows to minimize transmission losses. However, this would require the allocation of additional space for the batteries in the caverns. This is illustrated in Figure 3 with the batteries shown in pink with magnet power converters connected to them. In the center, the AC-DC power converters are visible together with a transformer for AC grid connection. The magnets and their connections are depicted in blue.

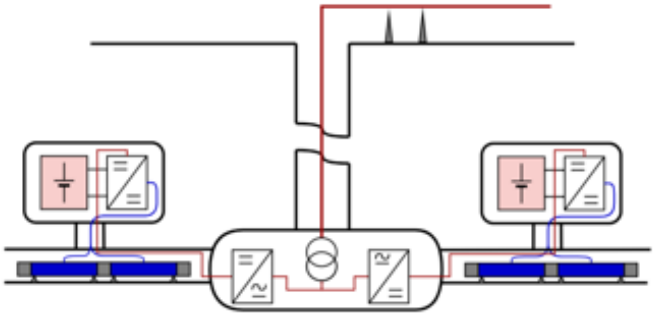

Figure 3. Illustration of localized energy storage at the level of magnet power supplies.

Creating additional space in the underground caverns adds to the implementation cost of the project. In regards to the grid connection, there are two considered variants [7]. There is an option for connecting the grid to the system through transformers and a high-power bidirectional AC-DC power converter called a Modular Multilevel Converter (MMC) located in the caverns. This would further minimize the losses as the HV connection can be brought closer to the consumption point. However, this also implies that additional space is dedicated for transformers and MMCs in the caverns. Furthermore, this would increase the installation cost and complicate equipment maintenance. Another option would be to have the transformers and MMCs located on the surface with an MVDC connection with the power converters in the caverns. This would reduce the amount of excavated material while taking advantage of the efficiency of the MVDC connection [7].

2.1.2 Centralised Energy Storage in MVDC Networks

Another solution for connecting ES to the system is to connect them to the magnets in a centralized way through an MVDC connection. This approach has the advantage of simplified logistics as the batteries are located in fewer locations. This simplifies the access and maintenance of the systems. One of the downsides of this solution is the higher transmission losses between the batteries and the magnets compared to the solution discussed previously. However, this solution could be realized in several different ways. One option is to have the batteries installed in the caverns together with the MMCs. This solution is illustrated in Figure 4 with the batteries shown in pink next to DC-DC converters for MVDC connection. The MVDC connection ties together the magnet power converters, ESS, and power from the grid. The AC-DC converters for the grid connection are on the surface.

It has the advantage of retaining comparatively short connections between the batteries and magnets, which helps with the efficiency of the system. Additionally, it retains the

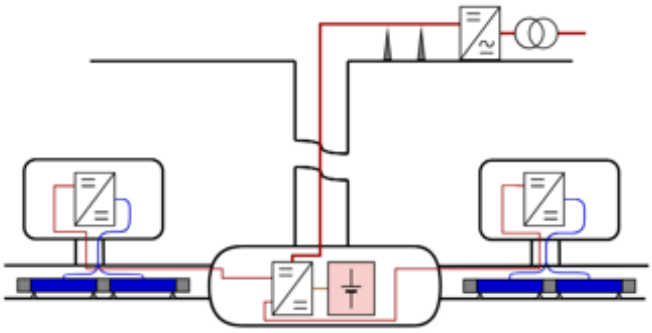

Figure 4. Illustration of centralized energy storage using MVDC networks.

centralized ES, which helps with maintenance and fault detection. It should be noted that the amount of bedrock removed is not necessarily increased with this solution. However, the bedrock removal occurs in fewer locations and at a grander scale. This could translate to savings in the tunneling stage due to simplified logistics. A different solution is to have the batteries installed above ground together with the MMCs. With this approach, it is possible to reduce the amount of bedrock that has to be removed during tunneling significantly. This would translate to further reduced cost of the installation. An additional advantage of this approach is easier access and maintenance. As the batteries are above ground together with the MMC, the replacement of components in the event of a fault is simplified. Additionally, the risks involving a fault in the system are reduced as there is better access to the installations. However, its main drawback is that the cables connecting the batteries to the system are longer, which results in increased total losses in the system. Therefore, from these options, the more advantageous direction shows to be the prior.

2.1.3 Distributed Energy Storage in MVDC Networks

Another solution for connecting ES to the magnets is to distribute it between two installation sections. This would mean that some part of the ES would be installed inside the caverns, and another part would be installed on the surface level. In this case, the energy flows to the magnets through two different paths. The common part between these two sections is the shared MVDC power bus. One part of the ES can be placed in the caverns close to the FCC's MVDC grid's distribution point, as illustrated in Figure 5. Here, the batteries are shown in pink connected to DC-DC converters in the caverns and to AC-DC converters on the surface. Thus reducing the designated volume in the caverns for ES. The MVDC connection ties together the magnet power converters, ESS, and power from the grid. In addition to the components mentioned, it is also possible to utilize the MVDC connection for on-surface installations (depicted as a blue box) such as control centers, renewable energy production and/or additional energy storage. The major part of the ES can be placed outside of the caverns and could be integrated into an MMC, which links the FCC to the AC power grid. This MVDC bus would be shared between the MMCs and other systems.

This solution's advantage is its high energy transfer efficiency thanks to the proximity of the ES to the magnets. As the ES is distributed, the volume of designated cavern space for ES is reduced. During the current ramping, the energy is taken from both ES locations. This solution helps to minimize the costs of excavations while also minimizing transmission losses. This solution would entail using Modular Multilevel Converters in two locations. The converters would need to be installed on the ground level together with ES and connection to the AC grid. The rest of the MMCs would be installed in the caverns together with ES and MVDC bus connections. MMCs are bidirectional AC-DC converters,

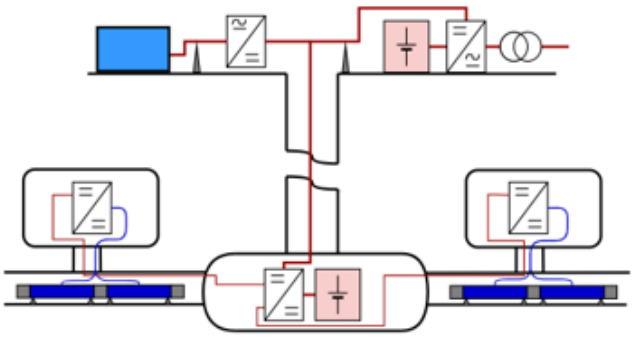

Figure 5. Illustration of distributed energy storage using MVDC networks.

which are commonly used in medium to high power applications where higher voltages are required [13]. Its higher voltage operation is achieved by stacking together submodules of commercially available semiconductor switches [13]. Thanks to its bidirectional power control capabilities, MMC often finds its way into applications where active front-end functionality is required [14]. Its modular design allows the development of a converter for any required voltage level. A typical MMC comprises six arms with two arms per phase, as illustrated in Figure 6, together with the potential connection to ES [15]. Each arm consists of identical submodules connected in series. Each arm is coupled with an arm inductor at the connection point within a phase. A submodule consists of semiconductor switches in the half-bridge, full-bridge, or another configuration with a DC capacitor [15]. Submodule in a half-bridge configuration is depicted in Figure 6 together with an illustration of how ES could be integrated into MMCs.

As shown in Figure 6, each submodule in an MMC could be connected to ES. In this example, the energy flow to and from storage is controlled with the help of a DC-DC converter. Without a converter coupling the MMC submodule to the battery, it is impossible to control the energy flow in the battery itself. Additionally, as the MMC is coupled with an AC grid, there is an AC voltage ripple present at each submodule of the MMC at the frequency of the grid [15]. This means that without a DC-DC converter, the battery's current ripple, charge current, and battery performance cannot be controlled. This could lead to accelerated aging of the battery cell and possible control issues in the system [16, 17]. With the help of a DC-DC converter, it is possible to coordinate the required power flow with the MMC in such a way that all the energy required for ramping up the current in the magnets could be taken from the ES and the system losses could be provided from the AC grid.

Additionally, the energy recaptured from the magnets can be directed back to the ES in a controlled way. It should be noted that AC voltage ripple on a submodule level could still

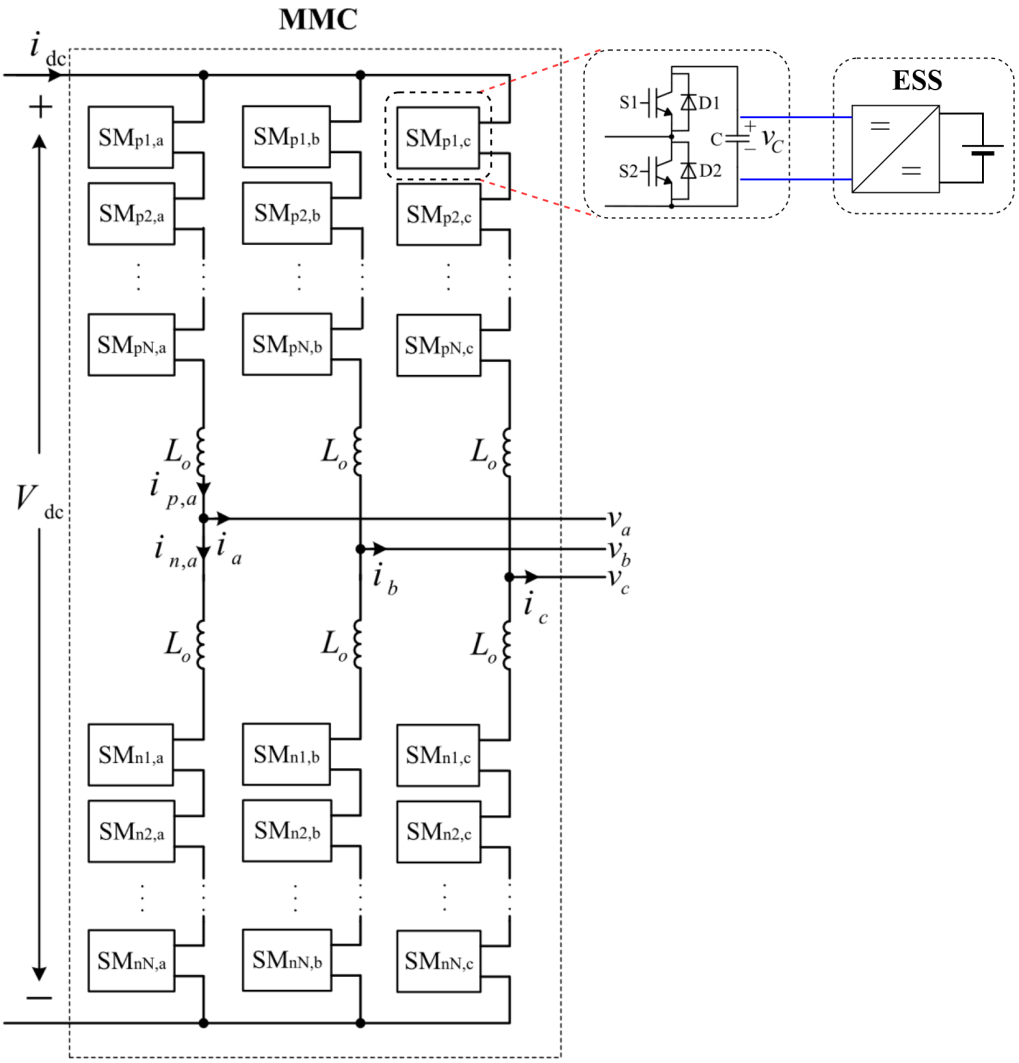

Figure 6. Schematic of MMC topology with illustration of ES integration. [13]

cause problems to the battery cell if the DC-DC converter does not correctly control the current ripple in the battery. Therefore, good design practices should be followed to protect the batteries and achieve controllability. The main components of an ESS considered in this study are a battery bank, a bidirectional power converter, and the load. An MMC submodule is considered to be the load, in this study. This thesis envisions ESSs connected to all MMC submodules. This allows the MMC to provide energy to the magnets from ESS and, consequently, recapture this energy when the magnetic field is not required. In the next section, the requirements and suitable DC-DC converter topologies are further discussed.

2.2 DC-DC Conversion for ESS

This section gives an overview of power converter topologies that could be used in battery ES applications. An essential function of ESS is to control the flow of energy. In the case of batteries, the importance of safe operation during charge and discharge cycles cannot be overstated. Banks of batteries can store a significant amount of energy, which, if not properly controlled, can cause a lot of damage to the technical infrastructure. Additionally, the integration of ESS into MMC submodules is challenging because of the low-frequency voltage ripple present in the submodules, as explained in the subsections above. The flow of energy is bidirectional in ESS. During discharge mode, the energy is transferred from the ESS to the load, and during charge mode, energy is transferred from the load to the ESS. This operation could be achieved using two unidirectional power converters. However, in practice, it is more economical to use one bidirectional converter instead [8]. In the case of batteries, the current in the batteries must be controlled according to the battery manufacturer's guidelines to ensure their optimal performance and longevity. Moreover, attention should be put into limiting the current ripple in the battery. These considerations are applied in Chapter 4 - Benchmarking of the Converters of this thesis.

2.2.1 Half-Bridge

Half-bridge is a simple bidirectional converter topology that is known for its simplicity, high efficiency, wide input voltage range, and low cost [18]. Thanks to its wide input voltage range, it is widely used for battery applications in EVs, hybrid vehicles, and ESSs [19]. Additionally, the application of half-bridge converter topology has been demonstrated in integrating batteries into MMC's submodules [20, 21]. This converter topology utilizes two power switches in a half-bridge configuration together with filtering capacitors and an inductor, as illustrated in Figure 7. Additionally, it has a simple control structure in the form of pulse width modulation (PWM) [19]. The switches are controlled using a PWM switching signal. The power level and the power direction are controlled by changing the duty cycle. This topology works in boost mode in one direction and buck mode in the other direction. In buck mode, the energy is transferred to the output when the upper switch is conducting. In boost mode, the energy is transferred to the output when the lower switch is not conducting.

Because this converter topology uses an inductor for storing energy in between the periods, it does not provide galvanic isolation between input and output. Additionally, half-bridge converters generally have comparatively high switching losses, and their control can be complex when experiencing fluctuations in the input voltage or on the load [18].

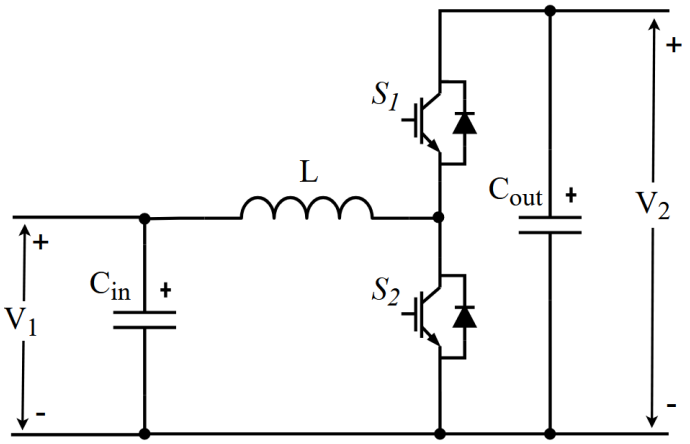

Figure 7. Half-bridge converter topology.

2.2.2 Dual Active Bridge

Dual Active Bridge (DAB) is a bidirectional DC-DC converter topology that provides galvanic isolation between the input and output [22]. DAB can be configured to work in either buck or boost operation [22]. This topology supports soft-switching operation, which helps to achieve higher efficiency figures [23]. It is often utilized in UPS, EV charging, renewable energy integration, battery integration, and DC microgrid applications [22, 23, 24]. Additionally, the application of DAB converter topology has been demonstrated in integrating batteries into MMC's submodules [25]. It comprises two full bridges connected to a high-frequency transformer with filtering elements [22]. DAB topology in its most basic form is illustrated in Figure 8.

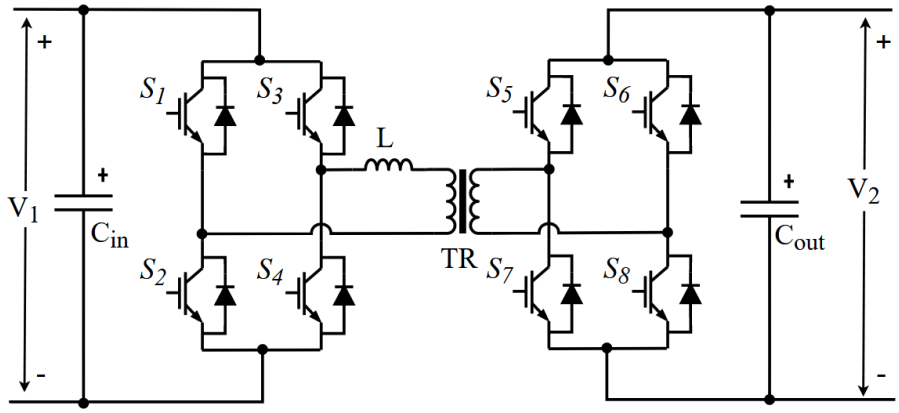

Figure 8. Dual Active Bridge converter topology.

The transformer is configured with a turns ratio required by the application. Each bridge is controlled with a constant duty cycle of 50%, producing a high-frequency square wave voltage at the transformer terminals. Compared to different proposed switching signal

modulation strategies, the phase-shift control method has the advantage of transmitting the maximum amount of energy [26]. By taking into account the leakage inductance of the transformer, which is an essential parameter in DAB, the two square waves can be adjusted in phase to control the power flow between two DC sources. This enables bidirectional power transfer. The power transfer equation, taking into account the first harmonic, can be used to describe the power flow in the DAB (see Equation 2.1) [27].

$$P_{\mathrm{DAB}} = \frac{V_1 \cdot V_2 \cdot \varphi(\pi - |\varphi|)}{L \cdot 2 \cdot n \cdot f \cdot \pi^2} \tag{2.1}$$

It should be noted that this equation applies when using phase-shift modulation only. Here, V_1 and V_2 represent the primary and secondary voltages, respectively, ϕ represents the phase angle, L represents the leakage inductance of the high-frequency transformer, n represents the turns ratio, and f represents the switching frequency. Increasing the switching frequency reduces the amount of power that can be transmitted. It is worth noting that decreasing the leakage inductance increases the amount of power that can be transmitted. The phase-shift angle can be measured between the gating signals of the primary side and secondary side switches. The voltage waveforms are rectangular and shifted. A greater shift angle results in more power being transmitted.

2.2.3 Partial Power Converters

In full power converters, the efficiency of the DC-DC converter plays a crucial role in determining the overall system efficiency. However, in PPP converters, the power loss occurring in the DC-DC converter is only a small percentage of the processed power, as illustrated in Figure 9. Consequently, the system efficiency in PPP converters cannot be equated to the efficiency of the DC-DC converter alone [9].

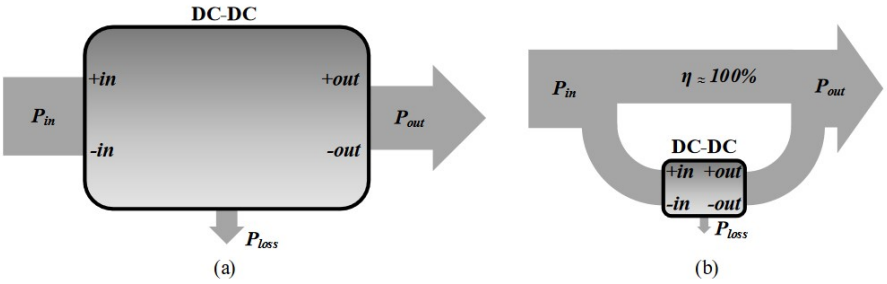

Figure 9. FPC (a) and PPP (b). [9]

Full power converters, which account for nearly all the converters used today, handle

all the power between the input and output. These converters face certain technological limitations that restrict significant improvements in their efficiency [9]. As a result, only small incremental gains in efficiency can be achieved.

On the other hand, there is a different type of converters based on the PPP concept. In PPP converters, only a fraction of the total power between the source and load, or input and output, is processed by the converter itself [9]. The remaining power is delivered directly to the load without undergoing any processing. This is achieved with a direct path for the current, allowing for theoretically up to 100% efficiency [9].

PPP converters allow for the design of a more efficient converter with higher power density. Partial power processing can be divided into two major subcategories: differential and partial power converters. Some have also proposed mixed strategies that preserve the advantages of both types [9].

Differential power processing refers to power converters designed to address current imbalances between different elements connected in series to the same voltage bus [9]. Instead of processing the total power consumed or supplied by the sum of the elements, differential power converter (DPC) architectures focus on correcting the mentioned current imbalance [9].

PPCs differ from DPC architectures in terms of their primary objective. While DPC architectures aim to correct imbalances between series-connected elements, PPCs focus on controlling power flow, current, and voltage levels between a source and a load [9].

The advantages of PPP converters are suitable in PV systems, ESSs, and EV charging [28]. The overall efficiencies of these architectures are high (typically >98%). Isolated topologies, particularly the isolated full bridge topology, are commonly employed in the conversion stage of these architectures. However, it's important to note that while isolated topologies are used within the converter, galvanic isolation in the overall system is not achieved [9].

There is a limiting factor to PPC operation, however, which is the range of imbalance between the input and output voltages [9]. This influences the partiality of a PPC. Partiality is the ratio of the power handled by the DC-DC converter and the total power passing through the system [9]. It is beneficial to have a lower partiality to take advantage of the PPP. PPCs have been proposed to work with up to 30% partiality to be advantageous over FPCs [9].

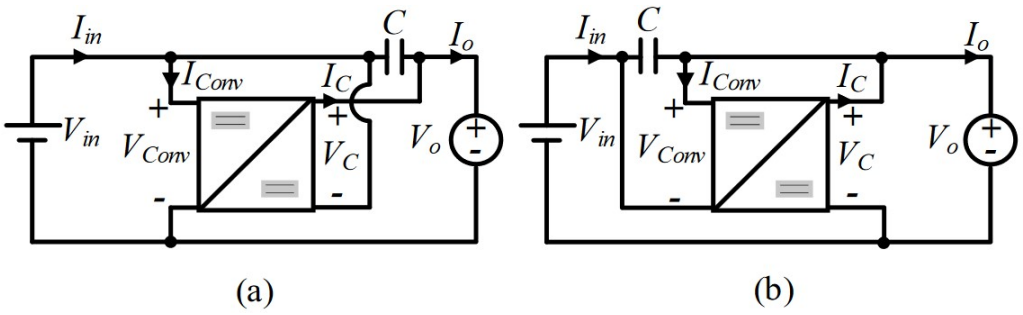

Figure 10. IPOS (a) and ISOP (b) configurations. [9]

This thesis focuses on PPCs because, in ES applications, the control of power flow is essential. PPCs can be further divided into two groups based on DC-DC topology employed: isolated and non-isolated PPCs.

There is limited literature on PPCs that do not require isolated DC-DC topologies [28]. One novel architecture presented in [28] is the fractional charging converter, which allows for non-isolated topologies within the PPC. This simplifies the design and manufacturability of the conversion stage. However, the fractional charging converter architecture has limitations in terms of the range of static voltage gain it can handle [28].

In the case of PPCs, which require an isolated DC-DC topology, there are two main configurations: input parallel output series (IPOS) and input series output parallel (ISOP) [24]. These configurations are visualized in Figure 10. They can be configured to work in either boost mode or buck mode and also achieve bidirectional power flow control [9]. In a DC-DC converter with a single polarity output, it is possible to operate a PPC in either boost or buck mode for each configuration. However, if the converter has the ability to change the polarity of its output voltage, both PPC modes can be achieved using the same converter. This functionality can benefit applications where the output voltage ranges from below to above the input voltage. Moreover, typical DC-DC topologies require additional circuitry to achieve this. For example, an unfolding circuit would provide this functionality [9].

In an IPOS configuration, the input power sources are connected in parallel, and the output power is connected in series. This means the power flows from the input side in parallel branches and then combines in series at the output side, as illustrated in Figure 10 (a). The Equations 2.2 and 2.3 are valid for the IPOS PPC configuration [9].

$$V_o = V_{\text{in}} + V_C \qquad (2.2) \qquad\qquad I_{\text{in}} = I_{\text{Conv}} + I_o \qquad (2.3)$$

On the other hand, in the ISOP configuration, the input power sources are connected in series, while the output power is connected in parallel. Here, the power flows from the input side in series and then splits into parallel branches at the output side, as illustrated in Figure 10 (b). The Equations 2.4 and 2.5 are valid for the ISOP PPC configuration [9].

$$V_{\text{in}} = V_{\text{Conv}} + V_o \qquad (2.4) \qquad\qquad I_{\text{o}} = I_{\text{in}} + I_C \qquad (2.5)$$

The IPOS step-up architecture is the most popular, and a wide variety of processed power ratio values can be reached due to the varying static voltage gain [28]. For this application, an IPOS configuration with a DAB topology has been chosen for the power conversion stage. This converter topology has not been tested in the considered applications. These applications are challenging due to the voltage ripple present in the MMC's submodules, which results in the need for battery current ripple rejection control [15].

2.3 Background Overview

In conclusion, this chapter delved into various configurations for integrating ESSs into FCC's electrical infrastructure. More specifically, it focuses on connecting them to magnets in the caverns. Three distinct approaches were explored: ES integration directly into magnet power converters, centralized ES in the caverns using MVDC networks, and decentralized ES using MVDC networks. The advantages and drawbacks of these approaches were considered. The approach of decentralized ES using MVDC networks sought to optimize efficiency by reducing designated cavern space for ESS, minimizing costs and losses. MMCs were considered for the connection between the AC and DC grids. Additionally, the possibility of integrating renewable energy production on-site is a plus. This is why this solution, together with the use of MMCs, is considered in this work as a potential use case.

The electrical considerations for integrating ESS into MMC's operation were discussed. Regarding this, it is not practical to connect batteries to MMC submodules with a direct connection due to the required precise control of power flow and the protection of batteries. Because of this, DC-DC converters, which control the power flow and the state of batteries, are required. Three power converter topologies were introduced and described. Half-bridge topology and DAB are widely known and used topologies that could be utilized in such use cases. PPC was introduced as a new method for ES integration. PPC promises to achieve higher power densities, higher efficiency, and a smaller converter footprint.

In summary, this chapter presented the main elements of the state of the art and concluded the presentation of existing work and the background of the topic. For ES integration into

MMCs, PPC was proposed to achieve a more efficient solution with a smaller footprint compared to conventional full-power converter topologies. The subsequent sections delve further into details regarding the operation of PPC, the design of PPC, and the comparison of PPC with the considered conventional full power converter topologies.

3. Proposed IPOS Partial Power Converter

In the previous chapter, an overview of different topologies and configurations for ES integration into FCC power systems was given. The concept of PPP was introduced, and the operation of PPC was briefly discussed. This chapter discusses the PPC topology in IPOS configuration based on DAB and goes deeper into its operation, control, and practical design considerations in the context of this work.

3.1 Operation Principle

The considered PPC topology is connected in an IPOS configuration and employs a DAB DC-DC converter. The operation of the active part of the converter, a DAB, was described in the previous chapter. However, the operation of the PPC topology in IPOS configuration based on DAB is slightly different. In this topology, the input is connected in series with the output of the DAB, as is illustrated in Figure 11. This means that the output voltage of the DAB is added to the primary side input voltage.

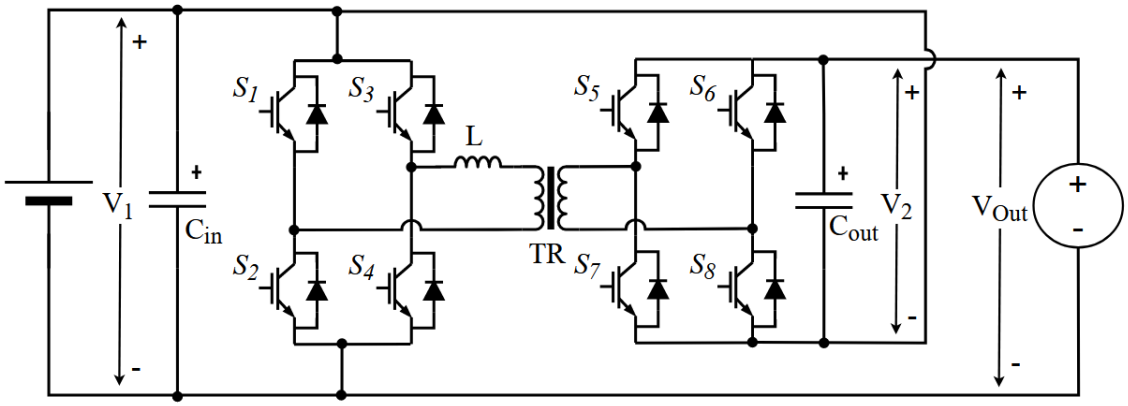

Figure 11. Diagram of proposed PPC in IPOS configuration based on DAB.

Furthermore, there is also a direct connection between the positive side of the input terminal and the negative pole of the DAB output. Most of the output current of the converter is passed through the latter connection path. As can be seen from Figure 11, there is a direct connection between the input and output negative terminals. The input is connected in parallel to the primary side voltage source, i.e., the battery. Part of the energy is transferred through a high-frequency transformer using switches in full bridge configuration on the primary and secondary sides. This kind of configuration introduces partiality to the converter. The partiality factor describes the amount of power the converter

processes and is determined by the voltage ratio between the primary and secondary sides. The power flow in this converter can, therefore, be described with the Equation 3.1 [27, 9].

$$P_{\text{PPC}} = \frac{1}{K_{\text{Pr}}} \cdot \frac{V_1 \cdot V_2 \cdot \varphi(\pi - |\varphi|)}{L \cdot 2 \cdot n \cdot f \cdot \pi^2} \tag{3.1}$$

In this equation, V_1 and V_2 represent the voltages on the primary side and the DAB secondary side, respectively. The DAB secondary side voltage must not be confused with the converter's secondary side voltage, which is not part of this equation. However, the partiality factor K_{Pr} reflects the ratio between the DAB input and output voltages, which is proportional to the ratio between processed and overall power. One can notice that this equation consists of two parts: the DAB power transfer equation and the reciprocal of the partiality factor. When considering the influence the processed power has over the partiality factor, it becomes evident that it directly influences the system's efficiency as well. Therefore, the efficiency of the system can be represented with the Equation 3.2 [9].

$$\eta_{\text{sys}} = \frac{P_{\text{out}}}{P_{\text{in}}} = 1 - K_{\text{Pr}} \cdot (1 - \eta_{\text{Conv}}) \tag{3.2}$$

where, μ_{Conv} represents the efficiency of the DC-DC power processing stage, and μ_{sys} represents the overall efficiency of the PPC. This equation shows that the efficiency of the DC-DC stage does not need to be high to ensure exceptionally high PPC efficiency if the partiality factor is low.

3.2 Design of PPC

This section goes into further detail on the design of the PPC. More specifically, the design of its simulation model's parameters. As a first step, the main specifications for the converters needed to be fixed beforehand. This is required to have a common starting point for the converter designs. Moreover, it is needed to compare the three DC-DC converter topologies accurately. The input specifications encompass voltages in the system and its power levels. The application specification and design constraints for a practical converter design for comparisons are discussed in more detail in Chapter 4 - Benchmarking of the Converters.

However, at this stage, it should be brought out that the input voltage (the battery bank voltage) was set to 800 V, and the average output voltage was set to 1000 V. The difference between input and output voltage is, therefore, 200 V. Resulting from the voltage ratio, the

PPC's partiality factor is 0.2. This means that the DAB DC-DC stage processes only 20% of the transferred power. The nominal power level for all converters was fixed at 40 kW, resulting in the PPC processed power of 8 kW. Because the end application at the output of the converter is an MMC submodule, the AC voltage component with a frequency of 50 Hz is also considered on the output. This AC component has an amplitude of 100 V peak to peak. This ripple complicates achieving accurate control and a stable power throughput.

The design of PPC, which uses DAB for its power processing part, started off with the design of a DAB converter. From there, it was possible to advance by reconfiguring its connections and control methods to operate as a PPC. The design process for achieving working DAB and PPC simulations that meet the specifications is described in the following subsections.

3.2.1 DAB Design

The design of DAB started with the calculation of critical components, including the transformer, its turns ratio, and the value of leakage inductance. The transformer turns ratio for a DAB topology can be calculated using the voltages applied to the primary and secondary side windings. The turns ratio is proportional to the converter's average primary and secondary voltages, i.e., defined by the 800 V/1000 V ratio. The required leakage inductance is calculated through the power transfer equation of the DAB, presented in Equation 3.3 [27].

$$P_{\text{DAB}} = \frac{V_1 \cdot V_2 \cdot \varphi(\pi - |\varphi|)}{L \cdot 2 \cdot n \cdot f \cdot \pi^2} \tag{3.3}$$

As can be seen from this equation, the power flow in the converter is determined by the voltages in the system, the phase shift between the primary and secondary bridges, the leakage inductance, and the switching frequency. As the voltages and switching frequency can be fixed by the requirements of the application, the remaining factors that can influence the power flow are the leakage inductance and phase shift angle. It has been demonstrated in the literature that a phase shift angle of 0.7 rad for nominal DAB operation allows to achieve a good balance between the controllability and efficiency, i.e., the circulating energy [29]. When phase shift at the nominal operating power level is limited to 0.7 rad, the leakage inductance is the remaining parameter to be identified. This limitation helps to fix the initial value of the leakage inductance at the level of 138 uH. However, when considering the design constraints detailed in Chapter 4, optimization of the design of DAB becomes necessary. The nominal phase shift needed to be reduced to achieve

better performance while decreasing the size of the filtering components. As a result of these optimizations, the nominal phase shift angle is set at 0.35 rad, which results in the required leakage inductance of 80 uH. The calculations for the practical realization of the DAB's transformer are further detailed in Appendix 2. The remaining passive components, such as capacitors and filtering inductors, were chosen while keeping the stability of the converter, the practical feasibility of these components, and the resulting performance of the converter in mind. Moreover, these component choices were verified and optimized iteratively through simulations.

The control methods for DAB are detailed in the following subsections. After successfully concluding the DAB simulation and verifying its proper functionality using feasible component values, the design phase of PPC could be initiated.

3.2.2 Practical PPC Design

The power transfer equation of a PPC based on DAB is quite similar to that of the DAB. However, the partiality factor must also be taken into account. As mentioned earlier, the partiality factor of PPC represents the ratio of power that is processed by the converter and the transferred power. In the PPC in ISOP configuration based on DAB topology, this is mainly determined by the ratio between the primary and secondary side voltages of the converter, i.e., 800V/200V [9]. The smaller the difference between the voltage is - the smaller the partiality factor is. A smaller partiality factor allows the design of a converter, which processes less power and achieves higher efficiencies in a smaller form factor while reducing its component ratings [9]. The equation for this converter's power transfer was depicted in Subsection 3.1. For the reader's convenience, it is brought out in Equation 3.6 [27, 9].

$$P_{\text{PPC}} = \frac{1}{K_{\text{Pr}}} \cdot \frac{V_1 \cdot V_2 \cdot \varphi(\pi - |\varphi|)}{L \cdot 2 \cdot n \cdot f \cdot \pi^2} \tag{3.4}$$

Considering that $K_{Pr} = V_2/V_1$, this equation could be simplified as shown in Equation 3.5.

$$P_{\text{PPC}} = \frac{V_1^2 \cdot \varphi(\pi - |\varphi|)}{L \cdot 2 \cdot n \cdot f \cdot \pi^2} \tag{3.5}$$

The distinct feature demonstrated by the simplified equation is that the phase shift angle does not depend on variations of the voltage V_2 caused by the AC component of the voltage V_{Out}. Hence, it could be predicted that the phase shift angle is defined only by

the system power, and only tiny variations of the phase shift angle may be expected as a result of variations in DC-DC stage losses. As the voltages and switching frequency can be fixed by the application's requirements, the remaining factors influencing the power flow relation are the leakage inductance and phase shift angle. Similarly to DAB, the nominal phase shift angle is limited to 0.7 rad according to recommendations in [29]. In this case, the proposed phase shift angle proved to yield a converter design that fits in the design constraints detailed in Chapter 4, achieving good performance while keeping the component sizes down. When the nominal phase shift angle is limited to 0.7 rad, the leakage inductance is the remaining design parameter to be defined. The required leakage inductance was therefore 550 uH and later adjusted in simulations to 700 uH to account for power losses and ohmic voltage drop in the DC-DC stage. The calculations for the practical realization of the PPC's transformer are further detailed in Appendix 2.

When reconfiguring a DAB into a PPC, the connections in the converter must be modified, as shown in Figure 11. There are other components that must also be changed to achieve a stable operation with practical component values. The selection of the switches was re-evaluated, and the model parameters were adjusted accordingly. The primary side switches were dimensioned for reduced operating current compared to the DAB converter with the same power rating. For the secondary switches, the voltage rating of the switches was reduced as they operate at full output voltage. The turns ratio for the transformer was also re-calculated for the PPC. The calculations for the practical realization of the PPC's transformer are further detailed in Appendix 2. The values of capacitors were chosen sufficiently high to keep the stability of the converter, with the practical feasibility of these components and the resulting performance of the converter in mind. Moreover, these components were verified and optimized iteratively through simulations. Compared to the DAB, the ratings of the capacitors could also be reduced. Additionally, the PPC did not require a filtering inductor on the output due to the differences in the output current waveform, the peculiarities of the MMC submodule, and the good stability of the converter. The control methods used in PPC are detailed in the following subsections.

3.3 PPC Control

This section covers the considerations for the control of the PPC. The control method for the DAB converter resembles, in its principle, the control methods of PPC. For this reason, it is not specifically discussed in this work. Instead, a thorough explanation of the control method for the PPC is given. In this thesis, multiple types of control systems were implemented for the PPC, including active DC Bias correction, PPC control with a stable DC output, and a PPC control with a varying DC output. The following subsections address different challenges and propose solutions in the context of controlling PPC.

3.3.1 Active DC Bias Correction

DC bias can be a challenging issue in DAB-based converters [30]. DC bias is typically caused by jitter in the converter's control signal, which can cause the on and off times of the switches to be slightly different [30]. If this is not rectified, then the DC bias can increase so that the converter becomes uncontrollable. Additionally, excessive DC bias current increases the device stress current and increases the risk of magnetic saturation [30]. This could potentially lead to the destruction of the converter. The DAB transformer design is scaled to perform within a specified magnetic field density range. The transformer core's magnetic flux density depends on the amplitude of the AC waveform in the windings. When DC bias is introduced into the winding current, the magnetic flux density deviates from the specified range and might lead to core saturation. Additionally, the elevated DC current values can lead to excess heating of the windings, jeopardizing the balance between the generated and dissipated heat in the transformer. This can potentially lead the transformer core out of the designated temperature range and cause additional issues with its performance.

DC bias issue in the transformer is often solved with the addition of a DC bias capacitor [31]. A capacitor or a capacitor bank is then connected in series with one of the transformer windings. This blocks the passage of DC current passively. However, in practice, this increases losses in the converter and decreases its power density because of the addition of extra components [30]. Another approach is to solve the DC bias issue through active control [30]. The proposed active control regulates the DC component of the transformer current. To understand better how active DC bias control works, the switching signal generation is explained together with the DC bias control. This is illustrated in Figure 12. As can be seen from the figure, the switching signals are generated separately for each full bridge. The switching signal generation starts with a carrier signal. Based on the carrier signal, the sine waves are generated. The sine waves are then fed to comparators, which detect when the wave is on the positive side or negative side of the Y axis. Therefore the comparators output rectangular waveforms based on the waveforms prior, to control the switches. The initial carrier signal can influenced by the converter's control variable. By influencing the carrier signal's offset, the power transfer of the converter can be controlled. The power transfer in the proposed converter's control circuit is based on independent control of the phase shift of the secondary side full bridge relative to the primary side full bridge.

In order to achieve active control over DC bias, the jitter in the control signal can be alleviated by continuously monitoring the DC bias in the transformer windings and using that data to adjust the switching timings. As illustrated in Figure 12, it can be realized by

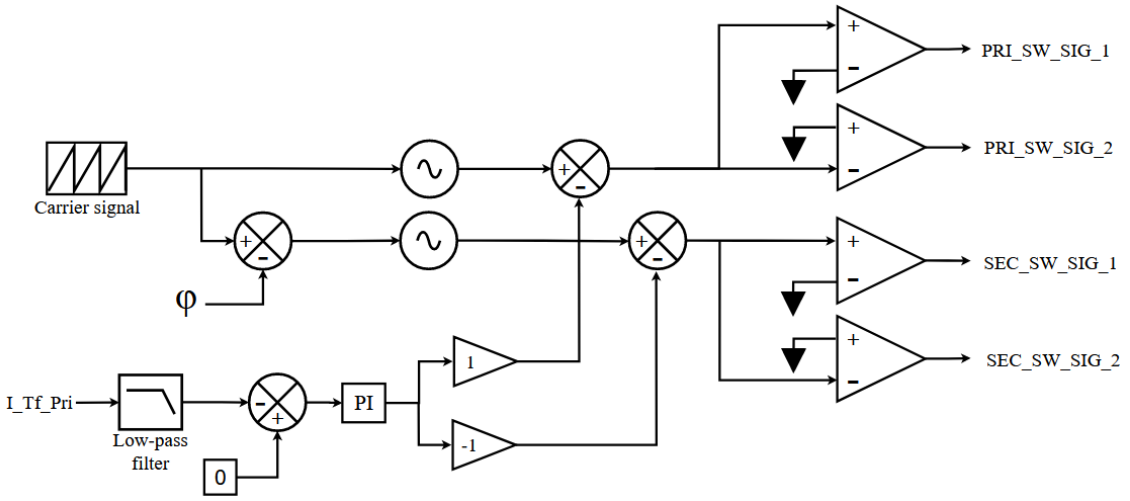

Figure 12. Control diagram for controlling the DC bias in the transformer.

adjusting the offset of the sinusoidal waveforms along the Y-axis to correct the switching timings.

This correcting signal can be generated using the following method. The current in a transformer winding is measured to monitor the bias current. Here, the primary transformer winding current is used. The transformer current is measured, and the measured signal is filtered to an extent where only the DC component is left. The DC component is fed to a PI controller that helps to correct the sinusoidal signal, which is used for switching signal generation. The proportional and integral gains of the PI regulator were acquired using a trial-and-error method. This solution fixes the DC bias issue without adding extra components like capacitors. It should be mentioned that a current sensor together with analog to digital converter is required as additional components with this approach. In some instances, this may influence the control complexity and cost. However, the energy density of the converter is not reduced compared to a conventional solution [30]. This method was validated through simulations involving both the DAB converter and DAB-based PPC. The entirety of the DC bias current is not canceled as occasionally slight DC bias still occurs. However, the DC bias occurs in both directions at a frequency much lower than the switching frequency. This allows the system to remain stable throughout its operation. It should be mentioned that this control method is used in all simulations containing a DAB in this thesis to avoid using a DC-bias-blocking capacitor.

3.3.2 PPC Control for a DC-DC Operation with Stable DC Output Voltage

The control of PPC is designed around controlling the battery current. The current is measured and filtered through a 2nd order low-pass filter to improve the converter's controllability. The difference between the filtered current values and the reference current values is then fed into a PI controller. The proportional and integral gain values for this application were acquired using a trial-and-error approach. The PI controller is tuned to respond well to the reference current with minimal overshoot. The output of the PI is supplemented with a saturation limiter, which eliminates the possibility that the phase angle leaves the set boundaries. The control diagram for controlling PPC with a stable DC output is brought out in Figure 13.

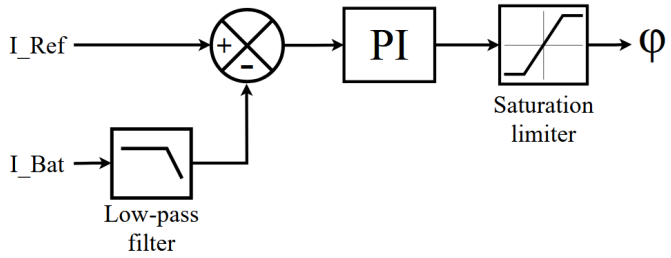

Figure 13. Control diagram for PPC with a stable DC output.

The phase angle is used as a control variable to create a phase shift between the primary and secondary bridges by introducing a shift to the secondary bridge carrier signal. This can be seen from Figure 12. The advantage of this control method proved to be its ease of implementation and a relatively fast response time to the changes in the reference current.

3.3.3 Active AC Current Rejection in PPC Control

The control of a PPC with a fluctuating output voltage can be a challenging endeavor. However, in the case of the MMC submodules, the frequency and amplitude of the voltage change can be determined before the realization of the converter. In MMCs, the voltage ripple at the grid frequency can be measured across each submodule [17]. This was discussed in more depth in the previous chapter. In order to account for this fluctuating voltage on a PPC level and provide constant power while protecting the battery from low-frequency voltage ripple, it is necessary to synchronize the control signal with the disturbance. This can be achieved by improving the control structure that was introduced in the previous subsection. The PI controller used in simulating the controllers at hand was not fast enough to compensate for such rapid changes in the output voltage posed by

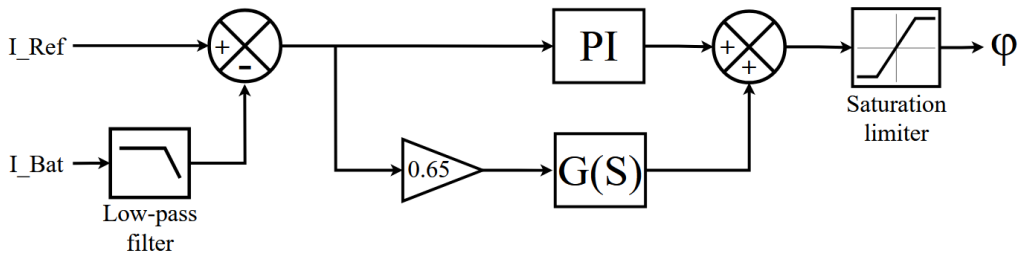

Figure 14. Control diagram for PPC with AC current ripple rejection.

the 50 Hz disturbance. Therefore, another kind of control structure was required. For this reason, a resonant controller was introduced in addition to the PI controller.

The resonant controller can track a sinusoidal control variable, which is in phase with the sinusoidal output voltage waveform, with zero phase error. This helps to reject the sinusoidal currents from the battery, improving the response of the control circuit. The resonant controller is connected in a feed-forward configuration with a PI controller. Both controllers react to the difference between a filtered battery current and a reference battery current value. The output of the feed-forward connection is supplemented with a saturation limiter, which ensures that the control variable does not go out of bounds. The values for the proportional, integral, and resonant gains in this control loop were acquired using a trial-and-error approach. A control diagram for the AC current rejection control for PPC is brought out in Figure 14.

This control structure comprises two main parts connected in parallel: a resonant controller configured to operate at 50 Hz and a PI controller configured to react to the changes in the reference current. The resonant controller is described as a transfer function in this application. The transfer function with its numeric values is brought out in Equation 3.6.

$$G(S) = \frac{Y(S)}{E(S)} = \frac{4\pi s}{s^2 + 4\pi s + (2\pi 50)^2} \tag{3.6}$$

This transfer function is tuned to perform best at a frequency of 50 Hz. Therefore, it should be noted that this method of ripple compensation assumes that the frequency of the disturbance does not deviate from its nominal frequency. If a deviation from the nominal frequency is expected, then a phase-locked loop would be required to track the frequency in real time.

3.4 Verification of the Control Systems

The simulation of PPC, which included accurate battery current control, active DC bias correction, and AC ripple compensation, was completed through several key stages. All conducted simulations were based on the same application requirements. The first step was to achieve accurate battery current control in a converter with a stable DC output. This was first implemented in a DAB converter simulation. Once a stable control was achieved, an active DC bias correction control method was implemented next. Once the DAB converter was operational, the simulation model was reconfigured for PPC. Additionally, the control system architecture of DAB was carried over to PPC, and the gains of the control system were modified.

AC ripple compensation control system verification is described using the example of PPC. Due to its unique topology, there is a series capacitor that separates the secondary side output from the input. In other words, this capacitor's voltage should oscillate at the same frequency and magnitude as an MMC submodule, but with a 180°, to reject the grid-frequency current ripple at the battery bank terminals. AC ripple compensation is utilized in all converters in this work, but the impact is highlighted most in the case of PPC.

This section covers the creation of these simulations and the verification of the control system functionality. Additionally, the process of proving the feasibility of integrating PPC into an MMC submodule is investigated. The simulations were created using MATLAB/Simulink simulation software environment. Three different simulations are described in the following subsections.

3.4.1 Simulation Test Setups

Simulation models of three different converter topologies were created. The simulation of the DAB converter was created first. From there, by modifying the model, a PPC simulation was created. Lastly, a simulation was made for the half-bridge converter. The development of the half-bridge converter simulation and its control system is not separately discussed. This is because this model is needed only to conduct comparisons. Moreover, it does not share a common active power part with the PPC and DAB converter. The simulation model of the half-bridge converter is separately brought out and described in Appendix 4 and Chapter 4. Moreover, the component values and control coefficients of the half-bridge converter simulation model are brought out in Table 1.

Table 1. Component values and converter parameters of half-bridge converter simulation model.

Components and converter parameters	**Value**
L (mH)	2
C_{in} (uF)	500
PI controller - Proportional gain	0.003
PI controller - Integral gain	0.1
F_{sw} (kHz)	10
Power (kW)	40

Additionally, the transfer function of the resonant controller used in the half-bridge converter simulation model is depicted in Equation 3.7.

$$G(S) = \frac{s}{s^2 + (2\pi 50)^2} \tag{3.7}$$

This transfer function encompasses the frequency of the AC disturbance and is preceded by a multiplier of 0.1 in the simulation model.

The control systems for controlling PPC and DAB with both varying and stable DC outputs were described in the previous section. Additionally, the necessary steps to reach the required solution were laid out. In order to verify the proposed control methods and the converter's component values and study the operation of the converters, working simulations of DAB and PPC were created. Moreover, the component values and converter parameters of the DAB converter simulation model are brought out in Table 2, and the component values and converter parameters of the PPC simulation model are brought out in Table 3. The additional goal of these simulations is to produce working simulations while staying within the application requirements and the design constraints presented in Chapter 4.

Table 2. Component values and converter parameters of DAB converter simulation model.

Components and converter parameters	**Value**
L_{leak} (uH)	80
C_{in} (uF)	300
C_{out} (uF)	200
L_{out} (uH)	10
Transformer Turns Ratio	4:5
PI controller - Proportional gain	0.005
PI controller - Integral gain	2
F_{sw} (kHz)	10
Power (kW)	40

Table 3. Component values and converter parameters of PPC simulation model.

Components and converter parameters	**Value**
L_{leak} (uH)	700
C_{in} (uF)	300
C_{out} (uF)	100
Transformer Turns Ratio	4:1
PI controller - Proportional gain	0.008
PI controller - Integral gain	6
F_{sw} (kHz)	10
Power (kW)	40

Transfer functions utilized in both PPC and DAB converter simulation models are identical and are preceded by a multiplier of 0.65. The corresponding transfer function is brought out in Subsection 3.3.3.

All simulation models in Simulink were configured to operate with a time step of 100 ns. This step size was selected considering the required precision and acceptable speed of the simulations. The speed is essential to increase the amount of design iterations that could be done. The common part between the three simulation models of all converters was the input and output. The input was simulated using an ideal DC voltage source with a series impedance to emulate the behavior of a battery bank. The output was emulated using an ideal DC voltage source together with a series AC voltage source to emulate the behavior of MMC submodule's capacitor bus. The specific simulation models created and used in

this work are further discussed and visualized in Appendix 4. Additionally, the component values are specified in Chapter 4 - Benchmarking of the Converters. The simulations were needed to verify the feasibility of PPC utilization in the proposed application and to conduct comparisons. Furthermore, the data collected from these simulations was used to conduct the designs of the converters.

The initial converter simulation models were created with a stable DC output. The simulation model of the DAB converter, together with its control system, was designed first. This is because its operation is extensively covered in literature, which helps to achieve a workable model faster. Then, the simulation model of PPC was designed based on the latter. The reconfiguration of the DAB converter into PPC included modifications to the components of the converter and its control system. Lastly, as PPC is, in its nature, a more sensitive of the converters at hand to a voltage ripple at the output, the control system for compensating the ripple was designed next and was added to its simulation model. The results from these simulations and the verification of these control systems are presented in the following subsections.

3.4.2 Simulation Study of DAB Converter

As discussed in previous subsections, a stable simulation of a DAB is necessary to move forward with PPC simulations, as the proposed PPC topology is based on a DAB. The initial simulations with DAB were created using a steady DC output. DAB converter topology is introduced in 2.2.2 and its simulation model is discussed in Appendix 4. The simulation results are presented below. The converter's battery current during its operation is brought out in Figure 15. It can be seen that the bidirectional operation of the DAB was achieved in a controlled way.

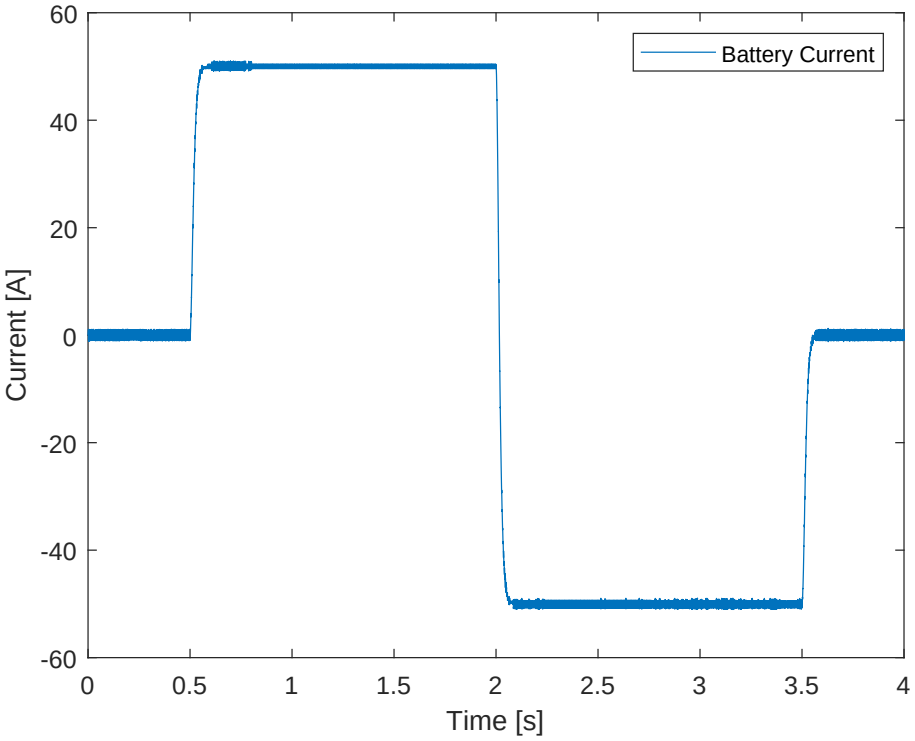

Figure 15. Battery current during the bidirectional operation of DAB.

The current waveforms in the transformer windings are measured during this operation and visualized in Figure 16. It can be seen that DC-bias current is not an issue in the transformer windings during its operation. Moreover, this simulation was also run for an extended period of time to detect the occurrence of DC-bias currents, and the findings are the same.

The control variable during this simulation is shown in Figure 17.

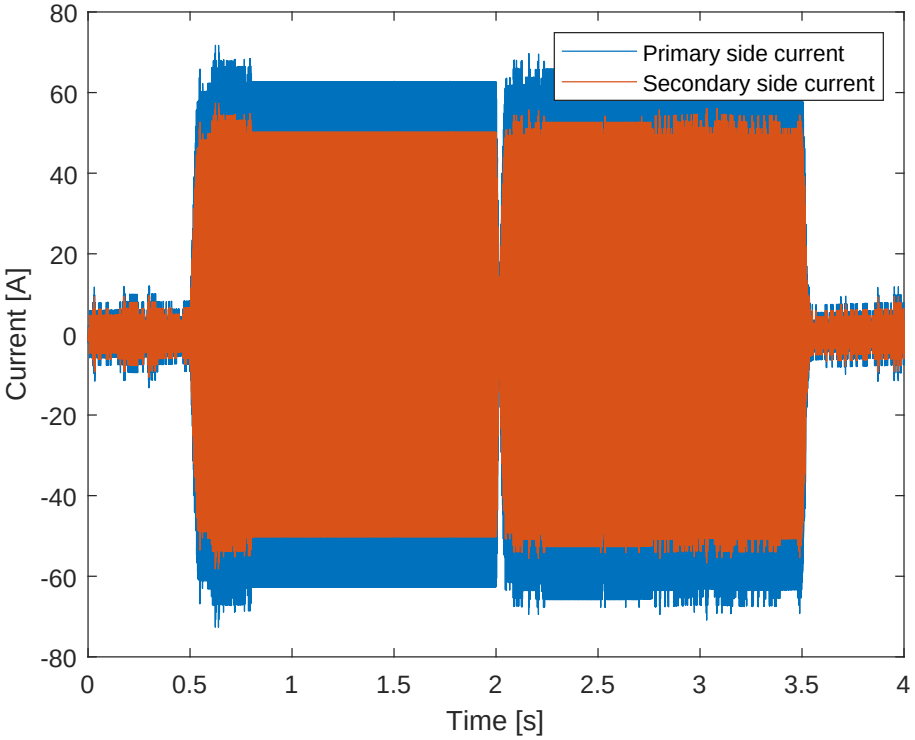

Figure 16. Waveforms in DAB converter transformer's primary and secondary windings.

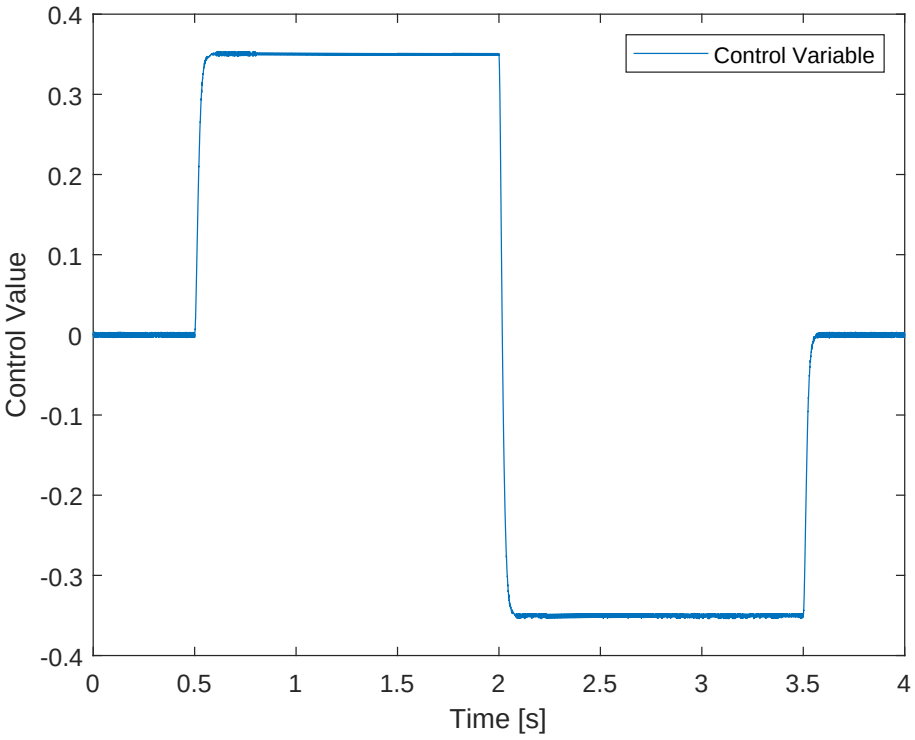

Figure 17. Control variable during DAB operation.

3.4.3 Simulation Study of PPC

In order to implement PPC simulation and validate the control methods and component values, the DAB simulation needed to be reconfigured. This reconfiguration involves changing the connections for the power paths, changing the transformer turns ratio, changing the component values, and updating the control methods. The initial PPC simulations were created using a steady DC output. PPC topology is visualized in Figure 11 and its simulation model is discussed in Appendix 4. The simulation results are presented below. The battery current during the converter's operation is brought out in Figure 18. It can be seen that the bidirectional operation of PPC was achieved in a controlled way.

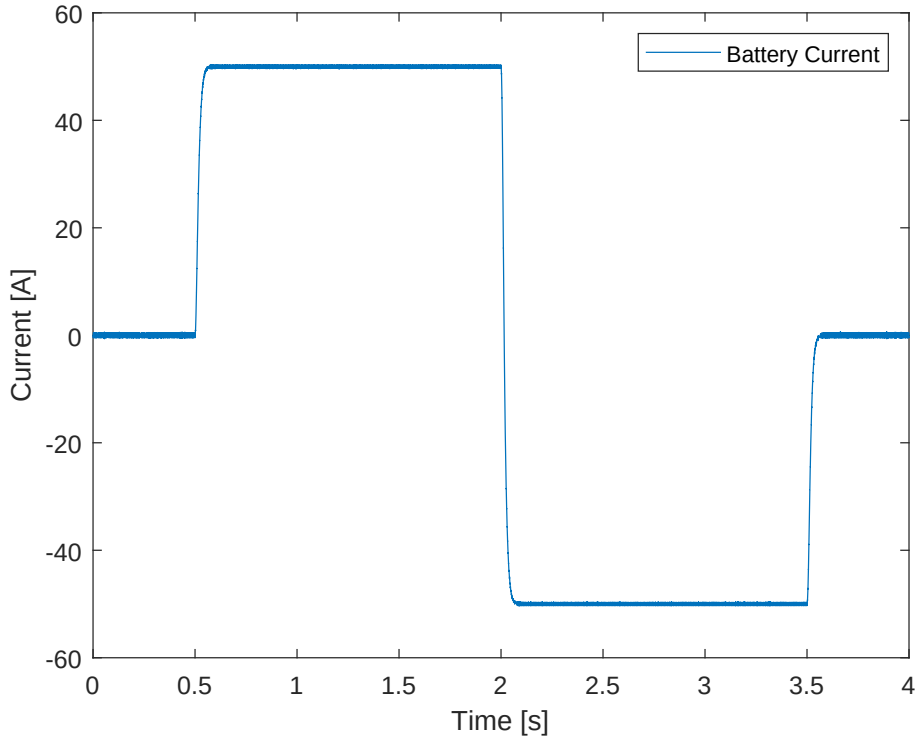

Figure 18. Battery current during the bidirectional operation of PPC.

The current waveforms measured in the transformer windings during the operation of the converter are shown in Figure 19. It can be seen that the DC-bias current is not an issue in the transformer windings during its operation.

The control variable during this simulation is shown in Figure 20.

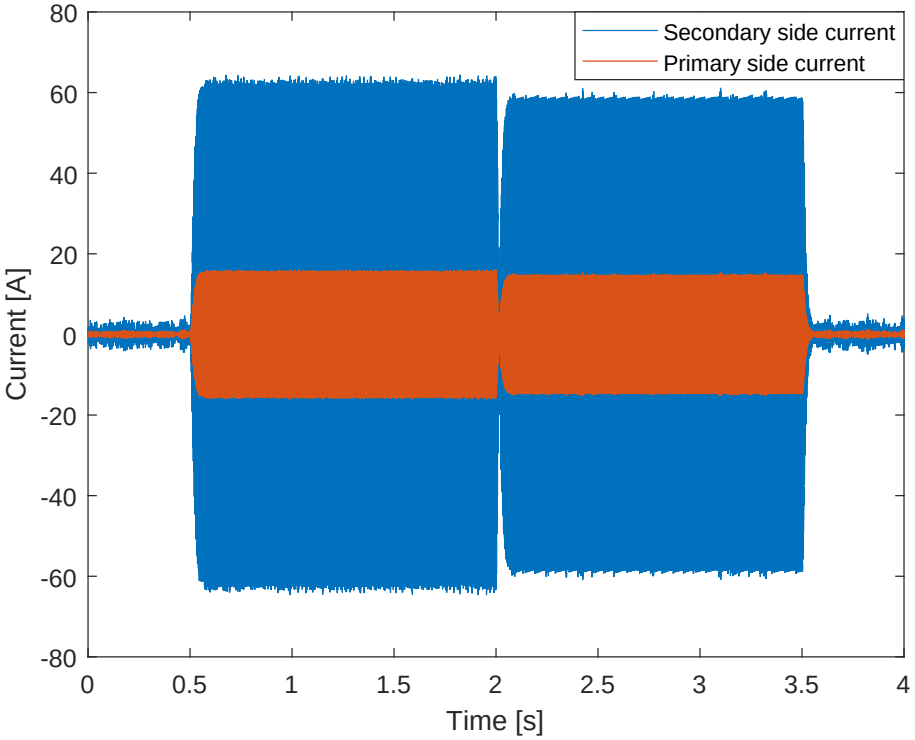

Figure 19. Waveforms in PPC transformer's primary and secondary windings.

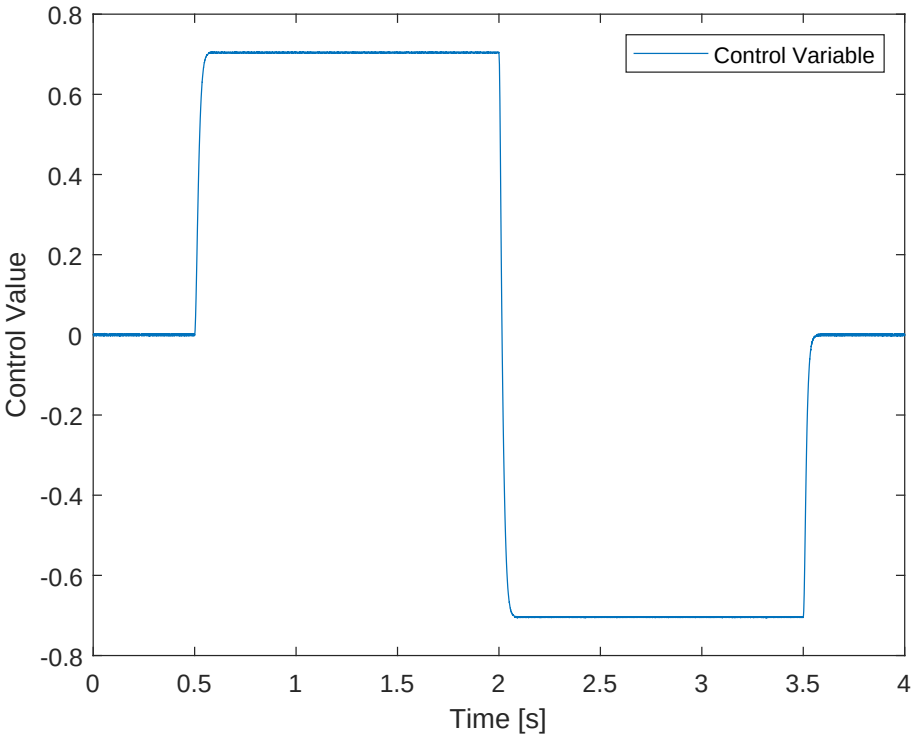

Figure 20. Control variable during PPC operation.

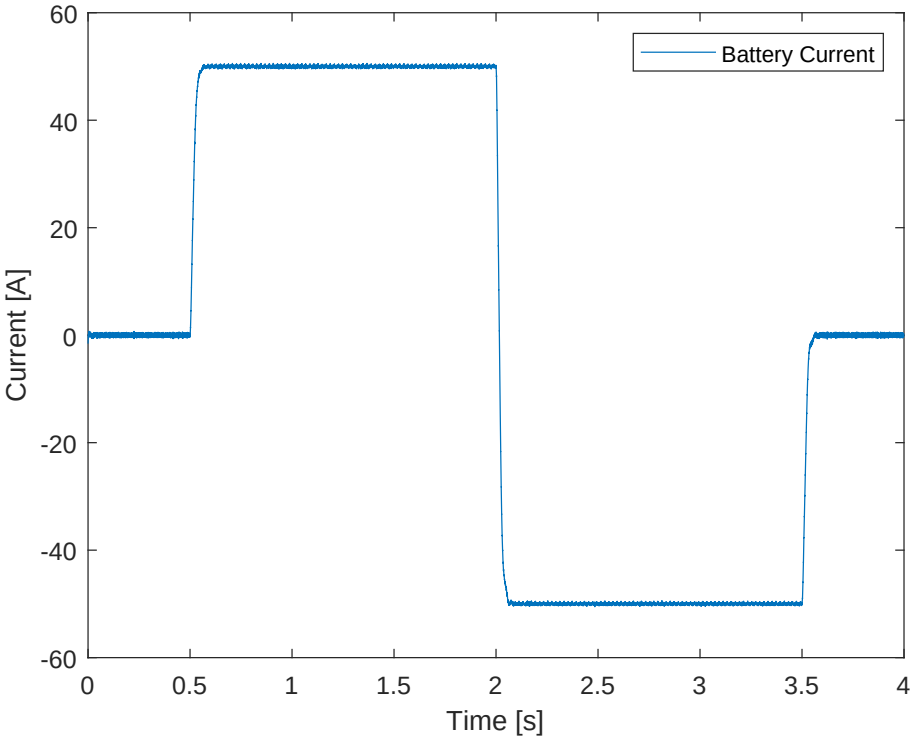

Figure 21. Battery current during the bidirectional operation of PPC with an AC component in the output.

After a controlled PPC operation was achieved with a stable DC output, an AC component was introduced to the output. The differences in control for this were detailed in Subsections 3.3.3 and 3.3.2. The simulation results are presented below. The battery current is brought out in Figure 21. It can be seen that the bidirectional operation of PPC was achieved in a controlled way. Moreover, the AC component is being compensated with the help of the control method and it is not present in the battery current.

A good way to visualize the impact of this control method is to start the converter later in the simulation. This is illustrated in Figure 22 where the converter is activated at the time instant of 0.25 s. In the first stage, an AC waveform can be seen in the battery current. This is the period, where the PPC is not activated. In this case, the sinusoidal voltage component passes through the capacitors in the system and causes AC currents to flow into the battery. The amplitude of the AC current is directly influenced by the size of the capacitor used on the output of the PPC. Although in this design, the AC component is not significant, in other possible applications, larger capacitors could be needed, and the benefit becomes more noticeable. Once the PPC is turned on, the AC component is actively rejected with the help of the compensating control method.

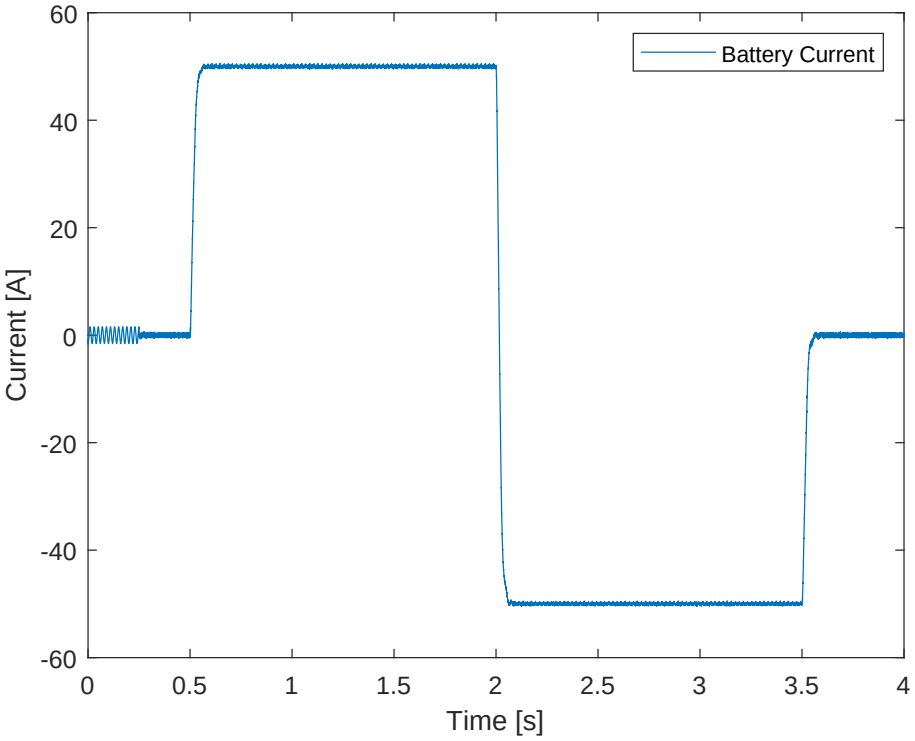

Figure 22. Battery current during the bidirectional operation of PPC with an AC component in the output and a delayed startup.

Transformer current waveforms measured during PPC operation with an output with an AC element are shown in Figure 23. It can be seen that the DC bias in the transformer current is not an issue. Additionally, the periodicity of the disturbance AC signal carries over to the current waveforms of the transformer. This occurs because the battery current is being controlled, and the effects of AC current rejection can be measured in the transformer.

The control variable during this simulation is shown in Figure 24.

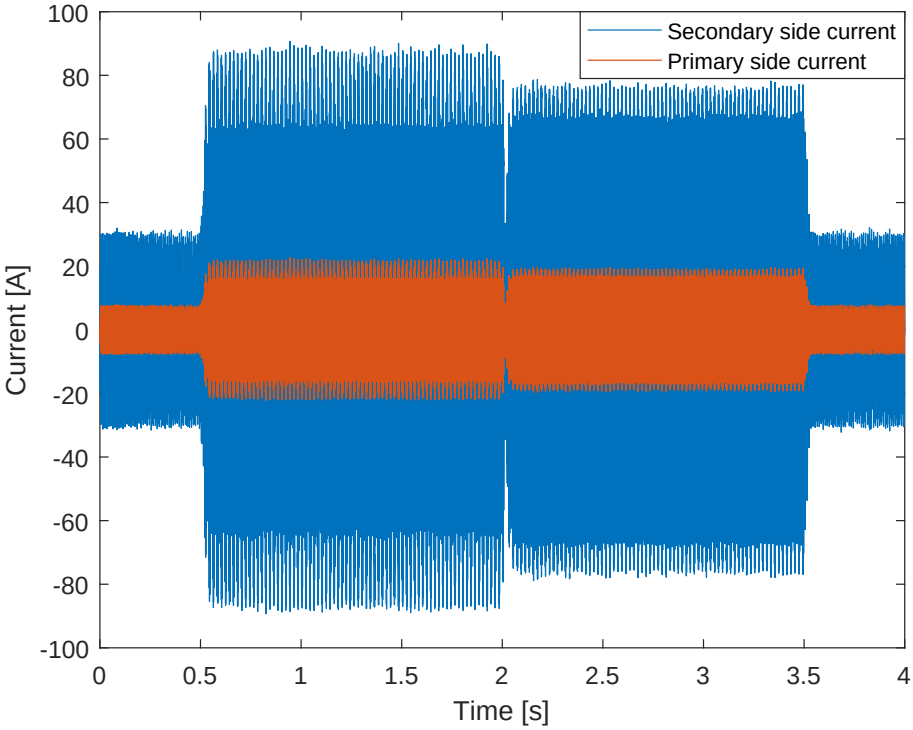

Figure 23. PPC transformer primary and secondary waveforms with an AC component in the output.

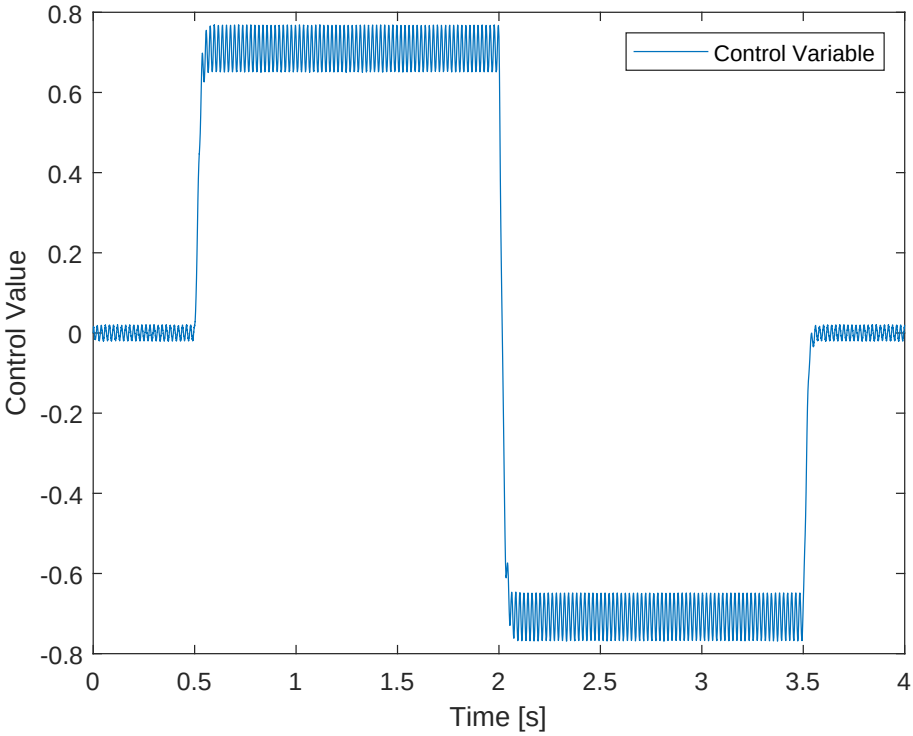

Figure 24. Control variable during PPC operation with an AC component in the output.

3.4.4 Practical Considerations

To design physical power converters based on their simulation models, one must also consider the practical considerations for these converters. Certain aspects of the converter can be missed with even sophisticated simulation models. These considerations should not be neglected when aiming to predict the converter losses accurately and to achieve a successful converter design.

Consideration of Physical Electrical Connections

The resistance of the electrical connections can add a measurable amount of losses to the system. However, the DC resistances of electrical connections can be estimated only after the converter design is completed in CAD software or measured directly from a prototype. There are additional parasitic components that, by being present in the circuit, can significantly influence the operation of the converter both in terms of stability and losses. These parasitic components can be described in simulations as impedances across a transmission line to allow for optimization of the converter design to account for this. However, in a converter where most of the connections are achieved using wire and busbar connectors with a complicated geometry regarding analysis, this cannot be accurately estimated without building the converter. Moreover, the impact of the aforementioned factors depends on the design choices made in the physical design of the converters. Hence, these factors fall outside the scope of this work since the design focuses solely on the primary power converter components, without an extensive consideration of internal connections.

Considerations in Component Selection

In addition to component selection, a complete converter design should take into account the layout of the electrical connections to enable efficient and viable connections within the converter. The best method for achieving this is by creating a 3D model of the converter in CAD software to accurately assess the mechanical compatibility of different components and demonstrate their placement and connections. Furthermore, this method allows to accurately estimate the overall volume of the converter. However, this method is out of the scope of this thesis, and a simplified approach is employed to result in a realistic component selection. Moreover, the volumes of the converters are instead calculated as the sum of their components's volumes. For achieving a realistic component selection, the compatibility of different components that must fit together shall be considered. Additionally, the dimensions of the components and their proportions should be evaluated for them to be realistic. This is important to avoid disproportionally long or wide components that don't necessarily add much to the converter's volume; however, they cannot be utilized in a

practical design.

Potential mechanical mismatches can occur in different component categories. However, with careful consideration, they can be avoided. As an example, when establishing a cooling solution for the switches, it is important to ensure the compatibility of the switches with the cooling solution both mechanically and thermally, as detailed in Section 4.3. Moreover, the physical placement of the switches must also be taken into account for practical electrical connections. Similar considerations also apply to the configuration of the capacitor banks and in the design of magnetics. The converter volume constraint described in Chapter 4, necessitates diligent component selection concerning their mechanical dimensions. The transformer designs in PPC and DAB converters and the inductor design in half-bridge converters contribute significantly to the converters' mechanical dimensions and their electrical performance. When considering the transformers used in PPC and DAB converters, their leakage inductance values are important parameters in their designs. Leakage inductance, depending on its value, is sometimes achieved using a combination of embedded leakage inductance and an external inductor [32]. However, it is recommended to achieve the design goals using only embedded leakage inductance [32]. This means that the leakage inductance value is achieved within the transformer itself, simplifying the converter construction, reducing its size, and reducing losses. The value of embedded leakage inductance is fully dependent on transformer geometry and its windings configuration and is, therefore, difficult to accurately assess without measuring it from a built prototype. For this reason, in this work, it is assumed that the target leakage inductance can be fully achieved using embedded leakage inductance. The component selection, magnetics design, and capacitor selection are further discussed in Chapter 4 and Appendix 2.

Further Considerations

The cooling consideration is an important aspect of converter design. This aspect must not be overlooked when aiming to achieve a successful converter design and compare the converters fairly. This design aspect is considered in this work and is further detailed in Subsection 4.3.

Keeping in mind the application at hand, there are further practical considerations. The DC-DC converters separate the battery bank from an MMC submodule. As the batteries don't tolerate system faults well, it is necessary to protect them. A fault can occur in the MMC submodule and cause a short circuit at the output of the converter. Galvanic isolation, present in DAB converters, protects the batteries from such faults. However, a fault can also occur within the converter itself. This means that in the event of a short circuit within the converter, galvanic isolation does not protect the batteries. Therefore,

to ensure the protection of batteries, a dedicated protection circuit is required. Battery protection can be achieved using solid-state switches based on different semiconductor technologies isolating the batteries in case of a fault. This issue is further discussed in [33]. The protection solution does not contribute significantly to the overall volume of the converter, but it does increase its cost and losses. As all converters require this solution, this aspect was not considered in the converter designs nor their comparisons in this work.

Concluding the exploration of practical considerations in power converter design, the subsequent chapter introduces the methodology for comparing converters and presents the analysis along with comparison results, further extending upon the foundational principles elucidated in this section.

4. Benchmarking of the Converters

So far, this work has focused on giving an overview of the technologies used in ESS and demonstrating the suitability of PPC through simulations. This section aims to lay a foundation for converter comparison considering the requirements of the ESS application. This chapter concludes with an overview of the advantages and disadvantages of PPC, DAB, and half-bridge converters in the application in question. These converter topologies are introduced in Section 2.2. The main objective of comparisons is to gather critical information about these converters and demonstrate which technologies are the most promising for such applications.

4.1 Case Study

The application and its conditions, in which the three converters were tested, were identical. The use case for a bidirectional DC-DC power converter is the following. A battery pack with a total DC voltage of 800 V supplies an MMC submodule with a constant power of 40 kW. Additionally, the battery pack retrieves the constant power as well. It must be a bidirectional power converter with a high degree of controllability. In this case study, the goal is to emulate the conditions in an ES integration solution in MMC submodules. The considered topologies are compared, and the results are presented in the last section of this chapter.

4.1.1 Description of the Use Case

The amount of power to be supplied from the ESS through a single MMC into the system has been proposed to be 3.6 MW. However, the ESS is distributed among the MMC's submodules. In this MMC, there are 15 submodules in each arm, and there are 6 arms. This results that the amount of power supplied into one submodule is 40 kW. As discussed previously, the ESS must control the flow of energy bi-directionally. As the control of energy is realized by the DC-DC converters used in the ESS, the power rating of one converter must be at least 40 kW.

In order to assess if PPCs have an advantage over common FPC topologies, a fair comparison must be provided. The use case in which the converters are compared is described in the previous chapter. The input of the converter is a battery bank with a nominal voltage of 800 V. The output of the converters is a 1 kV DC source with a 50 V AC voltage

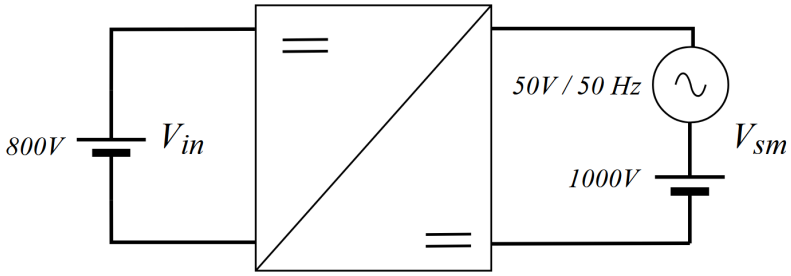

Figure 25. Use case for comparing the converters.

component. This use case for converter comparison is illustrated in Figure 25. The MMC submodule is simulated using an ideal DC source in series with an AC source. The voltage waveform of the emulated MMC submodule is shown in Figure 26.

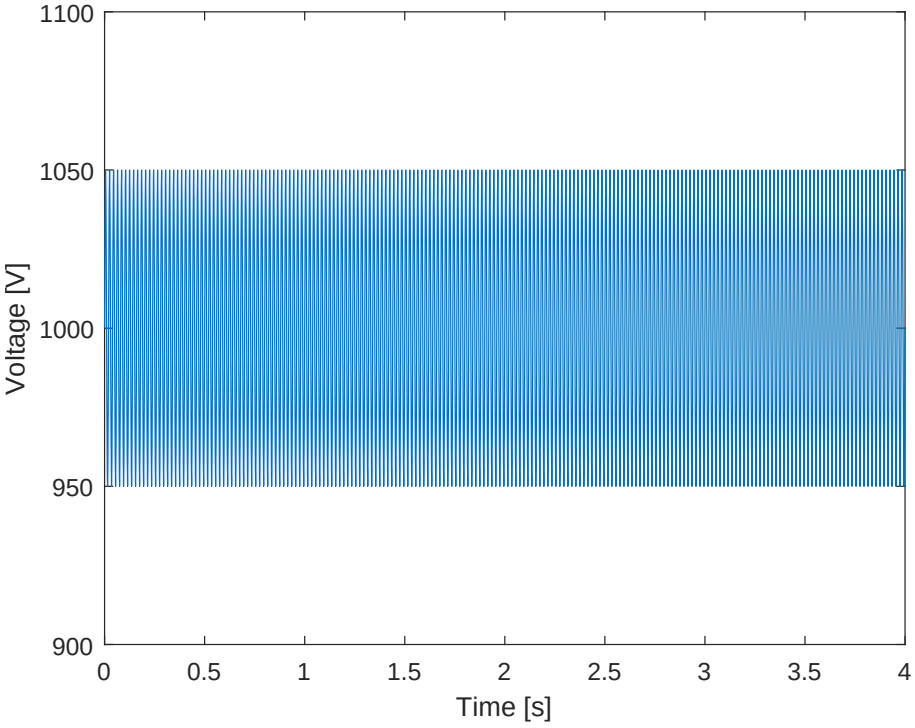

Figure 26. Voltage on the emulated MMC submodule.

The battery current in the simulations follows the same reference current waveform with all converters. This current waveform is brought out in Figure 27.

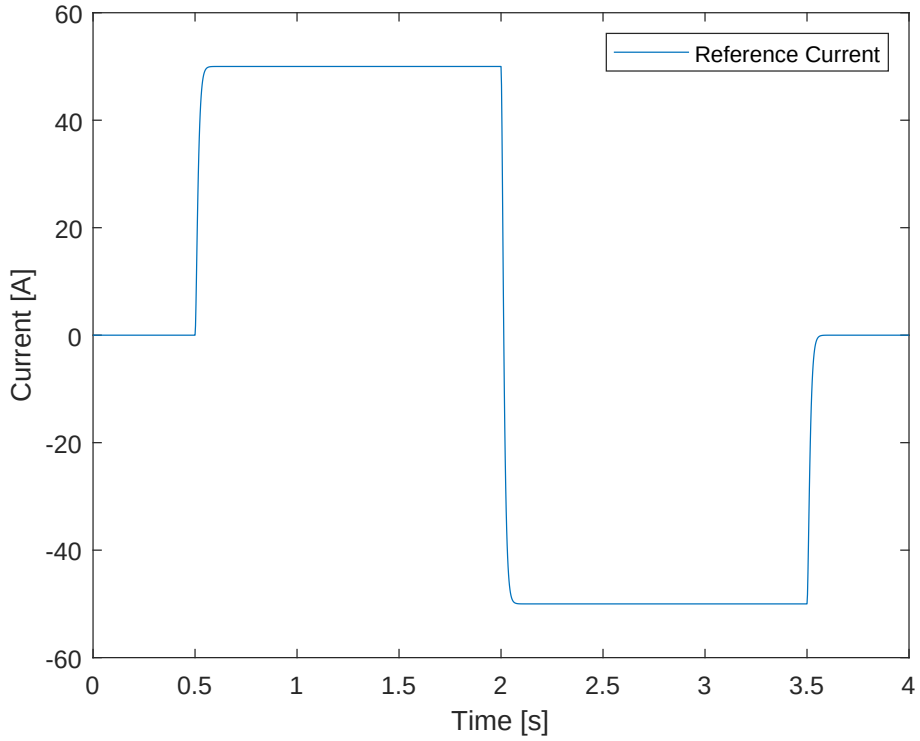

Figure 27. Reference battery current waveform.

4.1.2 Converter Design Constraints

In addition to the application description, which sets the power and voltage goals for the converter designs, constraints were proposed to set specific limits for the three converters. This helps to reduce free variables and the iterations in the power converter design process. Additionally, the constraints help to achieve more comparable converter designs and take into account different practical considerations. The constraints are further discussed below.

Semiconductor Switches

The limitations of semiconductor technologies set the first constraint. Considering the required power level, system voltages, and currents, silicon carbide (SiC) metal-oxide-semiconductor field-effect transistors (MOSFETs) can be a suitable choice. This is especially true when higher switching frequencies are required [34]. SiC MOSFETs are widely used in the automotive industry, and their reliability is proven in the industry [35]. A different semiconductor technology that could be considered is the insulated-gate bipolar transistor (IGBT). Compared to SiC MOSFETs, they are typically used in lower frequency applications because their switching losses increase significantly with frequency [34]. They are widely used in high-power applications such as renewable energy generation, automotive, and different high-power converter stations [36]. Their reliability is also proven in the field [36]. More importantly, IGBT modules are also available in press pack

packages [36]. Press pack package is a semiconductor packaging technology where the semiconductor substrate is directly fused together to the connection plate of the IGBT module [36]. This increases reliability, and its resistance to thermal cycling [36]. In a typical semiconductor package, the silicon substrate is connected to the connection pads using electrical bond wires [36]. During a thermal cycle, the bond wires experience mechanical stress, which, over numerous cycles, degrade the connection strength to the substrate and can cause the bond wire connection to fail [36]. This is a common failure point of semiconductor devices [37]. In a press pack device, the tolerance for thermal cycling is improved [36]. As an additional benefit, the resistance of the contact leads is reduced [36]. In the power converters used in particle accelerators at CERN, thermal cycling is a significant consideration [38]. This is because the switches in those converters experience considerably more thermal cycles over the same time period when compared to a typical industry application [38]. Therefore, to reduce the need for converter maintenance and increase their longevity, IGBTs in press pack packages are a better-suited choice for pulsed power converters. For the above reasons, SiC MOSFETs are unsuitable, and IGBT technology fits better for this application.

Frequency

The second constraint is the switching frequency. It is known that the highest losses in these converters come from losses in the switches [39]. Switching frequency has a strong influence over the losses in the switches [39]. To compare the topologies fairly, a single switching frequency shall be used in all three converters. On the one hand, the lowest practical frequency that could be used is influenced mainly by the volume constraint of the converter as the passive components' sizes increase with decreased frequency. On the other hand, the highest practical frequency that could be used is limited by the semiconductor switches' technology, acceptable losses, EMC considerations, and available cooling solutions. Acceptable losses and available cooling solutions are not considered initially as the design of the converter is conducted iteratively, and the discrepancies can be solved. EMC considerations, which are an important factor in the converter design of a high-power converter, set a practical frequency limit for the converters. Higher frequencies in high-power applications can have a detrimental impact on EMC performance, leading to additional challenges and costs in EMC mitigation efforts [40]. However, this factor cannot be correctly evaluated before building the converter. Therefore, based on the expertise at CERN and the results reported in [34], the higher frequency limit was set to 20 kHz.

Battery Ripple Current

The third constraint is the limit of the battery ripple current. The maximum current ripple in the battery pack was limited to make conclusive comparisons. Moreover, this means that

when conducting comparisons, the performance of the converters is on a comparable level. The maximum allowed peak-to-peak ripple current on the battery was set to 10% of the nominal current. This constraint helps to compare converters more fairly, as the converter's impact on the battery will be similar. Additionally, the battery input filtering inductor is a common component for all converters. The 10% ripple current is realistically achievable with the converters at hand. Moreover, a lower current ripple on the controlled current simplifies the achievement of stable control. A higher ripple current has been known to complicate the accurate battery current control. This initial limit is considered to be the worst case. However, when the converter designs allow to improve the current ripple with little to no additional costs and complexities, then it shall be pursued.

Volume

The fourth constraint to limit the volume of the converters is necessary for directing the converter design to be suitable for integration purposes. The volume requirement comes from the need to practically fit the converters aside from the MMC's submodules without unnecessarily increasing the size of the MMC cabinet. In other words, the size of the MMC submodules must not be larger than the converter that interfaces batteries to the submodule. Additionally, mechanical constraints help to achieve a design that optimizes the length of connections and accessibility for maintenance. On top of that, it helps to pursue one of the project's goals to lower the costs and minimize losses. Moreover, another goal of minimizing the use of materials to minimize environmental impact is also pursued.

Limiting the volume of the converter can additionally help to achieve more comparable converter designs regarding cost and efficiency. A minimum power density of 5 W/cm3 was chosen as a constraint for the design of three converters. This translates to a maximum volume of 10 liters. This power density value was chosen based on the converter power level and the dimensional restrictions for DC-DC converter integration into MMC.

4.1.3 Dimensioning of Power Converters

The available volume for a converter design influences most design aspects of the converter. In order to fit all three converters inside the volume constraint, it is helpful to start with volume estimations for components that account for most of the total volume. The majority of volume in a power converter is typically taken up by the magnetics, cooling, and capacitors [41]. Because dimensioning of power converters can be an iterative process, the volume dedicated to cooling is not considered at this stage.

For all three topologies, the switches were selected according to best practices. As

mentioned in the previous subsection, the chosen semiconductor switch technology was the IGBT. An empirical approach of having a 50% margin between the simulation values and the IGBT's datasheet values was followed. The switches can be changed to optimize the design further. However, at this stage, when the first prototypes had not yet been conceived, more conservative values were selected for IGBTs.

When considering the set ripple current constraint, it becomes necessary to evaluate the passive filtering elements separating the battery from the converters. In order to have comparable ripple currents on the battery, filtering elements were chosen to filter out switching current ripple on the battery side. In series with the battery pack, a small resistor and an inductor were added to create a more realistic simulation. The inductances and resistances were selected to be equal for all converters. Additional filtering elements that were used in each of the three converters were capacitors, creating an LC filter at the output of the battery pack. Capacitances were selected individually for each of the converter topologies. An important consideration when selecting these components was their volume and the impact that the increase in component values had on the ripple current. Also, it was considered what minimum number of real capacitors connected in parallel can handle the root mean square value of the switching current ripple component.

The magnetic components of all three converters were calculated to suit the required applications and help to achieve accurate loss calculations and volume estimations. The magnetics calculations are discussed in detail in Appendix 2. There, the process of choosing the materials and configuring the windings is brought out.

4.2 Simulation Results

This section presents the comparable results from the simulations. The simulation models used are described in Appendix 4. Using simulation results, it becomes possible to demonstrate the slight differences in their operation and control. When looking at the battery current tracking, it can be seen from Figures 28, 29 and 30, that the battery current tracking functionality is achieved with all converters. Considering the design constraints detailed above and the available control strategies, there remained small differences between the controlled waveforms.

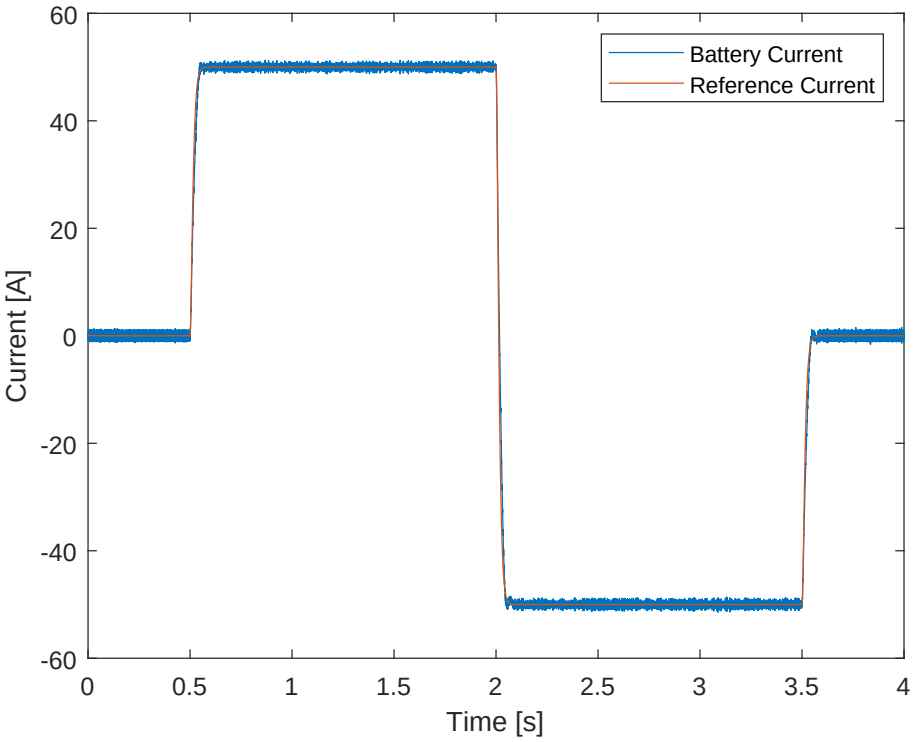

Figure 28. Controlled battery current in the DAB with the reference current.

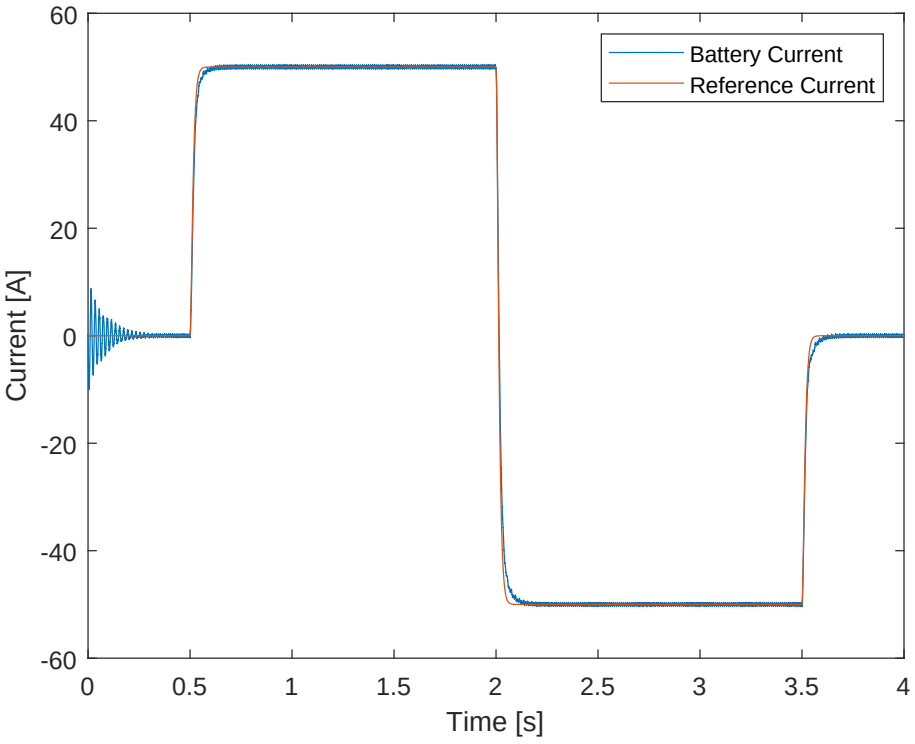

Figure 29. Controlled battery current in the half-bridge converter with the reference current.

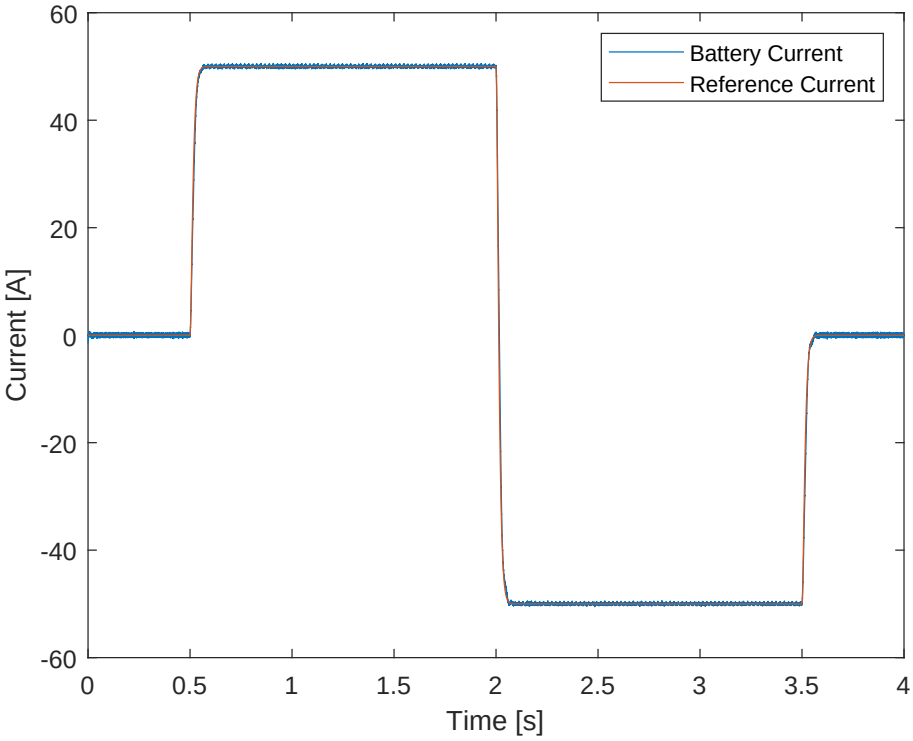

Figure 30. Controlled battery current in the PPC with the reference current.

The differences in the waveforms can be further presented numerically using current ripple values. DAB shows a peak-to-peak current ripple of 4.4%, half-bridge has a ripple of 1.6%, and PPC has a ripple of 2%. Considering the constraints of these converters, the current waveforms show current ripple values well below the goal of 10%. Through the design of the converters, it became evident that it was possible to exceed the goal ripple values with small increases in the filtering components. This realization, coupled with the understanding that improved controllability is achievable with reduced ripple, prompted the decision to pursue a solution with even lower ripple levels.

When looking at the battery voltage waveforms during the operation of the converters, it can be seen from Figures 31, 32 and 33, that there are differences between topologies. The biggest differences are between DAB-based converters and the half-bridge converter.

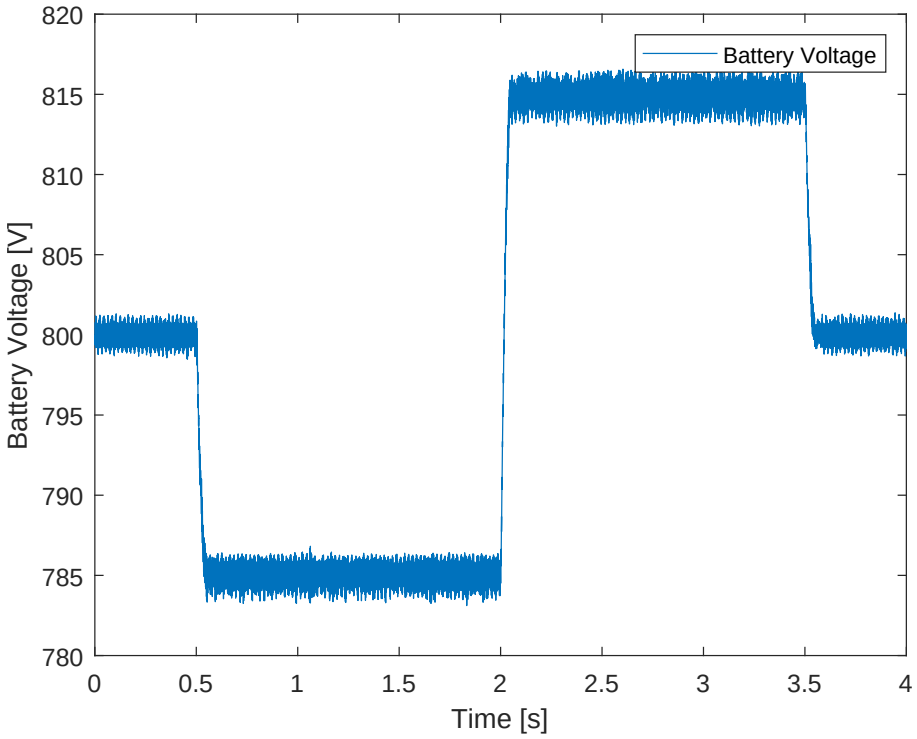

Figure 31. The battery voltage during the operation of the DAB converter.

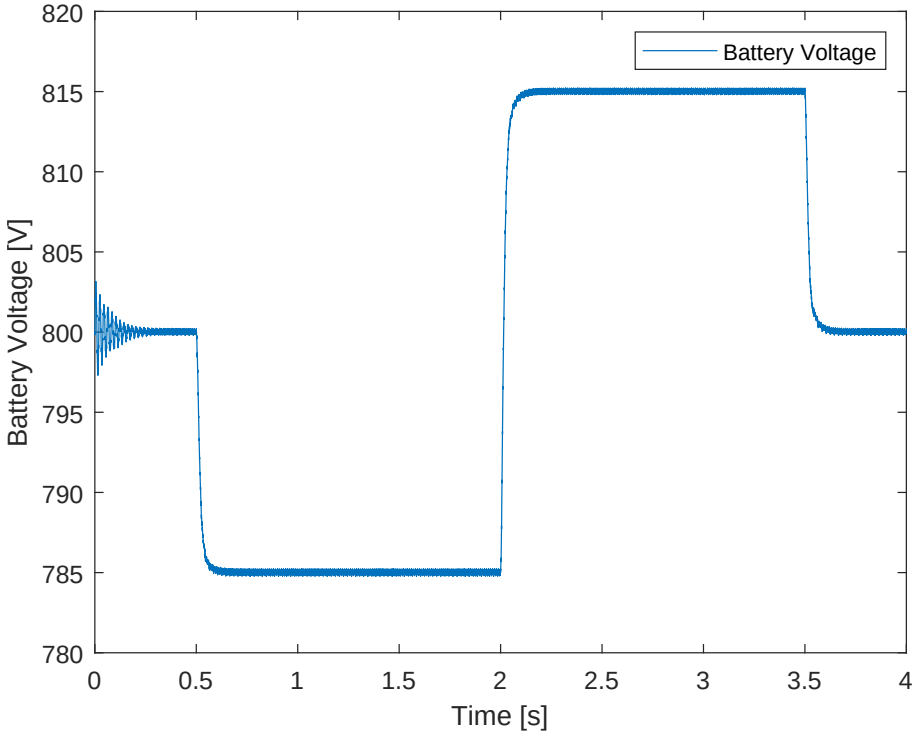

Figure 32. The battery voltage during the operation of the half-bridge converter.

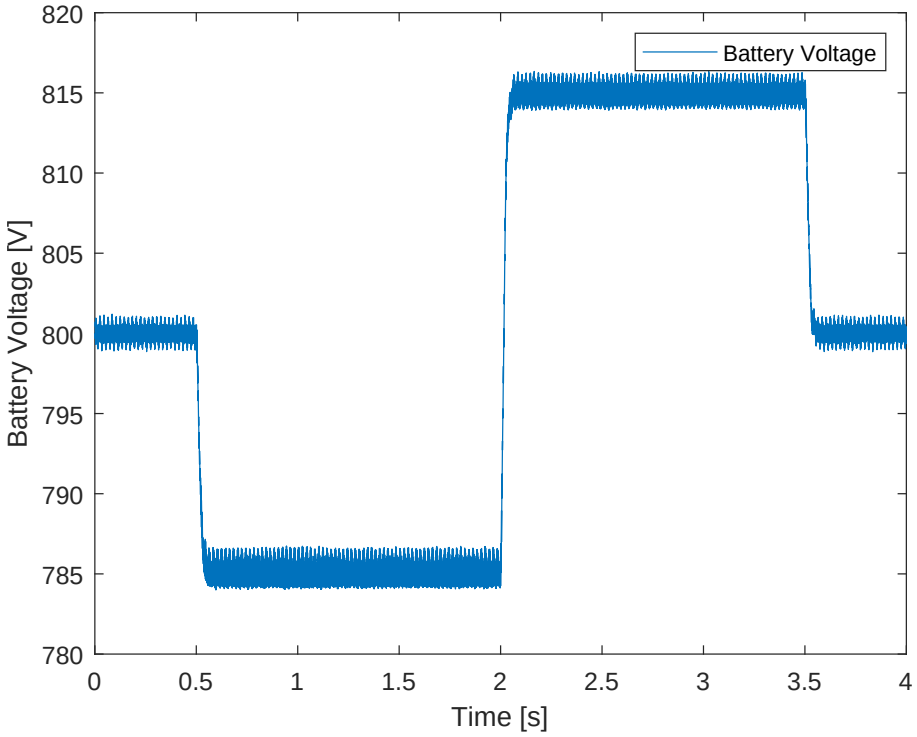

Figure 33. The battery voltage during the operation of PPC.

The differences in the waveforms can be further presented also numerically using voltage ripple values. DAB shows a peak-to-peak voltage ripple of 0.36%, half-bridge has a ripple of 0.06%, and PPC has a ripple of 0.32%. These figures follow the trend of the current ripple figures detailed above. Even though the differences between the converters in this case are small and there was not a constraint for the voltage ripple, these figures further show the differences of stress on the battery and the tendencies of the converters.

When looking at the control variables of the converters, it can be seen from Figures 34, 35 and 36, that there are differences between topologies. The biggest differences are between DAB-based converters and the half-bridge converter. Here, the ripple in the control variable waveforms follows the voltage ripple disturbance on the secondary side of the converter. Thanks to this controlled ripple, it is possible to achieve a stable power flow while blocking this ripple from passing into the battery.

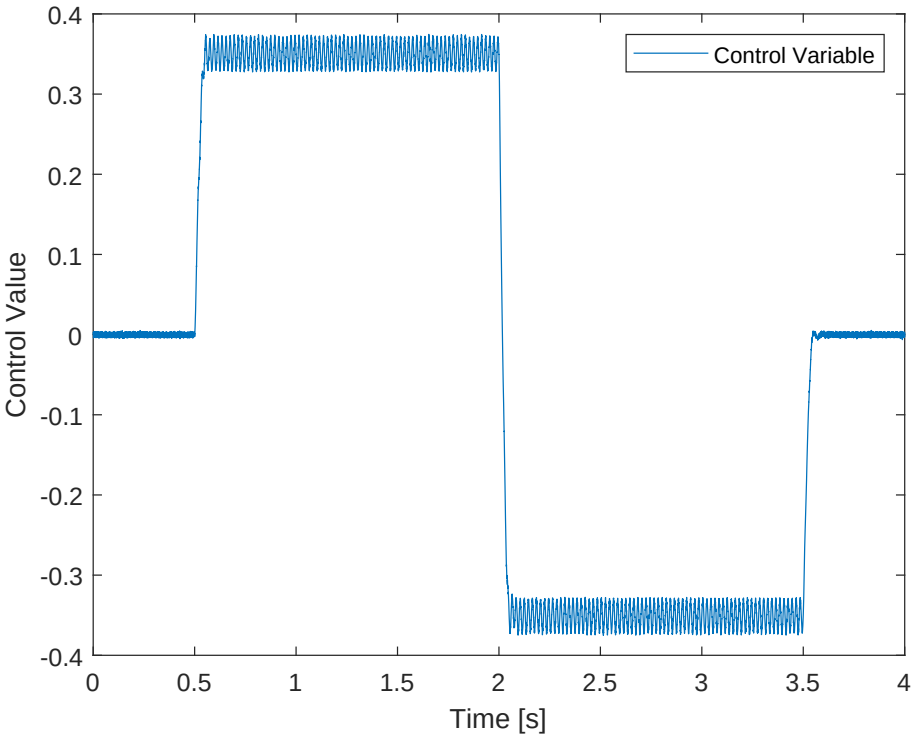

Figure 34. The control variable in the DAB converter during operation.

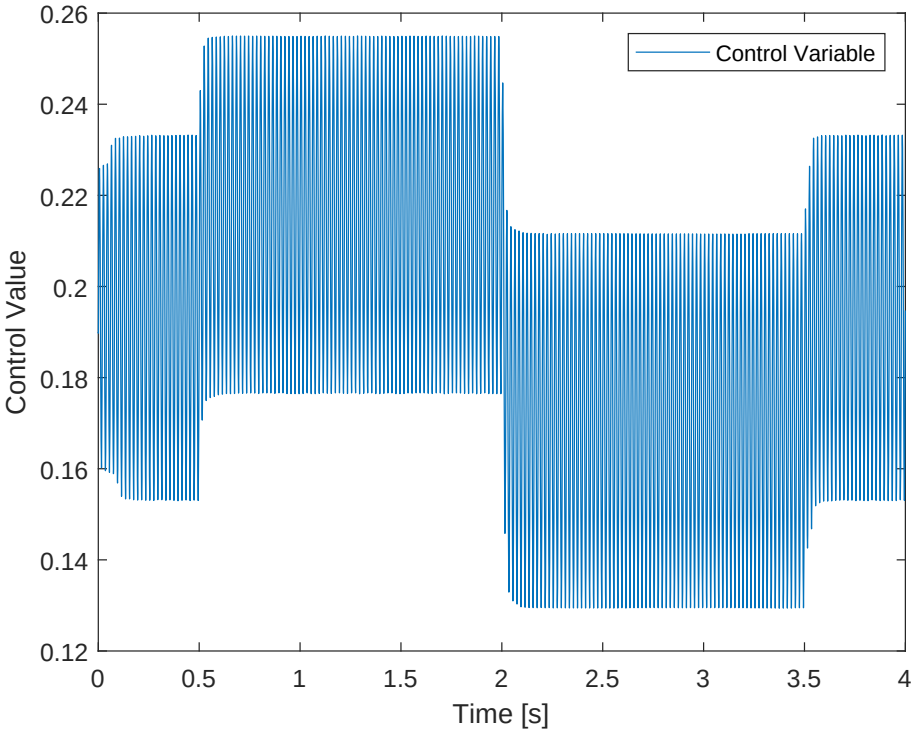

Figure 35. The control variable in the half-bridge converter during operation.

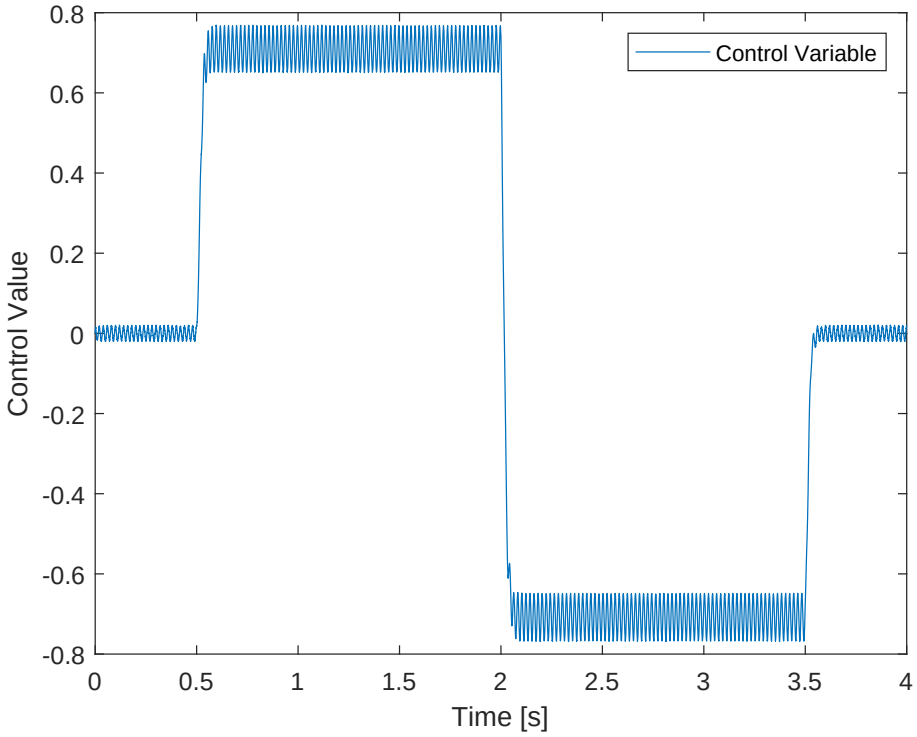

Figure 36. The control variable in the PPC during operation.

4.3 Cooling Considerations

Cooling consideration is an important part of the power converter design. In order to compare converters thoroughly, it is necessary to consider all major aspects of the converter. Cooling capabilities set limits to the admissible power loss in the converter. Additionally, cooling solutions can contribute significantly to the cost and overall volume of the converter.

Therefore, a cooling strategy must be put in place to consider the cooling aspect of the converters. The majority of losses in the power converters at hand occur in the IGBTs. The losses in the remaining system components are low enough to be passively cooled without additional cooling apparatus. The cooling solution of the IGBT modules depends on the power dissipation of the switches, the desired temperature rise in the cooling unit, and the physical dimensions of the IGBT module. To achieve comparable cooling designs, a common temperature rise of 30° C is proposed for the cooling modules. A simple calculation was needed to determine the required thermal resistance of the cooling unit. The thermal resistance required from the cooling modules can be calculated using an equation relating the dissipated power and the temperature rise. Thermal resistance can be calculated using Equation A2.5 [42].

$$R_{\mathrm{TH}} = \frac{\Delta T}{P} \tag{4.1}$$

Here, R_{TH} represents the thermal resistance measured in K/W, ΔT represents the temperature rise in K, and P represents the power dissipation in W. The lost power to be dissipated through the cooling unit is calculated for all IGBT modules. The process of loss calculation is further discussed in Appendix 3.

Both water cooling and active air cooling methods were considered for the cooling of the IGBTs. Using water cooling, it is possible to cool the device within a smaller physical volume where the heat transfer occurs between the IGBT module and a water-cooled metal plate. Water cooling solution also reduces the impact that cooling has on volume differences between the converters. This is because differences in cooling power are achieved primarily with an increased flow of water and its temperature and not necessarily the increase in the cooling plate size.

In active air cooling, heat transfer occurs between the IGBT module and a heatsink with a forced airflow. Forced airflow is typically achieved using a fan. The heat dissipation capability of an active air cooling module depends primarily on the size of the heatsink and the rate of air that passes through it. However, it should be noted that in CERN's application, where the air circulation is limited in the underground caverns, active cooling is not feasible, and water cooling will be used. However, in this case, the heat rejection itself in the form of heatsinks is simply taken further away from the converter, and the economic impact is reflected elsewhere. This, however, can be difficult to estimate numerically without knowing the details about the cooling complex and its components. The active air cooling method, however, allows us to highlight the differences in volumes of the cooling apparatus in a more comprehensive way. This helps to bring greater focus to the impact of cooling considerations. For this reason, an active air cooling strategy was selected.

Active air cooling was solved using cooling modules produced by Fischer Elektronik. This single manufacturer was considered due to their excellent documentation and unified methods of determining the thermal performance of their products. Cooling units were selected individually for each set of IGBTs, and the selection was done iteratively to find the volumetrically smallest possible solution for each IGBT module. The main criteria for selecting the cooling modules were the compatibility of the physical dimensions of the IGBT modules and the cooling modules and the thermal resistance required from the cooling modules. The compatibility of the physical dimensions of IGBT modules and the cooling module means that the IGBT modules can be mechanically mounted onto the

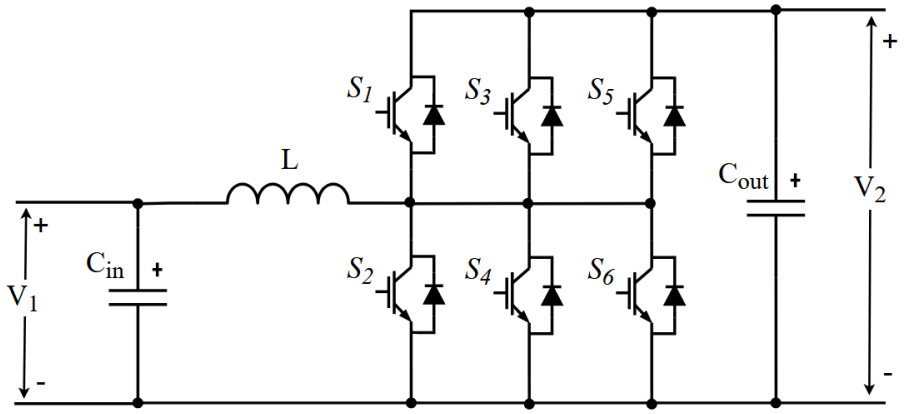

Figure 37. Parallel IGBT configuration for half-bridge converter.

cooling module.

In DAB-based converters, each full bridge of IGBTs was dedicated to a single cooling module. This is because the primary and secondary side bridges have different cooling requirements, so achieving better control over the temperatures is possible. Furthermore, dedicating a single cooling unit for each full bridge allows the use of conventional busbar connections thanks to the improved layout of the switches. From the thermal calculations and mechanical considerations, it became evident that a functioning cooling system can be achieved using the selected cooling modules with no changes to the IGBTs.

The half-bridge converter employs one IGBT module. Therefore, a single cooling module must be used. It is important to remember that a half-bridge converter uses a single half-bridge IGBT module, while DAB-based converters use four. Moreover, there are limitations to how much thermal energy can be directed away from the IGBT as the surface area of heat transfer is limited. The IGBT module's inherent thermal resistance between the semiconductor junction and the external case of the device is another limiting factor. This issue is exacerbated by the converter's disproportionally high switching losses per IGBT module. For these reasons, the required cooling solution for this converter couldn't have been feasible with conventional cooling methods. One option to combat this unrealistic cooling challenge is to increase the overall surface area of thermal conduction by employing additional IGBT modules as detailed in [43]. The switches can be connected in parallel to the existing ones. The switching, however, can take place in a distributed way so that each half-bridge IGBT module turns on sequentially (interleaved multidevice design). The proposed IGBT configuration is illustrated in Figure 37. As can be seen from the figure, the switches are connected in parallel.

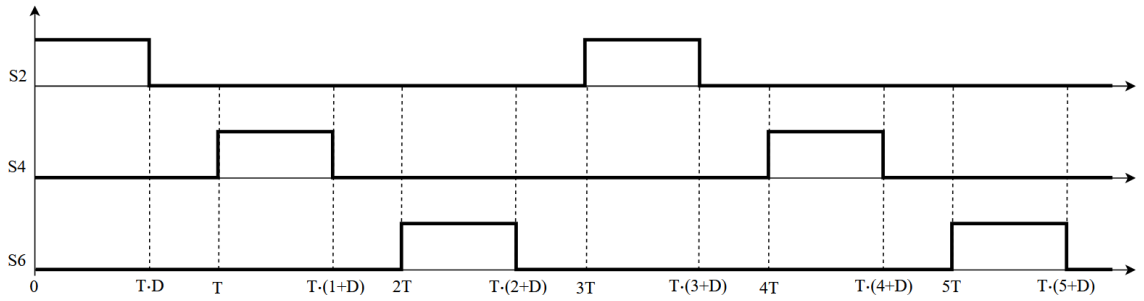

Figure 38. Interleaved switching signals during the operation of the half-bridge converter.

The operation of these switches is interleaved. In other words, each half-bridge is utilized during one switching period. The switching timings are illustrated in Figure 38. During one switching period, only one switch is utilized. The switches take turns during the operation of the converter to distribute the losses between the switches. This kind of configuration does not necessarily increase the efficiency of the converter but rather reduces the losses of a single power module and provides a larger surface area to improve heat dissipation among the switches. This method enables a feasible thermal design for the converter. A feasible thermal design was possible by utilizing three parallel IGBT modules.

In the DAB converter, heatsink LA-V-7-250-24 (R_{Th} = 0.048 K/W) and heatsink LA-V-8-300-24 (R_{Th} = 0.0325 K/W) were used in the primary and secondary side, respectively [44, 45]. For the half-bridge converter, heatsink LA-HLV-3-200 (R_{Th} = 0.02 K/W) was used [46]. Lastly, for the PPC, heatsink LA-28-200-24 (R_{Th} = 0.12 K/W) and heatsink LA-28-250-24 (R_{Th} = 0.095 K/W) were used in the primary and secondary side, respectively [47, 48].

The prices and volumes of the cooling apparatus are further discussed in the next section.

4.4 Comparison Between Converters

This section delves into a quantitative comparative analysis of these converter designs, highlighting their differences. Once the converters were designed to meet common constraints, it became possible to compare the converters. When converters employing different topologies are tailored for the same application, they can be examined side by side, unveiling the distinct advantages, disadvantages, and limitations of each topology. The calculation methods for assessing the losses in the converters are detailed in Appendix 3, and the component selection and magnetics design are specified in this chapter and Appendix 3, respectively. This meticulous comparison is crucial in pinpointing the most suitable converter for integrating ES into MMC applications.

This analysis aims to contribute to the existing knowledge base concerning the three power converter topologies under consideration. By examining the waveforms, efficiency, component volume, cost, and other pertinent parameters, a comprehensive understanding of the strengths and limitations of different converter designs can be acquired.

Through rigorous analysis and evaluation, this comparison seeks to provide an exhaustive assessment of PPC and position the acquired data alongside well-established power converter topologies. Table 4 offers an overview of the numerical distinctions between the converters. This table is divided into four sections: components and properties, losses, volume, and cost. The components and properties section highlights the differences between the essential properties of the converters, their component values, and ratings. The losses section highlights the differences in the origin of losses and their values. The section on volume highlights the differences among volumes of different component categories, specifically identifying the category that contributes the most to the overall volume. The cost category shows differences in the overall cost of the converters.

Table 4. Comparison between PPC, half-bridge, and DAB converters.

Components and properties	**PPC**	**Half-Bridge**	**DAB**
Primary switches	4x 1.2 kV/50 A	6x 1.2 kV/150 A	4x 1.2 kV/150 A
Primary switches MPN	FF50R12RT4	FF150R12RT4	FF150R12RT4
Secondary switches	4x 600 V/200 A	N/A	4x 1.2 kV/150 A
Secondary switches MPN	FF200R06KE3	N/A	FF150R12RT4
C_{in} (uF)	300 (800 V)	500 (800 V)	300 (800 V)
C_{out} (uF)	100 (250 V)	N/A	200 (1050 V)
L_{out} (uH)	N/A	2000 (56 A pk)	10 (45 A pk)
L_{in} (uH)	50 (51 A pk)	50 (51 A pk)	50 (51 A pk)
Transformer Turns Ratio	4:1	N/A	4:5
Galvanic Isolation	No	No	Yes
F_{sw} (kHz)	10	10	10
Power (kW)	40	40	40
Efficiency (%)	98.63	96.30	96.05
Losses	**PPC**	**Half-Bridge**	**DAB**
IGBT conduction losses (W)	176.6	142.4	278.0
IGBT switching losses (W)	361.9	1304.8	1258.3
IGBT total losses (W)	538.6	1444.3	1536.3
Magnetics Core losses (W)	8.9	0	36.3
Magnetics copper losses (W)	1.2	37.3	6.58
Other losses (W)	N/A	N/A	1.6
Total Losses (W)	548.7	1481.6	1579.3
Volume	**PPC**	**Half-Bridge**	**DAB**
Magnetics Volume (L)	1.57	1.74	5.88
Capacitors Volume (L)	0.10	0.32	0.25
Other components Volume (L)	0.56	0.27	0.42
Total Volume (L)	2.23	2.33	6.55
Volume with cooling (L)	4.41	14.26	14.31
Cost	**PPC**	**Half-Bridge**	**DAB**
Total Cost (€)	1112	1329	2030

The differences in component values, their ratings, and their quantities are analyzed first. To compare the power switches between topologies, we can assess the number of switches and their ratings. A half-bridge converter requires the least number of switches, which, however, requires three power modules to be realized in practice. DAB-based converters use two additional switches. However, it should be mentioned that the number of switches in the half-bridge converter at hand is increased when compared to conventional half-bridge converters to achieve realistic cooling for the switches. When comparing DAB to PPC, however, it becomes evident that the ratings of PPC switches are lower compared to the DAB. One can notice that the current ratings of PPC secondary switches are increased compared to the DAB. This is because the PPC secondary side shows peak currents that exceed those of the DAB. It should be noted that the switches selected for these converters are selected while considering the procedure for creating converter prototypes. However, the real-world application currents might deviate from the simulations. This is especially true when considering the complicated nature of simulating the MMC submodule's operation. As one might have noticed, the MMC submodule is simulated simplistically.

When considering the differences between the passive components, the values of the passive components and the ratings can be noticed. It is evident that when comparing PPC with DAB, capacitor ratings and values are reduced in PPC. However, the half-bridge uses one less capacitor in the system, but the existing input capacitor has a higher capacitance value. Here, the real comparable difference becomes the price and volume of these components.

The magnetics can be compared mainly by looking at the volume and costs of these components. The exact design specifications of these components are brought out in Appendix 2. The PPC uses an isolated transformer, which is smaller than the inductor used in the half-bridge. This was achieved because only part of the power is transferred through the transformer. The volumes and costs of magnetics are further discussed below.

As seen from Table 4, DAB provides galvanic isolation, which helps to protect the batteries from faults at the output. Different safety circuits, such as a solid-state breaker, are proposed for PPC to overcome this safety concern [33]. For the half-bridge converter, similar solutions should be considered. However, galvanic isolation does not ensure the safety of the battery from possible faults in the converter itself. Therefore, protection circuits are also required in a DAB converter, and its advantage of galvanic isolation is diminished.

All three power converters were simulated and designed to run at the same switching frequency and power level to achieve comparable results. Looking at the efficiency figures, the PPC offers the highest system efficiency with a figure of 98.63%, while the half-bridge

and DAB converter offer comparable efficiencies of around 96%. The differences in efficiencies become more prominent when looking at the losses and the required cooling capabilities.

The losses can be divided between IGBT losses, losses in the magnetics, and other losses. Here, other losses originate from a converter-specific filtering inductor. The IGBTs' losses contribute to most of the converters' losses. IGBT losses are the lowest in PPC with 538.6 W and highest in DAB with 1536.3 W. Although these two converters have the same number of switches, the PPC switches pass less current and at a lower voltage. Even though the half-bridge converter is the simplest topology with the lowest number of switches, it experiences comparable losses in the switches with DAB. This is due to the fact that the switches are operating at full voltage and full current of the converter.

Losses in the magnetics also differ in the converters. The lowest magnetic core loss is in a half-bridge converter, with a negligible amount of power being lost in the core, and the highest core loss occurs in the DAB converter, where 36.3 W is lost in the core. PPC core loss is at 8.9 W. Half-bridge magnetics shows the lowest core loss due to the use of powdered iron core material with low reluctance and the fact that it is a DC inductor with little changes in the magnetic flux density. Copper losses, however, are the lowest in PPC with losses at 1.2 W and highest in half-bridge with losses at 37.3 W. DAB copper losses are at 6.58 W. Lower copper losses in the PPC are mainly due to the reduced currents in the transformer compared to DAB, different winding configuration and a smaller transformer design with a shorter MLT. On the other hand, DC inductor of the half-bridge converter has more turns in the core, which decreases the options for reducing the winding resistance. From these figures, the advantage of processing only part of the power becomes clear as it results in lower currents and smaller magnetic components. Additionally, the output filtering inductor of the DAB converter adds 1.6 W of losses to its total losses. A comprehensive overview of the loss calculation methodology for calculating losses in the converters is brought out in Appendix 3. Overall, PPC operates with a power loss of 548.7 W, while half-bridge operates with a power loss of 1481.6 W, and DAB operates with a power loss of 1579.3 W. The differences in the losses are almost threefold. This means the cooling capabilities must also be upscaled to account for this difference.

When looking at the volumes of different categories of components, it becomes evident that magnetics occupies the majority of the volume. Here, the DAB transformer is the largest, with a volume of 5.88 L. The PPC transformer and half-bridge inductor are considerably smaller, with volumes of 1.57 L and 1.74 L, respectively. PPC has the smallest magnetics volume. The inductor in the half-bridge has a simpler construction compared to the PPC transformer, which helps to reduce the price of the component. DAB transformer

is the largest of them all and has the highest price. When looking at the volume of the capacitors, the PPC leads with the smallest volume of 0.1 L, followed by DAB with 0.25 L. Half-bridge's capacitors occupy a volume of 0.32 L. Other components include the IGBT modules and the output filtering inductor of the DAB converter. PPC has the smallest overall volume of 2.23 L when the cooling is not considered. The half-bridge converter's volume is in a similar range, i.e., 2.33 L, and the DAB converter is almost three larger, yielding a volume of 6.55 L. These volumes account for the sum of all components. The required volume for wiring, connectors, protection, control, and mechanical layout are not considered. However, taking into account that the protection requirements, ratings for the wiring, and control requirements in the converters are comparable, the additional volume differences between converters are considered to be marginal.

When considering the cooling apparatus together with the total component volume, the differences between the converter volumes increase significantly. For PPC, the overall volume together with cooling is 4.41 L, but for half-bridge and DAB converters, the overall volumes rise to 14.26 L and 14.31 L, respectively. As can be seen from these figures, the volume advantages of the half-bridge converter are essentially lost to the cooling of the three power modules used in the design. Using water cooling, however, the converter volume differences can be smaller. In this scenario, it's important to highlight that relocating the physical cooling system farther from the converter does not diminish the associated costs and space requirements on a system level. These expenses and spatial demands remain higher for converters that require greater cooling, in contrast to those with lower cooling requirements. Considering this and the figures discussed above, the advantage of PPC becomes evident as less power is lost and less cooling is needed. This advantage can also be seen when looking at the cost of the components.

The cost comparison of the converters considers the cost of magnetics, capacitors, filtering inductors, switches, and cooling heatsinks. The costs of different components and how they contribute to the overall cost of the converters can be seen in Table 5.

As can be seen from the table, PPC has the lowest cost of 1112 €. The second in cost is half-bridge with a price of 1329 €. The most expensive of the converters is DAB with a price of 2030 €. Both PPC and half-bridge converters are close in their prices. Interestingly, the distribution of costs is not the same for all converters. What differentiates the DAB converter from the others costwise is its more expensive transformer.

Cooling is a significant contributor to the cost of these converters. For PPC and half-bridge converters, the cost of cooling forms the most significant portion of the converter cost. This is followed by magnetics and IGBTs, respectively. In the DAB converter, the largest

Table 5. Price comparison between PPC, half-bridge, and DAB converter components.

Cost item	**PPC**	**Half-Bridge**	**DAB**
Magnetics (€)	298	320	1079
Capacitors (€)	18.5	32	32.9
IGBTs (€)	180	210	280
Filtering inductors (€)	N/A	N/A	14
Cooling (€)	615	767	624
Total (€)	1112	1329	2030

contributor to the costs is the magnetics, followed by cooling and IGBTs, respectively. The cost of magnetics forms a more significant portion of the DAB converter cost due to the utilization of much more ferrite material and more litz wires for the windings. Additionally, the custom mechanical elements that are required for the realization of this transformer further increase its cost.

One can notice from the table that the prices of auxiliary electronics, together with the control boards, are not considered. The prices for auxiliary electronics between the three converters are expected to differ between converters considering the differences in needs for current sensors and IGBT driver circuits. However, associated costs and cost deviations between converters are considered to be insignificant enough not to change the overall distribution of the costs.

When considering the current and voltage waveforms presented in Subsection 4.2 as a point of comparison, a few observations emerge that shed light on the nuances between the converters. In terms of voltage ripple that is applied on the battery, the DAB converter shows a peak-to-peak voltage ripple of 0.36%, while the half-bridge has a significantly lower ripple at 0.06%, and the PPC is in between with a ripple of 0.32%. It can be noticed that DAB-based converters (full and partial power) feature significantly higher voltage ripple compared to half-bridge converters. Although the variances between the converters in this context are not significant, and there was no design constraint in regard to the voltage ripple, these metrics accentuate the different stresses on the battery and underscore the inherent tendencies of each converter. In terms of battery current ripple values, however, similar tendencies can be noticed. DAB converter exhibits the highest peak-to-peak current ripple of 4.4%, half-bridge has a more controlled ripple at 1.6%, and PPC presents a ripple of 2%. Battery current ripple was one of the design constraints with a maximum threshold of 10%. Through the design of the converters, it became clear that achieving ripple values even lower than the set goal was possible with only minor increases in the values of

filtering components. As the increase in the filtering component values eventually resulted in diminishing returns, the figures presented above were achieved. These figures reveal that DAB-based converters tend to produce higher current ripple values than half-bridge converters. However, the PPC exhibits lower current ripple values than the full-power DAB converter. Additionally, it should be noted that the control aspects should also be taken into consideration, as it could potentially improve the ripple performance of the converters.

From the comparisons conducted above, the advantages of PPC become evident in three important key categories: efficiency, volume, and cost. The PPC outperformed the conventional full power converters, with a 2.42% higher efficiency, 69.07% smaller volume, and 16.33% lower cost. The closest topology in terms of these categories was the half-bridge converter. Even though it has a simpler design, utilizes fewer switches, and a more simple magnetic component, it experiences more losses, necessitating a larger and costlier cooling solution. In contrast, the DAB converter underperforms across all three metrics but provides increased safety due to the galvanic isolation. These observations underscore the benefits of employing a converter that processes only a fraction of the power. Moreover, its advantages become even more pronounced when deploying PPC in a scaled setting.

Concluding the comparative analysis of the converters, the following chapter underscores the main results of this thesis and outlines avenues for future research.

5. Conclusion

5.1 Summary and Main Results

In this work, an overview of the technical considerations for the need for ES is given for the FCC, and different options for ES integration are presented. An introduction to the challenges of ES integration shows that some options offer more benefits for the project. Within the analysis conducted in this thesis, the application of MVDC networks and the use of MMCs for the connection between the AC grid and the internal MVDC grid were pursued. The utilization of MVDC networks for distributing energy within the FCC has multiple advantages over an AC network such as reduced excavated material, reduced copper usage, and improved system efficiency.

Furthermore, the goals of cost reduction and the specific considerations for connecting ESs into the FCC are limiting the available technical solutions for connecting ES into the FCC thereby necessitating technological innovations within the design. This is particularly true in integrating ES into the MMC submodules.

The primary objective of this thesis is to demonstrate the technical considerations of utilizing PPCs in ES applications in the FCC, with a specific focus on battery integration into MMC submodules. Moreover, the utilization of PPCs in this application had not been demonstrated before. To provide a comprehensive analysis, two other commonly used conventional bidirectional DC-DC power converter topologies were proposed for comparison purposes, highlighting the advantages of the PPC over them. Additionally, this thesis addresses the challenges associated with control in PPCs. In order to enhance the controllability and efficiency of the converter, specific control methods were employed to regulate the DC bias current and compensate for AC ripple voltage. The results demonstrated that implementing these designated control techniques yielded improvements in both controllability and volume.

To compare the three topologies, a specific use case with a predetermined power level was proposed. For this, simulations of all of the power converters were created to showcase their operation. In order to achieve accurate and fair comparison results, all of the power converters were designed together with component selection, magnetics design and cooling considerations. By analyzing the simulation results and considering the physical parameters of the components, it was possible to calculate the losses in the converters and highlight

the differences in efficiencies. Additionally, using the selected and custom-designed components, it was possible to compare the costs and volumes of the converters.

The comparisons clearly demonstrate that the overall volume of the converter is significantly influenced by the use of actively cooled commercially available radiators. The PPC emerges as the most compact solution with a very close volume to the half-bridge converter. However, when paired with a cooling apparatus, the PPC's volume was approximately three times smaller than that of the half-bridge converter. The volume of the DAB converter was above both of them. The comparisons also demonstrated the differences in efficiencies. The highest efficiency figures were achieved with PPC at 98.63%. The efficiencies of half-bridge and DAB converters were lower with their respective efficiency figures being at 96.30% and 96.05%. Additionally, the differences in the cost of the converters were also considerable. The PPC had the lowest cost at 1112 € while the costs of half-bridge and DAB converters were at 1329 € and 2030 €. To conclude these results, PPC outperformed the conventional full power converters, with a 2.42% higher efficiency, 69.07% smaller volume, and 16.33% lower cost while providing comparable performance. Considering these metrics, it becomes clear that the PPC provides significant advantages over conventional power converters.

5.2 Future Work

In this study, a PPC in an IPOS configuration based on the DAB converter was proposed. However, there are opportunities for further improvements in various aspects of this topology. For instance, the partiality in the proposed setup was set at 20%. As one of the advantages of a PPC is that only a fraction of the power is processed, it enables achieving higher efficiencies and power densities without compromising performance. By reducing the voltage difference between the primary and secondary sides, the partiality can be further reduced. A lower partiality allows to process a reduced amount of power which helps to reach even higher efficiencies. In future studies, following the findings of this research, the overall voltage of the battery pack could be increased, resulting in a reduced voltage difference without necessitating changes to the secondary side voltage or MMC design. This assumes that the submodule voltage is optimally selected for the application. Additionally, as the PPC is not yet a mature converter topology, there is still room for optimizations to improve the converter performance such as exploring alternative PPC topologies and control strategies.

Taking everything into consideration, the PPC presents an attractive solution for integrating ES into electrical systems, providing benefits such as reduced losses and smaller volume requirements at a lower cost. The goal of this thesis has been achieved and its results

have been detailed. The work presented here empowers researchers and engineers with the knowledge necessary to consider this technology for efficient and effective power conversion solutions. This has broader implications for the industry beyond CERN, as it seeks more cost-effective and energy-efficient technologies to address the challenges in ES integration solutions.

References

[1] CERN. *LHC The Guide*. [Accessed: 24-05-2023]. URL: https://cds.cern.ch/record/2809109/files/CERN-Brochure-2021-004-Eng.pdf.

[2] CERN. *The Large Hadron Collider*. [Accessed: 20-05-2023]. URL: https://home.cern/science/accelerators/large-hadron-collider.

[3] CERN. *CERN accelerator complex*. [Accessed: 22-05-2023]. URL: https://home.cern/science/accelerators/accelerator-complex.

[4] CERN. *FCC Overview*. [Accessed: 20-05-2023]. URL: https://fcc.web.cern.ch/overview.

[5] FCC collaboration et al. "FCC-hh: the Hadron collider: future circular collider conceptual design report volume 3". In: *European Physical Journal: Special Topics* 228.4 (2019), pp. 778, 875–878, 786–789, 994–995.

[6] CERN. *FCC magnet design*. [Accessed: 24-05-2023]. URL: https://fcc.web.cern.ch/magnet-design.

[7] CERN. *FCC power converters R&D*. [Accessed: 22-05-2023]. URL: https://indico.cern.ch/event/1064327/contributions/4883197/attachments/2453385/4208496/FCCWeek_2022_EPC.pdf.

[8] Hamdi Abdi et al. *Energy Storage Systems*. Dec. 2017, pp. 333–368. ISBN: 9780128042083. DOI: 10.1016/B978-0-12-804208-3.00007-8.

[9] Naser Hassanpour et al. "Partial power processing and its emerging applications". In: Dec. 2022, pp. 211–242. ISBN: 9781839534683. DOI: 10.1049/PBPO207F_ch7.

[10] EUROBAT. *EUROBAT Innovation Roadmap Annex*. [Accessed: 22-05-2023]. URL: https://www.eurobat.org/wp-content/uploads/2022/08/EUROBAT-WP-Innovation-Roadmap-2030_update-V2_Technical_annex.pdf.

[11] Juergen K. Steinke et al. "MVDC Applications and Technology". In: (2019), pp. 1–8.

[12] Sophie Coffey et al. "Review of MVDC Applications, Technologies, and Future Prospects". In: *Energies* 14.24 (2021). ISSN: 1996-1073. DOI: 10.3390/en14248294. URL: https://www.mdpi.com/1996-1073/14/24/8294.

[13] Suman Debnath et al. "Operation, Control, and Applications of the Modular Multilevel Converter: A Review". In: *IEEE Transactions on Power Electronics* 30.1 (2015), pp. 37–53. DOI: 10.1109/TPEL.2014.2309937.

[14] Zheng Gong et al. “Modulated Model Predictive Control for MMC-Based Active Front-End Rectifiers Under Unbalanced Grid Conditions”. In: *IEEE Transactions on Industrial Electronics* 66.3 (2019), pp. 2398–2409. DOI: 10.1109/TIE.2018.2844836.

[15] Salman Ali et al. “Recent Advancements in Submodule Topologies and Applications of MMC”. In: *IEEE Journal of Emerging and Selected Topics in Power Electronics* 9.3 (2021), pp. 3407–3435. DOI: 10.1109/JESTPE.2020.2990689.

[16] Devendra Patil and Vivek Agarwal. “Compact Onboard Single-Phase EV Battery Charger With Novel Low-Frequency Ripple Compensator and Optimum Filter Design”. In: *IEEE Transactions on Vehicular Technology* 65.4 (2016), pp. 1948–1956. DOI: 10.1109/TVT.2015.2424927.

[17] Ishaan Puranik, Lei Zhang, and Jiangchao Qin. “Impact of Low-Frequency Ripple on Lifetime of Battery in MMC-based Battery Storage Systems”. In: (2018), pp. 2748–2752. DOI: 10.1109/ECCE.2018.8558061.

[18] Electricity - Magnetism. *Half Bridge Converter*. [Accessed: 29-09-2023]. URL: https://www.electricity-magnetism.org/half-bridge-converter/.

[19] B. Vural, Serkan Dusmez, and Mehmet Uzunoglu. “An improved power conditioning unit for energy storage systems in hybrid electrical vehicles”. In: (June 2010). DOI: 10.13140/2.1.4664.3202.

[20] Michail Vasiladiotis and Alfred Rufer. “Analysis and Control of Modular Multilevel Converters With Integrated Battery Energy Storage”. In: *IEEE Transactions on Power Electronics* 30.1 (2015), pp. 163–175. DOI: 10.1109/TPEL.2014.2303297.

[21] Shaopo Qiu and Bin Shi. “An Enhanced Battery Interface of MMC-BESS”. In: (2019), pp. 434–439. DOI: 10.1109/PEDG.2019.8807554.

[22] Alberto Rodríguez Rodríguez Alonso et al. “An overall study of a Dual Active Bridge for bidirectional DC/DC conversion”. In: (2010), pp. 1129–1135. DOI: 10.1109/ECCE.2010.5617847.

[23] Haris Ataullah et al. “Analysis of the Dual Active Bridge-Based DC-DC Converter Topologies, High-Frequency Transformer, and Control Techniques”. In: *Energies* 15.23 (2022). ISSN: 1996-1073. DOI: 10.3390/en15238944. URL: https://www.mdpi.com/1996-1073/15/23/8944.

[24] Naser Hassanpour et al. “A Series Partial Power Converter Based on Dual Active Bridge Converter for Residential Battery Energy Storage System”. In: (2021), pp. 1–6. DOI: 10.1109/RTUCON53541.2021.9711725.

[25] Hasan Bayat and Amirnaser Yazdani. “A Hybrid MMC-Based Photovoltaic and Battery Energy Storage System”. In: *IEEE Power and Energy Technology Systems Journal* 6.1 (2019), pp. 32–40. DOI: 10.1109/JPETS.2019.2892418.

[26] Gabriel Fernandez. *Dual Active Bridge converter modulation techniques*. [Accessed: 23-05-2023]. URL: https://imperix.com/doc/implementation/dual-active-bridge-control.

[27] R. Barlik, M. Nowak, and P. Grzejszczak. “Power transfer analysis in a single phase dual active bridge”. In: *Bulletin of the Polish Academy of Sciences. Technical Sciences* 61.4 (2013), pp. 809–828. ISSN: 0239-7528.

[28] Jon Anzola et al. “Review of Architectures Based on Partial Power Processing for DC-DC Applications”. In: *IEEE Access* 8 (2020), pp. 103405–103418. DOI: 10.1109/ACCESS.2020.2999062.

[29] Andrii Chub, Levy Costa, and Marco Liserre. “Analysis and design of asymmetric quad-active-bridge converter”. In: (2017), pp. 5367–5372. DOI: 10.1109/IECON.2017.8216930.

[30] Qinglei Bu et al. “A Comparative Review of High-Frequency Transient DC Bias Current Mitigation Strategies in Dual-Active-Bridge DC–DC Converters Under Phase-Shift Modulations”. In: *IEEE Transactions on Industry Applications* 58.2 (2022), pp. 2166–2182. DOI: 10.1109/TIA.2021.3136498.

[31] Kazuto Takagi and Hideaki Fujita. “Dynamic Control and Performance of a Dual-Active-Bridge DC–DC Converter”. In: *IEEE Transactions on Power Electronics* 33.9 (2018), pp. 7858–7866. DOI: 10.1109/TPEL.2017.2773267.

[32] Bernardo Cougo and Johann W. Kolar. “Integration of Leakage Inductance in Tape Wound Core Transformers for Dual Active Bridge Converters”. In: (2012), pp. 1–6.

[33] Pavel Purgat et al. “Low-Voltage dc System Building Blocks: Integrated Power Flow Control and Short Circuit Protection”. In: *IEEE Industrial Electronics Magazine* 17.1 (2023), pp. 6–20. DOI: 10.1109/MIE.2021.3106275.

[34] Mohd Alam, Kuldeep Kumar, and Viresh Dutta. “Comparative efficiency analysis for silicon, silicon carbide MOSFETs and IGBT device for DC–DC boost converter”. In: *SN Applied Sciences* 1 (2019), pp. 1–11.

[35] Bufan Shi et al. “A review of silicon carbide MOSFETs in electrified vehicles: Application, challenges, and future development”. In: *IET Power Electronics* 16 (May 2023). DOI: 10.1049/pel2.12524.

[36] B Jayant Baliga. *The IGBT device: physics, design and applications of the insulated gate bipolar transistor*. William Andrew, 2015.

[37] He Niu. “A review of power cycle driven fatigue, aging, and failure modes for semiconductor power modules”. In: (2017), pp. 1–8. DOI: 10.1109/IEMDC.2017.8002341.

[38] K Kahle. *Power Converters and Power Quality*. en. 2015. DOI: 10.5170/CERN-2015-003.57. URL: http://cds.cern.ch/record/2038611.

[39] Thomas Meade et al. “Parasitic inductance effect on switching losses for a high frequency Dc-Dc converter”. In: (Mar. 2008), pp. 3–9. DOI: 10.1109/APEC.2008.4522692.

[40] Texas Instruments. *Understanding and Optimizing Electromagnetic Compatibility in Switchmode Power Supplies*. [Accessed: 30-09-2023]. URL: https://www.ti.com/seclit/ml/slup202/slup202.pdf.

[41] Xuewei Pan et al. “An Overview and Comprehensive Comparative Evaluation of Current-Fed-Isolated-Bidirectional DC/DC Converter”. In: *IEEE Transactions on Power Electronics* 35.3 (2020), pp. 2737–2763. DOI: 10.1109/TPEL.2019.2931739.

[42] Texas Instruments. *Section 4 - Power Transformer Design*. [Accessed: 20-08-2023]. URL: https://www.ti.com/lit/ml/slup126/slup126.pdf.

[43] Omar Hegazy, Joeri Van Mierlo, and Philippe Lataire. “Analysis, Modeling, and Implementation of a Multidevice Interleaved DC/DC Converter for Fuel Cell Hybrid Electric Vehicles”. In: *IEEE Transactions on Power Electronics* 27.11 (2012), pp. 4445–4458. DOI: 10.1109/TPEL.2012.2183148.

[44] Fischer Elektronik. *Data sheet Product LA V 7 ...* [Accessed: 30-09-2023]. URL: https://www.fischerelektronik.de/web_fischer/en_GB/VA/LAV725024/datasheet.xhtml?branch=heatsinks.

[45] Fischer Elektronik. *Data sheet Product LA V 8 300 24*. [Accessed: 30-09-2023]. URL: https://www.fischerelektronik.de/web_fischer/en_GB/VA/LAV830024/datasheet.xhtml?branch=heatsinks.

[46] Fischer Elektronik. *Data sheet Product LA HLV 3 200*. [Accessed: 30-09-2023]. URL: https://www.fischerelektronik.de/web_fischer/en_GB/VA/LAHLV3200/datasheet.xhtml?branch=heatsinks.

[47] Fischer Elektronik. *Data sheet Product LA 28 200 24*. [Accessed: 30-09-2023]. URL: https://www.fischerelektronik.de/web_fischer/en_GB/VA/LA2820024/datasheet.xhtml?branch=heatsinks.

[48] Fischer Elektronik. *Data sheet Product LA 28 250 24*. [Accessed: 30-09-2023]. URL: https://www.fischerelektronik.de/web_fischer/en_GB/VA/LA2825024/datasheet.xhtml?branch=heatsinks.

[49] Xuewei Pan et al. “An overview and comprehensive comparative evaluation of current-fed-isolated-bidirectional DC/DC converter”. In: *IEEE Transactions on Power Electronics* 35.3 (2019), pp. 565–586.

[50] MagINC. *mag-inc product catalog*. [Accessed: 20-08-2023]. URL: https://www.mag-inc.com/Media/Magnetics/File-Library/Product%20Literature/Ferrite%20Literature/Magnetics-2021-Ferrite-Catalog.pdf.

[51] Ferroxcube. *Ferroxcube Datasheet 3C90*. [Accessed: 20-08-2023]. URL: https://www.ferroxcube.com/upload/media/product/file/MDS/3c90.pdf.

[52] Ferroxcube. *Ferroxcube Datasheet E100$_6$0$_2$8*. [Accessed: 20-08-2023]. URL: https://www.ferroxcube.com/upload/media/product/file/Pr_ds/E100_60_28.pdf.

[53] Xuewei Pan et al. “An overview and comprehensive comparative evaluation of current-fed-isolated-bidirectional DC/DC converter”. In: *IEEE Transactions on Power Electronics* 35.3 (2019), pp. 539–564.

[54] Infineon. *FF200R06KE3-Datasheet*. [Accessed: 08-09-2023]. URL: https://www.infineon.com/dgdl/Infineon-FF200R06KE3-DataSheet-v03_00-EN.pdf?fileId=db3a304412b407950112b434a07960d4.

Appendix 1 – Non-Exclusive License for Reproduction and Publication of a Graduation Thesis[1]

I Joosep Niinemägi

1. Grant Tallinn University of Technology free licence (non-exclusive licence) for my thesis "Application of Partial Power Converters for the Powering of Future Circular Collider", supervised by Andrii Chub and Manuel Colmenero Moratalla
   1.1. to be reproduced for the purposes of preservation and electronic publication of the graduation thesis, incl. to be entered in the digital collection of the library of Tallinn University of Technology until expiry of the term of copyright;
   1.2. to be published via the web of Tallinn University of Technology, incl. to be entered in the digital collection of the library of Tallinn University of Technology until expiry of the term of copyright.
2. I am aware that the author also retains the rights specified in clause 1 of the non-exclusive licence.
3. I confirm that granting the non-exclusive licence does not infringe other persons' intellectual property rights, the rights arising from the Personal Data Protection Act or rights arising from other legislation.

30.12.2023

[1]The non-exclusive licence is not valid during the validity of access restriction indicated in the student's application for restriction on access to the graduation thesis that has been signed by the school's dean, except in case of the university's right to reproduce the thesis for preservation purposes only. If a graduation thesis is based on the joint creative activity of two or more persons and the co-author(s) has/have not granted, by the set deadline, the student defending his/her graduation thesis consent to reproduce and publish the graduation thesis in compliance with clauses 1.1 and 1.2 of the non-exclusive licence, the non-exclusive license shall not be valid for the period.

Appendix 2 - Magnetics Calculations

The transformer design started with a first-pass design. The first-pass design intends to assess the requirements for the transformer's components before the design can be refined.

In the first-pass design, the first step is to evaluate the required geometry of the core. For this, an equation that represents the geometrical coefficient of the transformer is used. The geometrical coefficient can be estimated using Equation A2.1 [49].

$$K_{\text{gfe}} \geq \frac{\rho \lambda_1^2 I_{\text{tot}}^2 K_{\text{fe}}^{(2/\beta)}}{4 K_u (P_{\text{tot}})^{((\beta+2)/\beta)}} \cdot 10^8 \tag{A2.1}$$

To reach realistic designs, the core's geometrical coefficient (K_{gfe}) must be greater or equal to the total on the right side of the equation. Here, ρ represents copper's resistivity, λ_1 represents the volts-seconds applied on the primary side of the transformer, I_{tot} represents the sum of the primary side and secondary side RMS currents referencing them both to the primary side, K_{fe} represents the core loss coefficient, K_u represents the winding fill factor, P_{tot} represents the total allowed power dissipation and β represents the core loss exponent and the K_{fe} represents the core loss coefficient. The equation is multiplied with 10^8 to compensate for the cm units used for dimensions throughout the design process. The transformer's geometrical coefficient helps to estimate the required mechanical size of the core and its required thermal energy dissipation limitations, considering the applied voltages and the switching frequency.

In order to match the required geometrical coefficient of the transformer with the core, the core's geometrical coefficient can be calculated with the help of its mechanical dimensions. The core's geometrical coefficient can be calculated with Equation A2.2 [49].

$$K_{\text{gfe}} = \frac{W_A A_{\text{c}}^{2(1-1/\beta)}}{MLT l_{\text{e}}^{(2/\beta)}} u(\beta) \tag{A2.2}$$

Here, W_A represents the window area of the core, A_c represents the cross-sectional area of the core, MLT stands for the median length per turn for the core and l_e represents the effective length length of the magnetic flux in the core. The value u(β) is defined through Equation A2.3 [49].

$$u(\beta) = \left[\left(\frac{\beta}{2}\right)^{-\left(\frac{\beta}{\beta+2}\right)} + \left(\frac{\beta}{2}\right)^{\left(\frac{2}{\beta+2}\right)} \right]^{-\left(\frac{\beta+2}{\beta}\right)} \tag{A2.3}$$

In the previous equations, there are also multiple variables that need to be defined through equations, and some of them need visual representations, as shown below.

One input parameter for designing a transformer is the maximum allowed power dissipation (P_{tot}), in Watts. It can be defined by defining the maximum allowed temperature rise and using the core's thermal resistance value. P_{tot} can be calculated with Equation A2.4 [42].

$$P_{\text{tot}} = \frac{T_{\text{rise}}}{R_{\text{th}}} \tag{A2.4}$$

For the E-shaped cores considered in this work, the core's thermal resistance R_{th} can be estimated using Equation A2.5 [42].

$$R_{\text{th}} = \frac{36}{A_{\text{W}}} \tag{A2.5}$$

This formula takes into account that the usable surface area of the core is approximately 22 times the winding window area W_A. The latter equation is derived from Equation A2.6 [42].

$$R_{\text{th}} = \frac{800°C/W}{A_{\text{S}}} \tag{A2.6}$$

Here, A_S represents the available surface area of the core. Equation 4 represents is used to calculate the thermal resistance for one core. Where a stacked core configuration was used, the increased surface area was also taken into account. The units for thermal resistance in this application are °C/W.

Window area W_A is the are inside the closed core in which the windings reside. How the core's dimensions are shown in product catalogs is illustrated in Figure 39.

Here, the window can be calculated using the dimensions M and D by multiplying the total width of the window with the total length of the window as depicted in Equation A2.7.

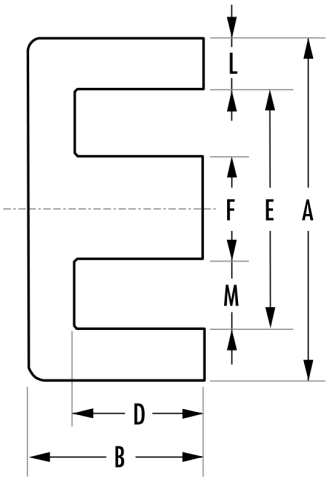

Figure 39. Dimensions as they are given in a product catalog. [50]

$$W_A = 2L \cdot W \tag{A2.7}$$

Here, L represents the length of the window (represented in the figure above as D), and W represents the width of the window (represented in the figure above as M). In this work, cm^2 units are used for the window area.

Copper's resistivity (ρ) is defined as $1.72 \cdot 10^6$ ohm-cm.

Volt-seconds applied to the primary winding (λ_1) can be calculated using Equation A2.8 [49]. The units for this quantity are V-sec.

$$\lambda_1 = V_1 \cdot D \cdot T_{\text{on}} \tag{A2.8}$$

Here, V_1 represents the primary side voltage, D represents the duty cycle and T_{on} represents the on-time of the switch. In the case of DAB-based converters, the duty cycle is always 0.5. This means that T_{on} can be reached by taking a reciprocal of the switching frequency and multiplying that with the duty cycle.

Core loss exponent β is a value that is core material specific and can be typically found in the core material's datasheet [51]. It is a unitless value used for curve fitting of empirical power loss density.

Core loss coefficient K_{fe} is a value that is also core material specific and is typically

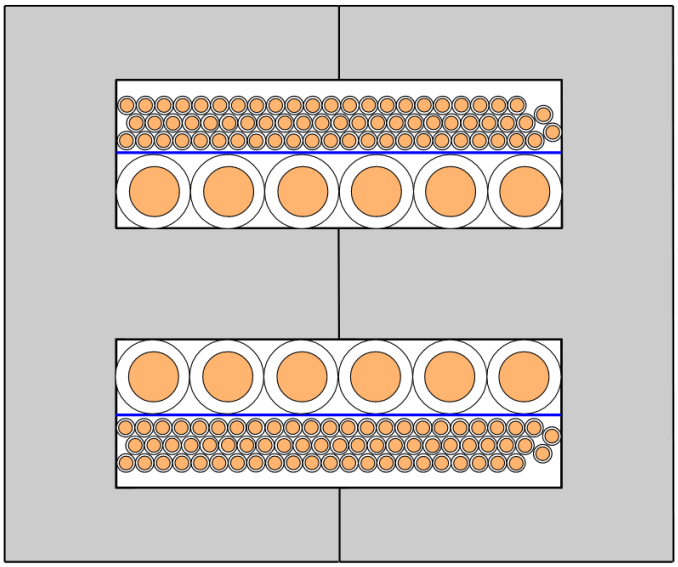

Figure 40. Illustration of the window area utilization.

provided in the core material's datasheet [51]. This value's unit is W/cm^{3}T$^\beta$.

The transformer's winding fill factor (K_u) is a value that is chosen based on the application. It refers to the fraction of the area of the window area which is filled with windings. This is necessary because not all the window area can be utilized for windings. Some space is taken up by the air between the round wires, some space is taken up by the isolation, and some space could be taken up by the inability to find a winding with a size that fills up the window exactly. This is illustrated in Figure 40. It should be noted that the goal of reaching a good transformer design is to utilize the window area as much as possible. The winding fill factor can is typically expressed as a value between 0 and 1 where 0 means that there is no copper in the window and 1 means that the window is entirely full of copper. In this application, the goal value for a fill factor was 0.3.

The core's cross-sectional area is the area through which the magnetic flux flows. It can be calculated using the dimensions given in the datasheet [52]. However, due to the mechanical imperfections, it is practical to use the core's effective cross-sectional area (A_e) provided in the datasheet separately, which is more accurate [52]. The second approach is used in this work. The unit for this is cm^2.

MLT is the median length of the windings. In an E-shaped core, it can be calculated using the dimensions provided in the datasheet [52]. The MLT in an E core is illustrated in Figure 41 with the core shown above. The blue line illustrates the path of the MLT. In this work, the units used for MLT are cm.

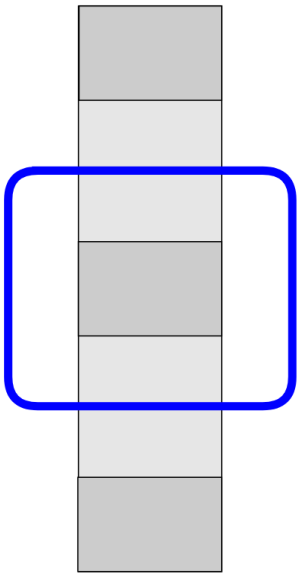

Figure 41. Illustration of MLT in an E core transformer.

Considering the need for a large core for the following transformer designs, the only viable solution is to use a shoebox design which encompasses the stacking of cores together to achieve a larger overall core size which is required as specified in the calculations below.

The second step is to evaluate the peak magnetic flux density in the transformer. The peak AC magnetic flux density can be calculated using Equation A2.9 [49].

$$\Delta B = \left[10^8 \cdot \frac{\rho \lambda_1^2 I_{\text{tot}}^2}{2K_u} \cdot \frac{(MLT)}{W_A A_c^3 l_e} \cdot \frac{1}{\beta K_{\text{fe}}}\right]^{\left(\frac{1}{\beta+2}\right)} \tag{A2.9}$$

Here, ΔB represents the peak magnetic flux density, ρ represents copper's resistivity, λ_1 represents the volt-seconds applied on the primary side of the transformer, I_{tot} represents the sum of primary side and secondary side RMS currents, K_u represents the winding fill factor, MLT stands for the Median Length per Turn for the core, W_A represents the window area of the core, A_c represents the cross-sectional area of the core, l_e represents the effective magnetic path length in the core, β represents the core loss exponent and K_{fe} represents the core loss coefficient. Multiplication by 10^8 is used to compensate for the cm units used throughout the design process for dimensions.

The effective length of the magnetic flux in the core (l_e) can be calculated using the dimensions given in the core's datasheet. However, due to the imperfections in the mechanical properties, a more accurate value for l_e is typically given in the core's datasheet [52]. The second approach is used in this work. This value is represented in cm units.

Evaluation of the peak magnetic flux is needed in order to estimate whether the application and the chosen core material are compatible. The magnetic flux density cannot exceed the saturation limit of the core. Moreover, there should be a healthy buffer between the peak magnetic flux density and the saturation limit. Additionally, in a transformer, where the magnetic flux changes from a positive peak to a negative peak at the switching frequency of the converter, the peak value also influences the losses in the transformer.

Keeping these things in mind, the third step is to evaluate the number of turns and sizes of windings in the transformer. The initial number of primary side turns can be estimated using Equation A2.10 [49].

$$n_1 = \frac{\lambda_1}{2\Delta B A_c} \cdot 10^4 \tag{A2.10}$$

Here, λ_1 represents the volt-seconds applied on the primary side of the transformer, ΔB represents the peak magnetic flux density and A_c represents the core's cross-sectional area. The equation is multiplied with 10^4 to account for the units used for the dimensions, which are in cm. Having the initial number of primary turns, the number of secondary side turns can be calculated using the turns ratio which is one of the design inputs. It can be calculated using Equation A2.11.

$$n_2 = \frac{n_1}{n} \tag{A2.11}$$

Here, n represents the transformer's turns ratio. It should be noted that the output of this equation is not necessarily an integer number which wouldn't be realizable in a practical way. This means that trade-offs must be made to achieve an optimal turns count for both windings. In order to choose the wire sizes for the windings, it is necessary to calculate the fraction of the window area designated for each winding. It can be done using Equations A2.12 and A2.13 [49].

$$\alpha_1 = \frac{I_1}{I_{\text{tot}}} \tag{A2.12}$$

$$\alpha_2 = \frac{I_2}{I_{\text{tot}}} \tag{A2.13}$$

Here, α_1 and α_2 represent the fractions of the window area for primary and secondary windings respectively. As can be seen from these equations, the designated part of the window area for each winding depends on the current values in the windings. It should be noted that the secondary current I_2 is referenced to the primary side. This means that the measured RMS current value of the secondary side is divided by n.

The cross-sectional area of the wires to be used in the windings can be calculated with the help of α_1 and α_2 to divide the window area between the windings. By knowing the designated width and length of the window for each winding, it is possible to divide the window by the required number of turns. Depending on the resulting number, it becomes evident how much of the space a round wire can occupy. In case the initial calculation results in much unused space, with round wires, the solution could be either to wind using parallel wires, wind windings on top of each other, or change the size of the wire. Choosing an optimal winding configuration can be an iterative process and is prone to the availability of certain (litz) wires and core geometries. In this work, parallel windings are used. Once the winding fills the window adequately, the size of the conductor is reduced to account for isolation and tolerances. Litz wires were used in these designs.

The three steps are iteratively conducted by choosing the core materials, core sizes, winding configurations, and thermal and magnetic parameters to reach a viable design. In transformer core material selection, MnZn ferrites were selected in order to achieve higher efficiencies compared to powder cores for instance. Therefore the core material selection was conducted from available MnZn ferrites. Additionally, the volume of the transformer must stay within the system's mechanical constraints described in Chapter 4 - Benchmarking of the Converters. The constraints help to reduce free variables and the number of iterations of the magnetics design. After iterating with transformer designs, the specification of the core material, its configuration, windings, and their configurations were resolved. These parameters for PPC and DAB transformers are brought out in the Table 6. Gapless cores were used for both transformers.

Table 6. PPC and DAB converter transformer specification and input design parameters.

Input Design Parameters	**PPC**	**DAB**
V_1 (V)	800	800
V_2 (V)	200	100
f (kHz)	10	10
D	0.5	0.5
λ (V-sec)	0.02	0.02
n	4	0.8
$I_{1_{\text{RMS}}}$ (A)	12.7	55
$I_{2_{\text{RMS}}}$ (A)	51	45
I_{tot} (A)	25.45	111.25
K_u	0.3	0.3
Core Specification	**PPC**	**DAB**
Core manufacturer	Ferroxcube	Ferroxcube
Core material	3C90	3C90
Core shape	E	E
Core size (mm)	100/60/28	100/60/28
B_{sat} (mT) [51]	470	470
β [51]	1.7	1.7
Transformer's Specification	**PPC**	**DAB**
n_1 windings	12	4
n_2 windings	3	5
n_1 parallel windings	1	2
n_2 parallel windings	3	2
D strand in litz n_1 (cm)	0.0254	0.0254
D strand in litz n_2 (cm)	0.0254	0.0254
No of strands in n_1	400	950
No of strands in n_2	780	610
A conductor n_1 (cm^2)	0.203	0.963
A conductor n_2 (cm^2)	1.186	0.618
K_u actual	0.28	0.32
No. of stacked cores	4	15
MLT (cm)	44.13	132.13
$P_{\text{loss\_max}}$ (W)	56.46	211.73
V (L)	1.56	5.88
ΔB (mT)	324.36	331.58

As can be seen from this table, the requirements for the transformers are fulfilled and the resulting designs are suitable for the converters.

Similarly to the transformer, the inductor design started with a first-pass design. The first step is to evaluate the required geometry of the core. The geometrical coefficient of the inductor can be estimated using Equation A2.14 [53].

$$K_{\mathrm{g}} \geq \frac{\rho L^2 I_{\mathrm{max}}^2}{B_{\mathrm{max}}^2 R K_u} \cdot 10^8 \tag{A2.14}$$

Here, ρ represents copper's resistivity, L represents the target inductance, I_{max} represents the maximum current in the inductor, B_{max} represents core's maximum flux density, R represents the resistance of the winding and K_u represents the winding fill factor. The equation is multiplied with 10^8 to compensate for the cm units used for dimensions throughout the design process. K_g for a given core can be calculated using Equation A2.15 [53].

$$K_{\mathrm{g}} = \frac{A_{\mathrm{c}}^2 W_A}{(MLT)} \tag{A2.15}$$

Here, A_c represents the cross-section of the core, W_A represents the core's window area and the MLT represents the average length of the windings. These parameters are further detailed in the transformer design part of this appendix.

Therefore, when taking into account the required inductance, the maximum current, the maximum allowed magnetic flux density, inductor resistance, and the winding fill factor, it becomes evident that the inductor design in the first step is iterative in its nature. The maximum magnetic flux density should be chosen to be lower than the saturation limit of the core in the worst-case operation. Powder cores were considered for the design of the inductor in order to achieve higher energy density. They provide higher magnetic flux density values and low magnetic permeability values. Furthermore, the availability of large cores, the possibility of stacking cores together, and the available core materials set limitations on the available solutions. Additionally, every parameter change affects the overall selection of cores.

The second step in the design of an inductor is to solve the magnetic circuit. It can be described with Equation A2.16 [53].

$$ni = \Phi(R) \tag{A2.16}$$

Here, Φ represents the magnetic flux in Wb, R represents the combined reluctance of the core and the air gap, n represents the number of turns in the inductor and i is the current.

The required number of turns in the inductor can be deducted from Equation A2.17 [53].

$$L = \frac{n^2}{R_c + R_g} \tag{A2.17}$$

Here L represents the inductance of the inductor, n is the number of turns in the inductor, R_c represents the reluctance of the core, and R_g represents the reluctance of the air gap. The components of the combined reluctance can be calculated using Equations A2.18 and A2.19 [53].

$$R_c = \frac{l_c}{\mu_c A_c} \tag{A2.18}$$

$$R_g = \frac{l_g}{\mu_0 A_c} \tag{A2.19}$$

In these equations l_g represents the length of the air gap, l_c represents the magnetic path length in the core, A_c represents the cross-sectional area of the core and μ_c represents the permeability of the core and μ_0 represents the permeability of vacuum. When a stacked core design is required, then A_c must reflect the overall cross-sectional area. In this work, the utilization of air gaps was not required and a gapless design was achieved.

The resulting magnetic flux density can be calculated using Equation A2.20 [53].

$$B = \mu \frac{nI}{l} \tag{A2.20}$$

Here B represents the magnetic flux density, μ represents the combined permeability of the core and the air gap, n represents the number of turns, I represents the current in the wining and l represents the combined magnetic path length. Using this equation, it is possible to verify, if the resulting magnetic flux density is below the saturation limit which can be found in the manufacturer's datasheet [50]. As mentioned above, a margin should be left between the core's saturation limit and the worst-case magnetic flux density during the operation of the converter.

After iterating through inductor design equations, the specification of the core material, its configuration and windings were resolved. These parameters for the half-bridge converter's inductor are brought out in the Table 7.

Table 7. Half-bridge converter inductor specification and input design parameters.

Input Design Parameters	**Half-Bridge**
L (mH)	2
R (Ω)	0.05
B magnetic flux density limit (mT)	1400
I_{max} (A)	56
K_u	0.4
Core Specification	**Half-Bridge**
Core manufacturer	MagInc
Core material	Xflux (μ_a 60)
Core shape	E
Core size (mm)	100/38/39
B_{sat} (mT) [50]	1600
Inductor's Specification	**Half-Bridge**
no turns	56
no parallel windings	1
A conductor n (cm^2)	0.33
K_u actual	0.55
No. of stacked cores	3
MLT (cm)	51.59
$P_{\text{loss\_max}}$ (W)	66.05
V (L)	1.74
B Actual magnetic flux density(mT)	866.12
R Actual winding resistance (Ω)	0.015

As can be seen from this table, the requirements for the inductor are fulfilled and the resulting design is suitable for the converter.

Appendix 3 - Converter Losses Calculations

The losses in the converters are calculated during a steady-state operation of the converter. Furthermore, the losses are computed for power transfer in the direction from the primary to the secondary side. The figures presented in this Appendix are sourced from the PPC simulations. The steady-state operations are illustrated in Figure 42.

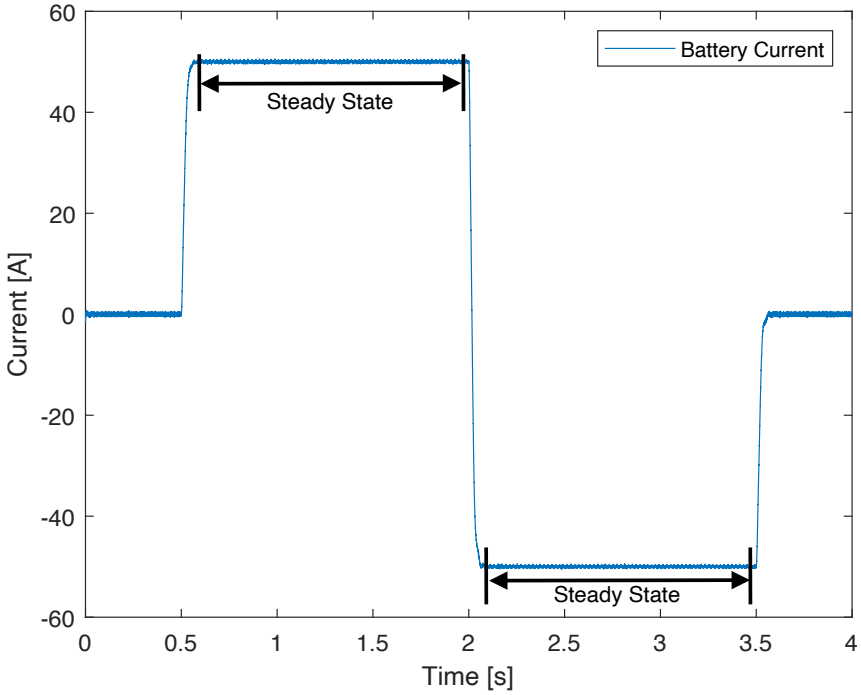

Figure 42. Battery current waveform in PPC with steady states highlighted.

The currents in the transformer windings can also be used to calculate the losses in the windings and the switches. The currents in the transformer windings are shown in Figure 43 together with highlighted steady-state operation.

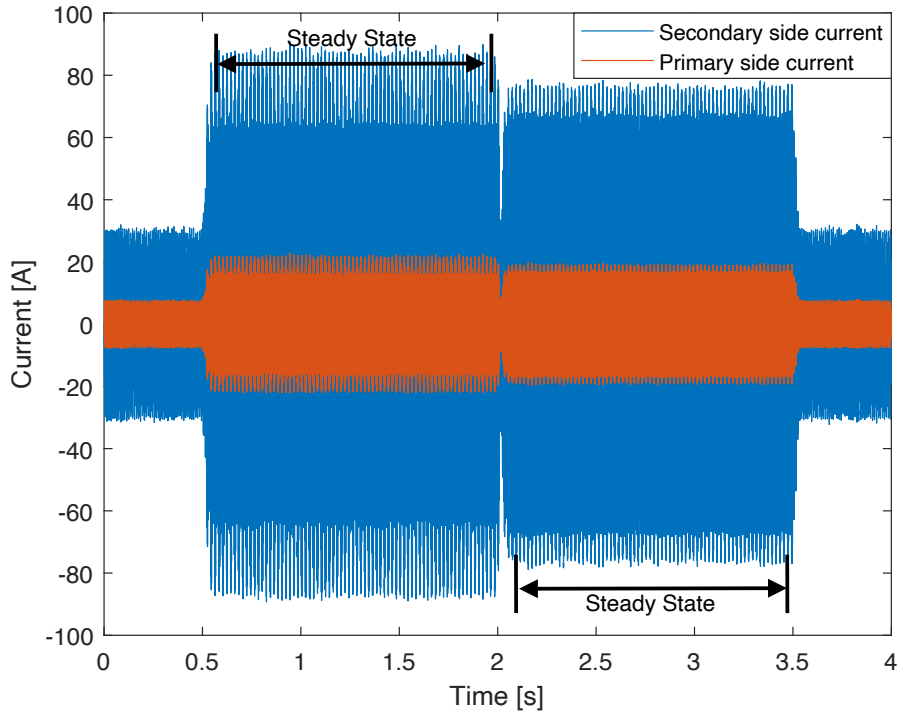

Figure 43. Transformer current waveforms in PPC with steady-state highlighted.

As can be seen from Figure 43, the current peaks in primary and secondary currents occur during the operation of the converter. They are caused by the converter's effort to compensate for the AC ripple voltage on the output. As the number of data points acquired from this simulation is significant, it is beneficial to reduce the data set for loss calculation. Due to the fact that the peaks are close to identical in their nature, one current peak section can be chosen for loss calculations. The peak section selection is illustrated in Figures 44, 45 and 46.

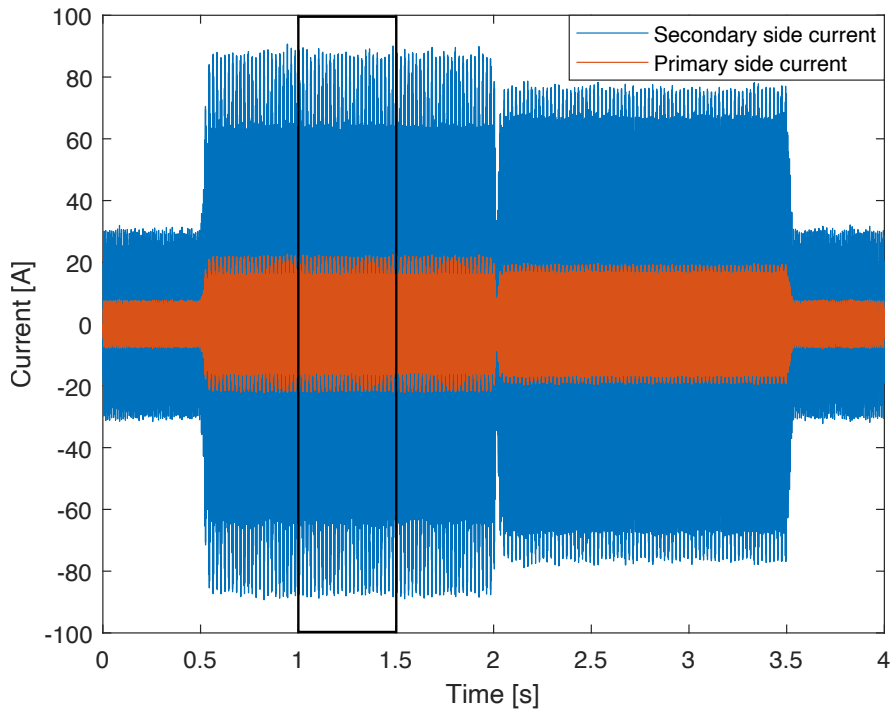

Figure 44. Current peak section selection for loss calculation - overview.

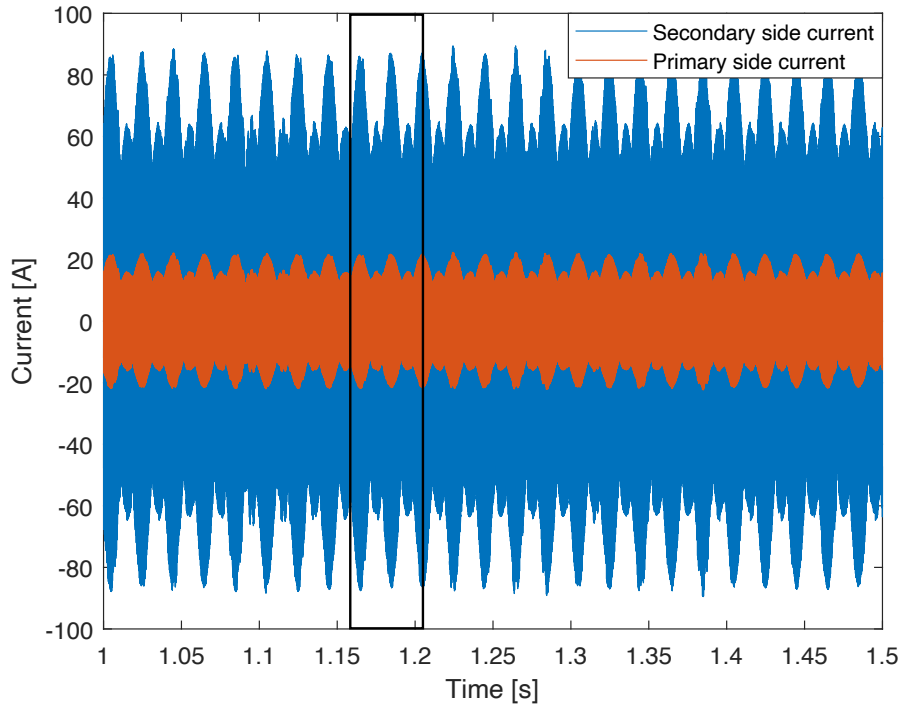

Figure 45. Current peak section selection for loss calculation - zoomed view.

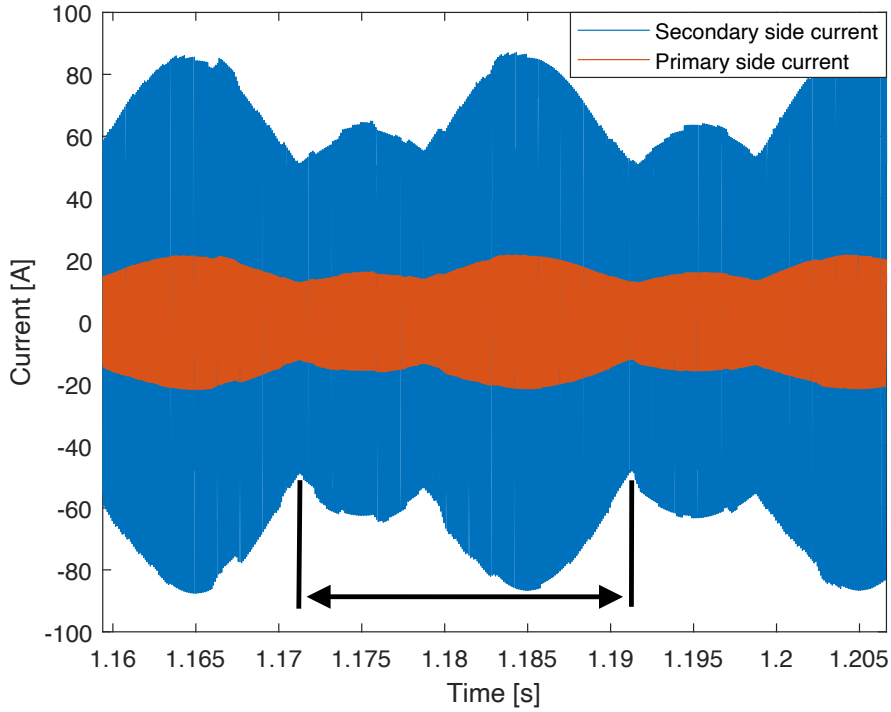

Figure 46. Current peak section selection for loss calculation - selected data.

The loss calculation for all three converters can be broadly divided into losses in the switches and losses in the transformer or inductor.

The losses in the switches will be described first. In IGBTs, the losses can be further divided into switching losses and conduction losses. Conduction losses in the switches can be calculated by using the absolute values from the current data shown in Figure 46. IGBTs can have conduction losses in the diode and in the switch. Depending on the application, the diode might not be conducting at all. In DAB-based converters, only the secondary side bridge diodes are conducting. In the half-bridge topology, both diodes conduct. This must be taken into account when calculating losses. The conduction losses are given in the datasheets as curves with voltage drop on one axis and the current on the other axis. Datasheets provide loss curves at different temperatures [54]. Here, the losses are calculated using the 125 °C loss curve. An example of the loss curves is brought out in Figure 47.

To calculate the IGBT conduction losses, every data point for the current in the switch was collected together with its corresponding timestamp. Then, the voltage drop information was collected from the datasheet and later interpolated over the entire measured current range. Then the currents and voltages were multiplied with each other to have the timestamps together with the instantaneous power loss values. To arrive at the average power loss value, data points with instantaneous power loss were integrated over the entire time

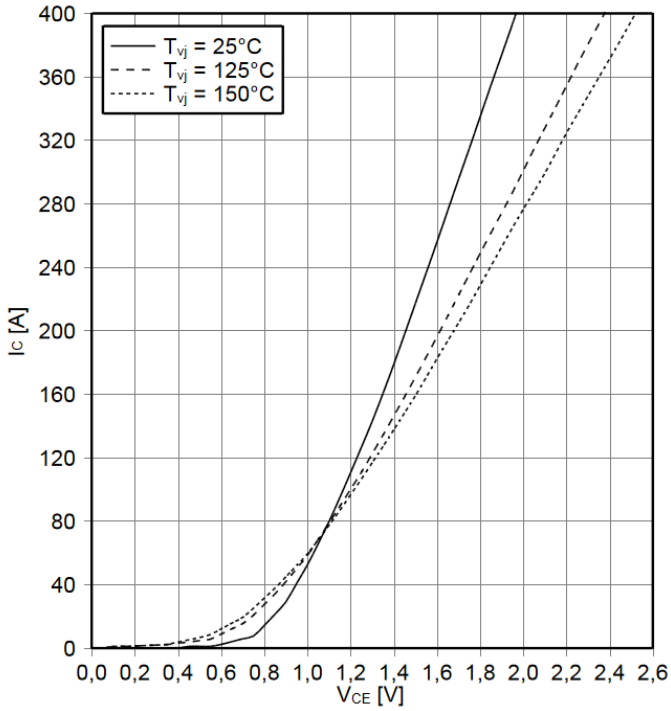

Figure 47. IGBT forward voltage drop as it is brought out in the datasheet. [54]

period and later divided with the time period to arrive at an average instantaneous power loss value. This method can be also described using Equation A3.1.

$$P_{\text{IGBT Cond Loss}} = \frac{1}{\Delta t} \int_{t_1}^{t_2} (I_c(t) \cdot V_{\text{ce}}(t))\, dt \tag{A3.1}$$

Here, $P_{\text{IGBT Cond Loss}}$ represents the average instantaneous power loss, I_C represents the current at a single data point and V_{CE} represents the voltage drop at a single data point. The multiplication of these values is the power loss at a single data point and the total energy loss is calculated using integration. Then, the average instantaneous power loss can be calculated by dividing the energy by the averaging period. This method was followed with IGBT switching losses for all converters.

Switching losses in IGBTs can be divided into losses in the switch and losses in the diode. The losses in the switch occur when the switch changes the conduction state. In other words, when the switch turns on or off. The switching loss in the diode is also referred to as a diode's reverse recovery loss, and it occurs when the diode stops conducting. The switching losses are influenced by the current at which the switching takes place and the voltage at which the switching takes place. In this example, the switching voltage is applied to the bridge in question. The current at the switching moment can be acquired

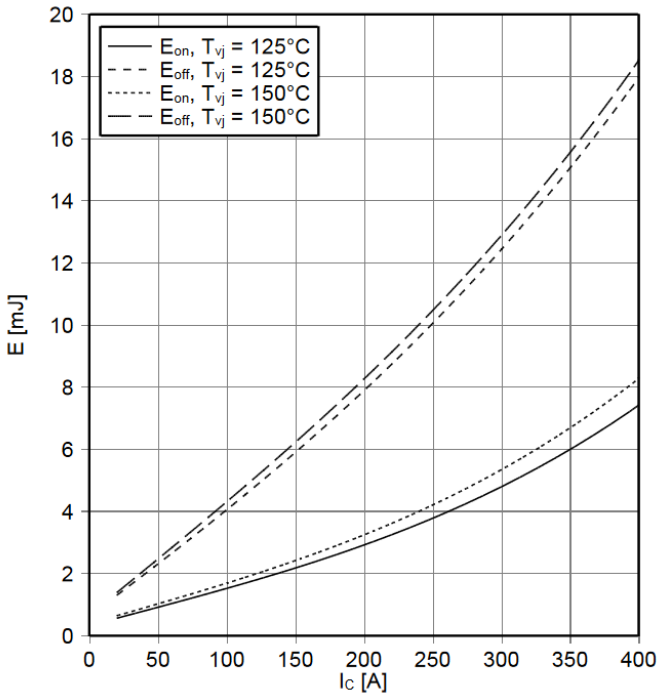

Figure 48. IGBT switching losses as they are brought out in the datasheet. [54]

from the current shape of the transformer windings or the inductor. As seen in Figure 46, the waveform consists of current peaks. The switching occurs at the peaks. This data can be transformed to show absolute values, and the current peaks can then be collected and analyzed. This method is simpler in the case of a half-bridge converter where the current does not reach negative values.

For losses in the switches, loss data from IGBT's datasheet must be collected and interpolated to match the current peak values from the simulation. Typically, the IGBT manufacturers show loss curves only at a single switching voltage. To accommodate for different voltage levels, the linear derating method can be used. It should be noted that attention should be given to the fact that when the diode is not conducting, there are also no diode reverse recovery losses. This must be taken into account when calculating losses. The switching losses are given in the datasheets as curves with energy loss on one axis and the switched current on the other. Datasheets provide loss curves at different temperatures [54]. Here, the losses are calculated using the 125 °C loss curve. Figure 48 presents an example of the switching loss curves.

To calculate the IGBT switching losses, every data point for peak current in the switch was collected with its corresponding timestamp. Then, the switching loss data was interpolated over these current values to have the energy loss data together with the timestamps. In order to calculate the instantaneous power switching loss, all of the energy loss data points

were added together. However, they need to be converted from mJ to J. Then, the power loss in J must be divided by the time period in which this power loss occurred to arrive at an instantaneous power loss value in W. The time period must be in seconds. This can be described with Equation A3.2.

$$P_{\text{IGBT SW Loss}} = \frac{\sum_{i=m}^{n} E_i}{t_n - t_m} \tag{A3.2}$$

Here, P represents the instantaneous power loss that occurs in the IGBT. E_i represents the energy loss in one instance. The first instance is indicated with a designator m, and the last is indicated with a designator n. The instances are added together and divided by the time period in which the losses occurred. This method was followed with IGBT switching losses for all converters.

The losses in the magnetics can be divided into core losses and copper losses. The core losses occur in the magnetic material depending on the magnetic flux density. This loss is nonlinearly increased with the increase of magnetic flux density. The core manufacturer has provided software for calculating the core losses for the transformer cores used in this work. The process of acquiring core loss data is illustrated in Figures 49 and 50.

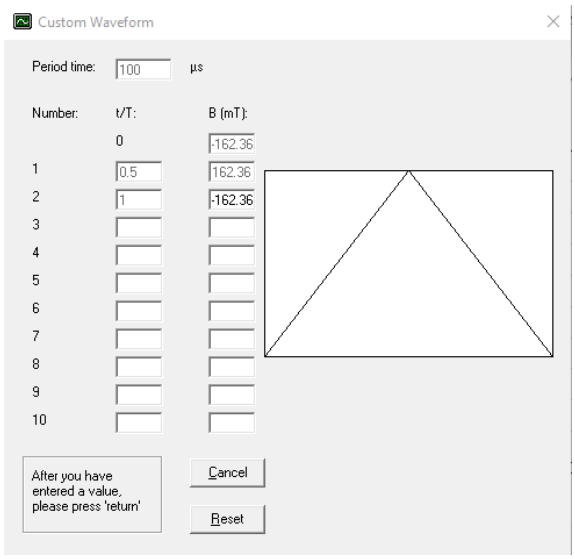

Figure 49. Custom waveform setup in Ferroxcube software.

As can be seen from Figure 49, after the change of magnetic flux density is inputted into the software, the loss curve is calculated. This loss curve shows the losses in power units per unit volume along with the change of core temperature. Therefore, as the transformers use stacked core configurations, the total volume of the transformer core must be taken

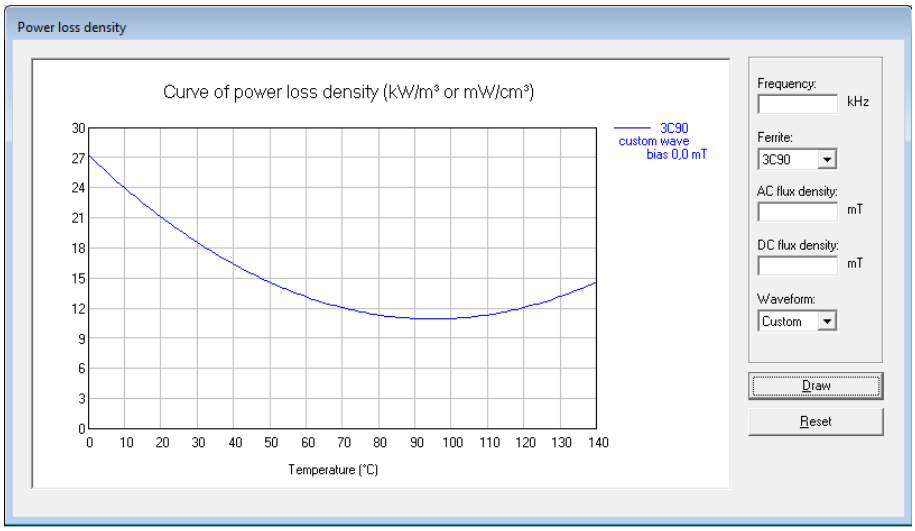

Figure 50. Core loss data output in Ferroxcube software.

into account to reach the final loss value. The core temperature of 90°C is assumed for all core loss calculations.

The copper losses occur in the windings of the transformer and inductor. For the inductor, RMS current values from the simulation results are used along with the winding resistance values calculated in Appendix 2. Ohm's law is used to calculate the losses in the windings. The losses in a DC inductor can be calculated with a high degree of accuracy. This is because the skin effect and proximity effect do not contribute to the increase in winding resistance. In transformers, however, the skin and proximity effects significantly affect the winding effective resistance. To improve efficiency, litz wires are used for the windings in transformers. This helps to reduce the impact of the skin and proximity effects. The skin effect is affected by the switching frequency, and the proximity effect is affected by the mechanical configuration of the windings. For this reason, it is difficult to accurately evaluate the resistance of the winding throughout its operation without building the transformer physically. Considering this aspect and the fact that litz wires are selected to operate at the selected swithing frequency optimally, DC resistance is considered for the loss calculation in the windings. The losses for all converters follow this methodology to achieve fair and comparable results.

Appendix 4 - Simulation Models

The Simulink simulation model of the DAB converter is shown in Figure 51. The time step used for this simulation is 100 ns. The power circuit with the ports for control signals and measurements is situated at the top. IGBTs in a full bridge configuration are colored red. The transformer is colored green. The component values in this model correspond to the physical design parameters brought out in Table 4 in Chapter 4 - Benchmarking of the Converters. The middle section depicts the generation of carrier signal, feedback realization and active DC bias correction circuits. The bottom section depicts the main control circuitry. It comprises of a reference signal generation, battery current filtering, and a PI and resonant controllers connected in a feed-forward configuration. Lastly, a saturation limiter is used to ensure that the feedback signal does not go out of bounds. Additionally, scopes are visible for battery current and switching signal visualization, which are commented out and depicted in gray. Net labels are also visible and the main scopes and connection points for data export are not shown in this figure. This simulation model can be accessed through the TalTech data repository: https://doi.org/10.48726/ws4hc-q3b07.

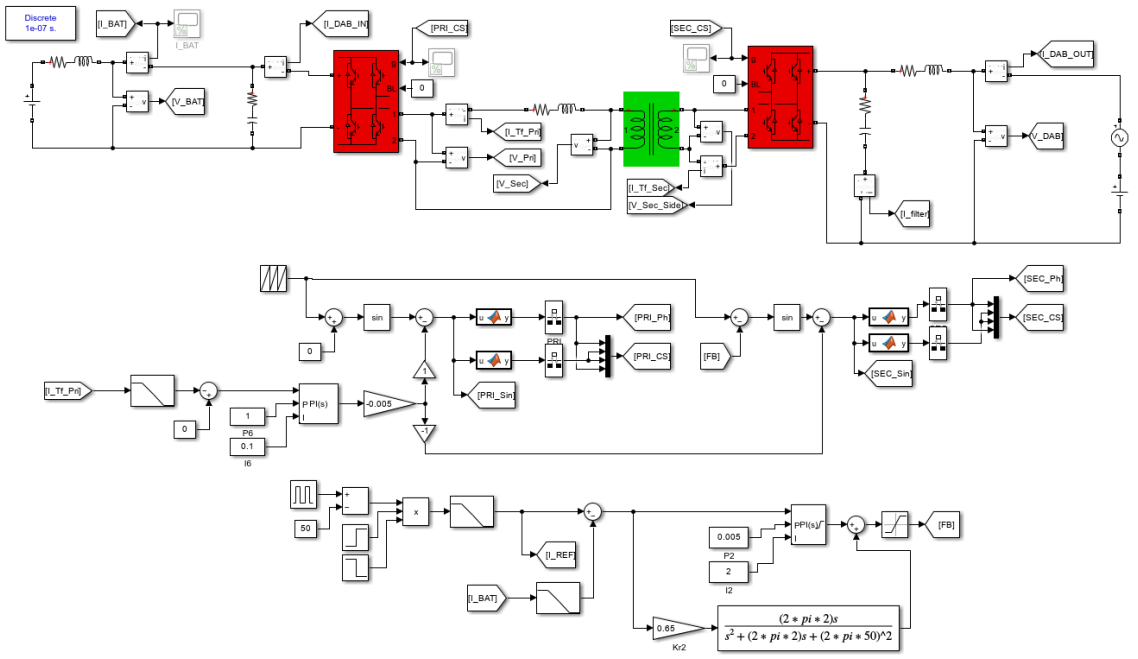

Figure 51. DAB converter simulation model.

The Simulink simulation model of the half-bridge converter is shown in Figure 52. The time step used for this simulation is 100 ns. The power circuit with the ports for control signals and measurements is situated at the top. IGBT switches are in a half-bridge configuration and are shown as separate units. The component values in this model correspond to the actual design parameters brought out in Table 4 in Chapter 4. The bottom section depicts the main control circuitry. It comprises of a reference signal generation, battery current filtering, and a PI and resonant controllers connected in a feed-forward configuration. Lastly, the generation of the carrier signal and the feedback realization using comparators are shown. Additionally, scopes are visible for switching signal visualization, which are commented out and depicted in gray. Net labels are also visible and the main scopes and connection points for data export are not shown in this figure. This simulation model can be accessed through the TalTech data repository: https://doi.org/10.48726/ws4hc-q3b07.

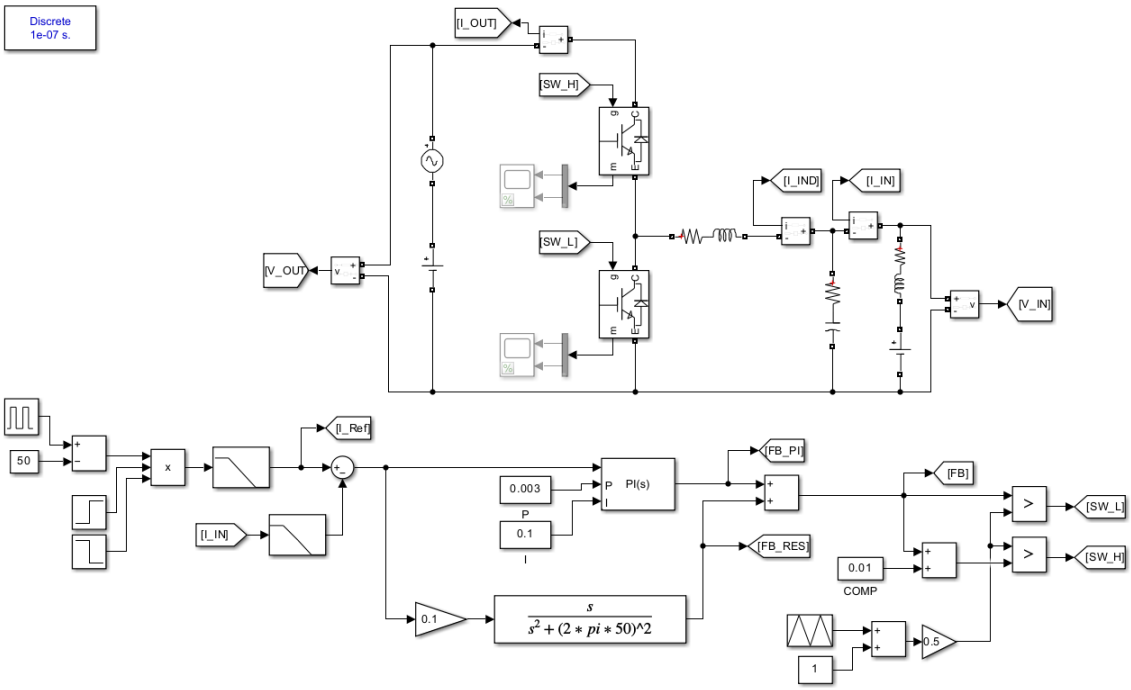

Figure 52. Half-bridge converter simulation model.

The Simulink simulation model of the PPC converter is shown in Figure 53. The time step used for this simulation is 100 ns. The power circuit with the ports for control signals and measurements is situated at the top. IGBTs in a full bridge configuration are colored red. The transformer is colored green. The component values in this model correspond to the actual design parameters brought out in Table 4 in Chapter 4. The middle section depicts the generation of carrier signal, feedback realization and active DC bias correction circuits. The bottom section depicts the main control circuitry. It comprises of a reference signal generation, battery current filtering, and a PI and resonant controllers connected in a feed-forward configuration. Lastly, a saturation limiter is used to ensure that the feedback signal does not go out of bounds. Additionally, scopes are visible for battery current and switching signal visualization that are commented out and appear gray. Net labels are also visible and the main scopes and connection points for data export are not shown in this figure. This simulation model can be accessed through the TalTech data repository: https://doi.org/10.48726/ws4hc-q3b07.

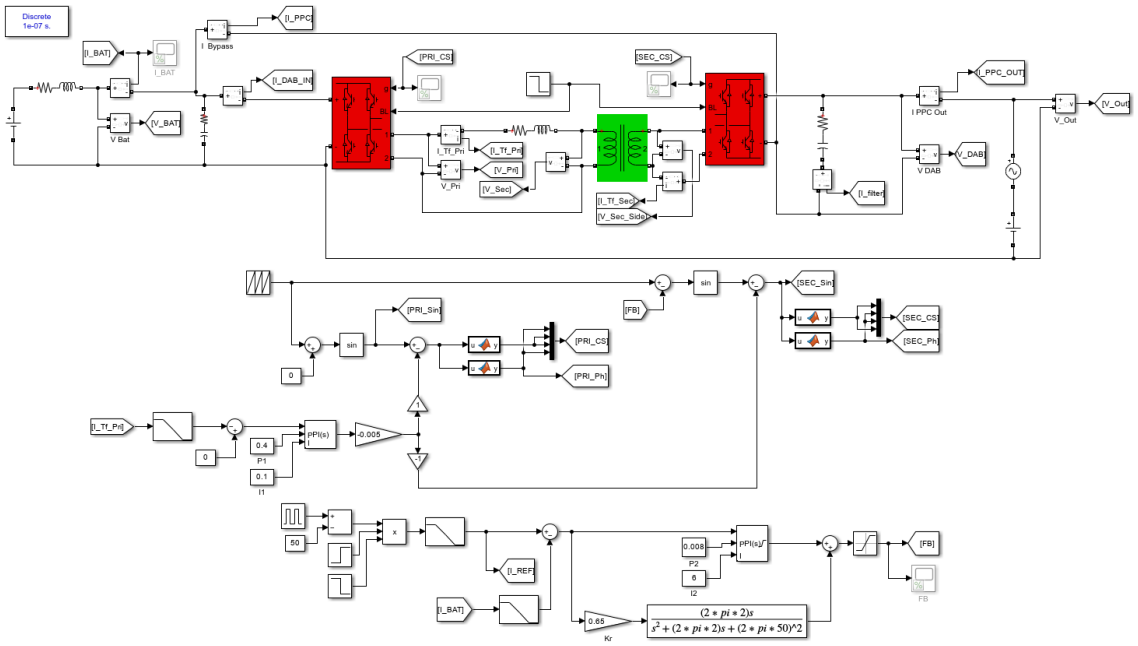

Figure 53. PPC simulation model.